

ABSTRACT

PARK, JI-SOO. Growth and Characterization of GaN and AlGaN Thin Films and Heterostructures and the Associated Development and Evaluation of Ultraviolet Light Emitting Diodes. (Under the direction of Professor Robert F. Davis)

AlGaN-based thin film heterostructures have been grown and fabricated into ultraviolet light emitting diodes with and without p-type and/or n-type AlGaN carrier-blocking layers at the top and the bottom of the quantum wells, respectively, and having the principal emission at 353 nm. The highest values of this peak intensity and light output power were measured in the devices containing p-type carrier-blocking layers. Growth of an n-type carrier-blocking layer had an adverse effect on these device characteristics. A broad peak centered at ~540nm exhibited yellow luminescence and was present in the spectra acquired from all the devices. This peak is attributed to absorption of the ultraviolet emission by and re-emission from the p-GaN and/or to the luminescence from the AlGaN within quantum wells by current injection.

Individual $\text{Al}_x\text{Ga}_{1-x}\text{N}$ films ($x < 0 \leq 1$) have been grown on Si- and C-terminated 6H-SiC{0001} substrates and characterized for electron emission applications. The large range in the values of x was achieved by changing the fraction of Al in the gas phase from 0 to 0.45. The ionized donor concentration in the n-type, Si-doped $\text{Al}_x\text{Ga}_{1-x}\text{N}$ films decreased as the mole fraction of Al was increased due to the reduction in the donor energy level and compensation. The use of the SiH_4 flow rate, which yields a Si concentration of $\sim 1 \times 10^{19} \text{ cm}^{-3}$ in GaN, established the upper limit of the mole fraction of Al wherein n-type doping could be achieved at ~0.61. The electron affinity of the Si-doped $\text{Al}_{0.61}\text{Ga}_{0.39}\text{N}$ films was as low as 0.1 eV. Increasing the Si doping concentration

in AlN films to as high as $1 \times 10^{21} \text{ cm}^{-3}$ caused slight degradation in crystal perfection. No difference was found in the Al core level binding energies between undoped and Si-doped AlN films. The results of XPS and UPS experiments showed that the work function of N-polar AlN films was 0.6 eV lower than that of Al-polar films.

**GROWTH AND CHARACTERIZATION OF GaN AND AlGa_N THIN
FILMS AND HETEROSTRUCTURES AND THE ASSOCIATED
DEVELOPMENT AND EVALUATION OF ULTRAVIOLET LIGHT
EMITTING DIODES**

by
JI-SOO PARK

A dissertation submitted to the Graduate Faculty of
North Carolina State University
in partial fulfillment of the
requirements for the Degree of
Doctor of Philosophy

DEPARTMENT OF MATERIALS SCIENCE AND ENGINEERING

Raleigh

2005

APPROVED BY:

Dr. Robert F. Davis
Chair of Advisory Committee

Dr. Robert Nemanich

Dr. Mark Johnson

Dr. John Muth

BIOGRAPHY

Ji-Soo Park received BS and MS degrees in Materials Science and Engineering from Seoul National University, Seoul, South Korea, in 1994 and 1996, respectively. He conducted research on Si oxidation using N_2O for thin gate dielectrics and its electrical characterization for his MS thesis. In 1996, he joined R&D Division of Hynix Semiconductor Inc. (formerly, LG Semicon. Co). During his research career as a process engineering in Hynix, he worked on advanced process development for Logic and DRAM technology, especially low resistivity gate electrode, self-aligned silicide process and thin gate dielectrics. He began his doctoral work in Materials Science and Engineering at North Carolina State University in July of 2001 under the direction of Dr. Robert F. Davis.

ACKNOWLEDGEMENTS

Preserve me, O God, for in You I put my trust. O my soul, you have said to the LORD, "You are my Lord, My goodness is nothing apart from You." As for the saints who are on the earth, "They are the excellent ones, in whom is all my delight." Their sorrows shall be multiplied who hasten after another god; Their drink offerings of blood I will not offer, Nor take up their names on my lips. O LORD, You are the portion of my inheritance and my cup; You maintain my lot. The lines have fallen to me in pleasant places; Yes, I have a good inheritance. I will bless the LORD who has given me counsel; My heart also instructs me in the night seasons. I have set the LORD always before me; Because He is at my right hand I shall not be moved. Therefore my heart is glad, and my glory rejoices; My flesh also will rest in hope. For You will not leave my soul in Sheol, Nor will You allow Your Holy One to see corruption. You will show me the path of life; In Your presence is fullness of joy; At Your right hand are pleasures forevermore. (Psalm 16)

I'd like to give all my gratitude to my God, who has provided me everything to make this dissertation possible.

TABLE OF CONTENTS

<i>List of Figures</i>	vi
------------------------------	----

<i>List of Tables</i>	x
-----------------------------	---

1. $\text{Al}_x\text{Ga}_{1-x}\text{N}$ Thin Films and Ultraviolet Light Emitting Diodes: Introduction and Literature Review 1

Abstract	2
1.1 Introduction	4
1.2 $\text{Al}_x\text{Ga}_{1-x}\text{N}$ Alloys	4
1.2.1 MOVPE Growth of $\text{Al}_x\text{Ga}_{1-x}\text{N}$ Alloys	5
1.2.2 Doping of $\text{Al}_x\text{Ga}_{1-x}\text{N}$ Alloys	7
1.3 Light Emitting Diodes	11
1.3.1 InGaN-based Visible Light Emitting Diodes	11
1.3.2 Al(In)GaN-based Ultraviolet Light Emitting Diodes	15
1.4 Outline of Dissertation	19
1.5 Summary	20
1.6 References	22

2. Comparison of the Microstructure and Chemistry of GaN(0001) Films grown Using Trimethylgallium and Triethylgallium on AlN/SiC Substrates..... 40

Abstract	41
2.1 Introduction	42
2.2 Experimental	42
2.3 Results and Discussion	43
2.4 Conclusions	46
2.5 References	47

3. Growth, Doping and characterization of $\text{Al}_x\text{Ga}_{1-x}\text{N}$ ($0 < x \leq 1$) Alloys on Si- and C-terminated 6H-SiC{0001} Substrates for Electron Emission Applications..... 53

Abstract	54
3.1 Introduction	55
3.2 Experimental Procedures	56
3.3 Results and Discussion	58
3.3.1 $\text{Al}_x\text{Ga}_{1-x}\text{N}$ Films	58
3.3.2 AlN Films	60
3.4 Summary	63
3.5 References	63

4. Growth and Fabrication of AlGa_N-based Ultraviolet Light Emitting Diodes on 6H-SiC(0001) Substrates	75
Abstract	76
4.1 Introduction.....	77
4.2 Experimental Procedures	78
4.2.1 Growth of Al _x Ga _{1-x} N Films	78
4.2.2 Growth of LED Heterostructures.....	80
4.2.3 Contacts on P-type GaN Films and N-type SiC Substrates and Design of LED Mask	82
4.2.4 Fabrication and Electrical and Optical Characterization of UV LEDs.....	84
4.3 Results and Discussion	85
4.3.1 Optical properties of the Al _x Ga _{1-x} N Films and Quantum Wells.....	85
4.3.2 P-GaN Contacts	87
4.3.3 N-SiC Contacts	91
4.3.4 Electrical and Optical Characterization of UV LEDs	92
4.4 Summary	94
4.5 References.....	95
5. Effect of Carrier-Blocking Layers on the Emission Characteristics of AlGa_N-based Ultraviolet light Emitting Diodes	110
Abstract	111
5.1 Introduction.....	112
5.2 Experimental Procedures	113
5.3 Results and Discussion	115
5.4 Summary	120
5.5 References.....	121
6. Recommendations for Future Research	130
7. Appendices	135
7.1 Detailed Process Sequences and Conditions for the Fabrication of Ultraviolet Light Emitting Diodes on 6H-SiC(0001) Substrates	135
7.2 Calibration procedures for Light Output Power measurements of Ultraviolet Light Emitting Diodes Fabricated in This Program	138

LIST OF FIGURES

Figure 1.1 Ionization energy of the Si donor in $\text{Al}_x\text{Ga}_{1-x}\text{N}$ as a function of the Al content, x	30
Figure 1.2 Activation energy of Mg acceptors in Mg-doped, p-type $\text{Al}_x\text{Ga}_{1-x}\text{N}$ as a function of the Al content, x . The inset shows the measured temperature dependence of the hole concentration in the p-type $\text{Al}_{0.27}\text{Ga}_{0.73}\text{N}$ sample from which an activation energy of 0.310 eV was obtained	31
Figure 1.3 Calculations of the spatially averaged hole concentration (at 300 K) for a Mg-doped $\text{AlGaIn}/\text{GaIn}$ superlattice as a function of the superlattice dimension L . The calculations (a) ignore the polarization fields, (b) include them, and (c) include both polarization fields and quantization effects. The hole concentration calculated for a bulk AlGaIn film is indicated by the arrow.....	32
Figure 1.4 Schematic of a representative p-GaN/n-InGaIn/n-GaN double hterostructure developed for blue LEDs by Nakamura <i>et al.</i>	33
Figure 1.5 Schematic of the material structure used to fabricate green, single QW LEDs	34
Figure 1.6 Electroluminescence of (a) blue, (b) green, and (c) yellow single QW LEDs at a forward current of 20 mA	35
Figure 1.7 The relative output power of blue InGaIn single QW LEDs grown on ELOG GaIn with a lower dislocation density and on sapphire substrates as a function of the forward current. Note that the LEDs on sapphire substrates show almost the same output power as the LEDs on the ELOG GaIn despite the much higher dislocation density of the latter material.....	36
Figure 1.8 The relationship between the intensity of the photoluminescence peak and the threading dislocation density in $\text{GaIn}/\text{Al}_{0.08}\text{Ga}_{0.82}\text{In}$ multi-QWs grown on $\text{Al}_{0.22}\text{Ga}_{0.78}\text{In}$ films	37
Figure 1.9 Comparison of the output power at 340 nm from LEDs grown on free-standing GaIn substrates (triangles) and on sapphire (squares) in pulsed injection mode	38
Figure 1.10 Schematic drawing of the LED structure grown by Nishida <i>et al.</i> containing n- and p-type short period alloy superlattices (SPASL) below and above the multi quantum wells. The SPASLs were used as transparent conductive layers	39

Figure 2.1 Optical micrographs obtained using Nomarski interference filter and showing the effect of growth temperature on the surface microstructure of 1 μ m GaN films deposited using TEG at (a) 980°C, (b) 1020°C and (c) 1050°C. Similar surface microstructures were obtained using TMG at 1020°C, 1050°C, and 1080°C, respectively	49
Figure 2.2 Time necessary to grow 1 μ m thick GaN films at 1020°C using TEG and at 1050°C using TMG as a function of V/III ratio.....	50
Figure 2.3 SIMS depth profiles of carbon, oxygen, hydrogen and silicon in (a) TEG GaN grown at 1020°C (V/III=1323) and (b) TMG GaN grown at 1050°C (V/III=2045)	51
Figure 2.4 FWHM of GaN(0002) peak and RMS roughness in 50 μ m x 50 μ m scans of TEG GaN grown at 1020°C (V/III=1323) and TMG GaN grown at 1050°C (V/III=2045). Number of measurements is 10; the error bars show standard deviation	52
Figure 3.1 (a) Room temperature CL spectra of undoped Al _{0.41} Ga _{0.59} N film and (b) Al mole fraction in Al _x Ga _{1-x} N films as a function of Al source fraction in the growth ambient.....	67
Figure 3.2 Ionized donor concentration, N _D -N _A , as a function of Al mole fraction in Al _x Ga _{1-x} N films. The SiH ₄ flow rate was held constant at 14.3 nmol/min.....	68
Figure 3.3 (a) Room temperature CL spectra of undoped and Si-doped Al _{0.41} Ga _{0.59} N films and (b) schematic showing conduction and valence bands and their respective bandgap energies as a function of momentum of the electrons.....	69
Figure 3.4 (a) Illustration of the use of various critical energies to determine the electron affinity of a semiconductor from UPS spectra and (b) the UPS spectrum of our Si-doped Al _{0.61} Ga _{0.39} N film.....	70
Figure 3.5 SIMS depth profiles of Si in (a) the reference AlN sample implanted with Si ⁺ using an energy of 90keV and a fluence of 8 x 10 ¹⁴ cm ⁻² , (b) the AlN samples doped with 5 ppm and 1000 ppm SiH ₄ contained in H ₂ , and (c) the AlN samples doped with 1000ppm SiH ₄ and grown on Si- and C-terminated SiC substrates.....	71
Figure 3.6 (a) XPS spectra of the Al 2p core level binding energy acquired from Si-doped (1 x 10 ²¹ cm ⁻³) AlN films on Si- and C-terminated SiC{0001} substrates, (b) schematic of the energy bands of Al- and N-terminated AlN showing the relation between the Al core level binding energy and the work function	72
Figure 3.7 XPS spectra of undoped and Si-doped (1 x 10 ²¹ cm ⁻³) AlN films.....	73
Figure 3.8 UPS spectra acquired from Si-doped (1 x 10 ²¹ cm ⁻³) AlN films on (a) Si-terminated and (b) C-terminated SiC{0001} substrates	74

Figure 4.1 Cross-sectional schematic of the LED structure.....	98
Figure 4.2 Al mole fraction in the $\text{Al}_x\text{Ga}_{1-x}\text{N}$ films and wavelength of bandedge emission peak determined via CL as a function of the fraction of Al in the growth ambient	99
Figure 4.3 (a) Plan-view and (b) cross-sectional schematics of the patterns of the Au/Ti thick electrode and the Au/Ni semi-transparent electrode deposited on the top p-GaN contact.....	100
Figure 4.4 PL spectra acquired from (a) one, three and six period quantum wells with undoped barriers and (b) three period quantum wells with undoped and Si-doped ($N_D - N_A = 5 \times 10^{18} \text{ cm}^{-3}$) barriers.....	101
Figure 4.5 I-V characteristics of Ni/Au contacts on p-GaN having a Mg concentration of $2 \times 10^{19} \text{ cm}^{-3}$ (a) as-deposited and sequentially annealed at 450 °C or 500 °C for 30 sec in nitrogen or 500 °C for 10min in air, and (b) after cleaning the GaN surface in either HCl at room temperature or at 85 °C or in aqua regia at room temperature prior to metal deposition. They were annealed at 550 °C for 10 min in air. The contact spacing of TLM patterns was (a) 10 μm and (b) 30 μm	102
Figure 4.6 I-V characteristics of Ni/Au contacts on p-GaN films with Mg concentrations of $2 \times 10^{19} \text{ cm}^{-3}$ and $5 \times 10^{19} \text{ cm}^{-3}$. The surface of each film was cleaned using an HCl solution at 85 °C. The film/contact assemblies were annealed in air at 450 °C for 10 min. The contact spacing in the CTLM patterns was 15 μm	103
Figure 4.7 (a) Current-voltage (I-V) characteristics of annealed Ni/Au contacts deposited on cleaned p-GaN containing $5 \times 10^{19} \text{ cm}^{-3}$ Mg as a function of the contact spacing of the CTLM pattern and (b) total resistance (R_t) as a function of $\ln(R/r)$, where R and r denote the radii of the circular cutouts and the circular contacts inside the circular cutouts, respectively	104
Figure 4.8 Current-voltage (I-V) characteristics of semi-transparent electrode (4nm-thick Ni and 4nm-thick Au) as-deposited and sequentially annealed at different temperatures in air for 10 min	105
Figure 4.9 Current-voltage (I-V) characteristics of Ni/Au contacts deposited on (a) n-type SiC(0001) wafers and annealed under different conditions and (b) Mg-doped GaN films annealed either in nitrogen alone for Mg activation or in forming gas following the Mg activation anneal. The contact spacing of CTLM patterns was 15 μm	106
Figure 4.10 Current-voltage (I-V) characteristics of LED (a) on linear and (b) on semi-log scale	107
Figure 4.11 EL spectra of LED acquired using a (a) low injection current (40~90mA), (b) high injection current (100~300mA) and (c) very high injection current	

(400~1400mA). A different integration time was used in each case to avoid peak saturation.....	108
Figure 4.12 EL spectra of LED at very high injection current (400~1400mA).....	109
Figure 5.1 Cross-sectional schematic of the LED structure without CBL.....	124
Figure 5.2 Schematic diagrams showing the positions of the MQWs in the LEDs (a) without a CBL, (b) with a P-CBL, (c) with an N-CBL, and (d) with N- and P-CBLs and the percentages of Al in each layer	125
Figure 5.3 Current-voltage characteristic of LEDs without a CBL	126
Figure 5.4 Semilogarithmic plots of EL spectra acquired from LEDs (a) without a CBL, (b) with a P-CBL, (c) with an N-CBL, and (d) with NP-CBLs as a function of injection current. The inset in (a) shows linear plots of the EL spectra of an LED without a CBL	127
Figure 5.5 EL intensities as a function of injection current of (a) the 353nm peaks and (b) the 540nm peaks and (c) the intensity ratios of the 353nm peaks to 540nm peaks of LEDs with different CBLs	128
Figure 5.6 Light output power of the LEDs with different CBLs as a function of injection current	129

LIST OF TABLES

Table 1.1 Lattice parameters and interplanar distances of the III-Nitride compounds and the substrates of α -Al₂O₃ and 6H-SiC used for the growth of LED material structures. All hexagonal forms of SiC and the solid solutions in the AlGaN system belong to the space group P6₃mc (186). The coefficients of linear thermal expansion of the nitrides vary with temperature in a nonlinear fashion..... 29

Table 3.1 FWHM values of the (0002) peak acquired from undoped and Si-doped AlN films. The number of measurements acquired from each film was 10..... 66

1. $\text{Al}_x\text{Ga}_{1-x}\text{N}$ Thin Films and Ultraviolet Light Emitting Diodes: Introduction and Literature Review

Ji-Soo Park and Robert F. Davis

*Department of Materials Science and Engineering, North Carolina State University,
Raleigh, NC 27695-7907*

Abstract

Metalorganic vapor phase heteroepitaxial growth and doping of $\text{Al}_x\text{Ga}_{1-x}\text{N}$ alloys as well as the present status of InGaN-based visible and AlGaN-based ultraviolet (UV) light emitting diodes (LEDs) are reviewed. A strong gas-phase pre-reaction occurs between Al precursors and NH_3 ; thus, the optimization of growth parameters, especially pressure, is very important to achieve the growth of $\text{Al}_x\text{Ga}_{1-x}\text{N}$ films with high Al concentrations. Donor doping of $\text{Al}_x\text{Ga}_{1-x}\text{N}$ films with Si is difficult due to an increase in donor activation energy with an increase in the Al content and the compensation of this donor by acceptor-type defects such as oxygen, carbon and cation vacancies. Indium-silicon co-doping and heavy doping of Si have been proposed to achieve n-type doping of $\text{Al}_x\text{Ga}_{1-x}\text{N}$ films with $x > 0.5$. Acceptor doping is also difficult to achieve in these films, since the Mg activation energy in $\text{Al}_x\text{Ga}_{1-x}\text{N}$ increases with an increase in the Al content. Mg- δ -doping and Mg-doped $\text{Al}_x\text{Ga}_{1-x}\text{N}/\text{GaN}$ superlattices have been proposed to achieve effective p-type doping of these solid solutions.

High brightness yellow, green, and blue LEDs have been achieved with the use of InGaN active layers. The power and efficiency of AlGaN-based UV LEDs are much lower than those of InGaN-based visible LEDs, since the AlN-GaN system, unlike the InN-GaN system, does not undergo phase separation of nano-sized precipitates with a much lower density of recombination states than are present in the InGaN matrix (and are present in all AlGaN films) due to the high density of dislocations. As such, light emission via direct band-to-band or donor-to-valence band transitions is markedly compromised in all AlGaN films. Quaternary $\text{In}_x\text{Al}_y\text{Ga}_{1-x-y}\text{N}$ active layers in quantum wells, $\text{Al}_x\text{Ga}_{1-x}\text{N}/\text{GaN}$ (or AlN) superlattices, low dislocation density substrates and

combinations of these components have been used to counter the negative effects of the dislocations and to achieve increased power output and efficiency in AlGaIn-based high-power UV LEDs.

1.1 Introduction

Numerous process routes have been investigated that would allow very close control of the composition, bandgap energy and lattice constant(s) of ternary III-V semiconductor alloys to control some of the properties of the associated devices. The solid solutions belonging to the $\text{Al}_x\text{Ga}_{1-x}\text{X}$ ($\text{X}=\text{Sb, As, P, and N}$) systems are the closest to ideal,¹ because the difference in the covalent radii of the cations is only 0.08 Å (1.26 Å for Ga and 1.18 Å for Al).

Wurtzite structure GaN and AlN have lattice mismatches of only 2.4% and 4% along the a- and the c-axes, respectively, as shown in Table 1.1.² The direct bandgap energies (UV wavelengths) of $\text{Al}_x\text{Ga}_{1-x}\text{N}$ alloys ($0 \leq x \leq 1$) range from 3.4 eV (360 nm in GaN) to 6.2 eV (200 nm in AlN). Thus, the $\text{Al}_x\text{Ga}_{1-x}\text{N}$ alloys are attractive for optoelectronic devices such as UV light-emitting diodes (LEDs) and laser diodes (LDs). The large bandgaps and good high-field electron mobilities also make these materials candidates for high-power, and high-frequency microelectronic applications. Commercial success of most of these applications requires the epitaxial growth of films with low densities of structural defects and controlled n-type and p-type doping.

In this chapter, the growth of $\text{Al}_x\text{Ga}_{1-x}\text{N}$ alloys and the introduction of donor and acceptor elements to achieve n-type and p-type doping via metalorganic vapor phase epitaxy (MOVPE) are reviewed. The achievement and current status of InGaN-based visible and AlGaN-based ultraviolet LEDs (UV LEDs) are also reviewed. An annotated outline of this dissertation is also presented.

1.2 $\text{Al}_x\text{Ga}_{1-x}\text{N}$ Alloys

1.2.1. MOVPE Growth of $\text{Al}_x\text{Ga}_{1-x}\text{N}$ Alloys

Hagan *et al.*³ synthesized $\text{Al}_x\text{Ga}_{1-x}\text{N}$ films by chemical vapor deposition (CVD) and showed the existence of an alloy system throughout the range from GaN to AlN. Baranov *et al.*⁴ grew $\text{Al}_x\text{Ga}_{1-x}\text{N}$ films up to $x=0.45$ by chloride vapor phase epitaxy (VPE) at 1050 °C and measured the electrical and optical properties. Yosida *et al.*⁵ deposited $\text{Al}_x\text{Ga}_{1-x}\text{N}$ films that contained the entire composition range on sapphire and Si substrates using reactive molecular beam epitaxy (MBE).

The formation of gas-phase adducts between group III and V precursors has been troublesome for MOVPE growth of III-V materials,⁶⁻⁷ as it affects both the efficiency of the deposition and the uniformity of the resulting film. The formation of gas-phase adducts arises from the fact that group-III metalorganics are electron acceptors (Lewis acids), while ammonia, with a spare electron pair on the nitrogen atom, is an electron donor (or Lewis base). The elimination of gas-phase pre- (or parasitic) reactions between NH_3 and metalorganics is very important for achieving the growth of high Al content $\text{Al}_x\text{Ga}_{1-x}\text{N}$ films.

Gas-phase adduct formation in the trimethylgallium/ammonia (TMG)/ NH_3 system has been suggested by Mazzarese *et al.*⁸ Thon and Kuech⁹ observed the formation of the adduct compound $(\text{CH}_3)_3\text{Ga}:\text{NH}_2$. The latter authors also suggested⁹ that decomposition products such as $[(\text{CH}_3)_2\text{Ga}:\text{NH}_2]_x$ (most probably $x=3$) likely occurred from a methane-elimination reaction. As a result, pyrolysis of TMG was shifted to higher temperatures in a H_2/NH_3 ambient compared to the temperature of decomposition in a H_2 ambient. However, such adducts are fully decomposed at the high temperatures used for the growth of GaN thin films and do not influence significantly the decomposition of TMG

or the incorporation of Ga into these films, as judged by the insensitivity of the GaN growth rates as a function of the partial pressure of NH_3 .

Trimethylaluminium (TMA) has also been observed to react with NH_3 to form a white crystalline solid at room temperature.¹⁰ Chen *et al.*¹¹ found that GaN growth efficiency, which is defined as the ratio between the growth rate and the molar flow rate of TMG, was almost constant between 85 Torr and atmospheric pressure; it was also constant in the temperature range where the growth is diffusion controlled. On the other hand, AlN growth efficiency drastically decreased with increasing reactor pressure and with decreasing growth temperature. This indicates that a strong gas-phase pre-reaction occurs between NH_3 and TMA.

Khan *et al.*¹² were able to grow $\text{Al}_x\text{Ga}_{1-x}\text{N}$ solid solutions over the entire binary system using MOVPE at low pressure (5-100 Torr). However, at atmospheric pressure, Koide *et al.*¹³ found that white, Al-rich deposits were observed on AlGaN layers and that control over the solid composition was impossible at low gas velocities (0.7 - 2 cm/sec). They attributed these deposits to involatile adduct formation, which depleted the Al precursor in the gas phase. Han *et al.*¹⁴ suggested that gas phase adduct ($\text{TMA}:\text{NH}_3$) reactions not only reduced the incorporation efficiency of TMA, but also hindered the incorporation of TMG. Choi *et al.*¹⁵ found that increasing the NH_3 flow rate at a constant flow rate of group-III precursors under the total growth pressure of 200 Torr resulted in a decrease in both the Al composition within and the growth rate of the $\text{Al}_x\text{Ga}_{1-x}\text{N}$ films. Increasing the flow rate of the TMA while keeping constant the flow rate of the TMG resulted in the eventual cessation in the incorporation of the Al into the AlGaN films, indicating the onset of a gas phase pre-reaction between NH_3 and TMA. Kondratyev *et*

*al.*¹⁶ found that the Al composition of the $\text{Al}_x\text{Ga}_{1-x}\text{N}$ films was proportional to the TMA flow rate at low growth pressure (75 Torr); however, it saturated at high pressure (300 Torr).

1.2.2. Doping of $\text{Al}_x\text{Ga}_{1-x}\text{N}$ Alloys

It is essential to have close control of the doping and the associated conductivity of AlGaN solid solutions for the successful application of these materials for optoelectronic and high-power and high-frequency electronic devices. However, it has been reported^{13, 17-19} that it is very difficult to achieve highly conductive $\text{Al}_x\text{Ga}_{1-x}\text{N}$ solid solutions with high Al content. Several experimental studies have indicated a steady decrease in the electron concentration and the associated n-type conductivity of these alloys with increasing values of x . Koide *et al.*¹³ reported that a decline in the free electron concentration for $x > 0.2$. For unintentionally doped, n-type $\text{Al}_x\text{Ga}_{1-x}\text{N}$, Lee *et al.*¹⁷ reported a rapid decrease in conductivity for $x > 0.4$. McCluskey *et al.*¹⁸ found a significant decrease in the conductivity for $x > 0.3$ in unintentionally doped AlGaN samples. Bremser *et al.*¹⁹ also achieved intentional n-type doping with Si up to $x = 0.42$; however, for $x > 0.42$, the addition of Si resulted in highly resistive films.

The decrease in the free electron concentration in $\text{Al}_x\text{Ga}_{1-x}\text{N}$ solid solutions with an increase in Al concentration is mainly due to the concomitant increase in the donor activation energy. Polyakov *et al.*²⁰ showed that the Si donor ionization energy increased from 18 meV for $0 < x < 0.1$ to about 50 meV for $x = 0.4$ and does not exceed 90 meV for $x = 0.6$. They also reported that an increase in Al composition was also accompanied by an increase in the density of defects with an energy level deeper than Si. Taniyasu *et al.*²¹

also found that the ionization energy of the Si donor increased slightly from 8.1meV ($x=0$) to 12 meV ($x=0.49$) but for $x>0.49$, it increased from 12meV ($x=0.49$) to 86meV ($x=1$) as shown in Fig. 1.1. Zeisel *et al.*²² reported that the activation energy of dark conductivity of Si-doped $\text{Al}_x\text{Ga}_{1-x}\text{N}$ alloys increased linearly from 18meV ($x=0$) to 320meV ($x=1$), but that of nominally undoped alloys was much higher. On the contrary, Boguslawski *et al.*²³ proposed that Si acts as a shallow donor for $x<0.6$ but forms DX centers at $x \approx 0.6$, which quench doping efficiency.

In addition, compensation of Si donors by acceptor-like defects was reported to be one of the origins causing difficulty in n-type doping of $\text{Al}_x\text{Ga}_{1-x}\text{N}$. Van de Walle *et al.*²⁴ argued that the reduced conductivity results from compensation by native defects with acceptor character. They reported that oxygen behaves as a deep acceptor for $x>0.27$ due to a DX transition, which converts a shallow donor into a deep level.¹⁸ Carbon can also be introduced into the growing $\text{Al}_x\text{Ga}_{1-x}\text{N}$ films via decomposition of the metalorganic sources. It has been reported²⁵ that this impurity acts as a shallow acceptor when it substitutes for on the nitrogen, and therefore, becomes a source of compensation for the Si donor. In addition, cation vacancies such as V_{Ga} and V_{Al} , can act as a triple acceptor, and their formation energies reportedly decrease with increasing Al composition.²⁶

Indium-silicon co-doping has been proposed to achieve highly conductive $\text{Al}_{0.65}\text{Ga}_{0.35}\text{N}$ films. Cantu *et al.*²⁷ reported that the $\text{Al}_{0.65}\text{Ga}_{0.35}\text{N}$ layers grown at 920°C using this approach possessed n-type carrier concentrations as high as $2.5 \times 10^{19} \text{ cm}^{-3}$ with an electron mobility of $22 \text{ cm}^2/\text{V}\cdot\text{s}$, which corresponds to a resistivity of $1.1 \times 10^{-4} \Omega\cdot\text{cm}$. However, significantly higher resistivity values were measured for Si-doped

$\text{Al}_x\text{Ga}_{1-x}\text{N}$ films with $x \geq 0.49$ deposited at 1150 °C without indium. The Si-doped $\text{Al}_{0.62}\text{Ga}_{0.38}\text{N}$ films exhibited a maximum carrier concentration of $2.5 \times 10^{19} \text{ cm}^{-3}$ and a resistivity of $6.2 \times 10^{-2} \Omega\cdot\text{cm}$. It was speculated²⁷ that indium occupies cation vacancy sites and suppresses acceptor formation and self-compensation.

Heavy doping of Si was also reported to result in highly conductive $\text{Al}_{0.7}\text{Ga}_{0.3}\text{N}$ films. Zhu *et al.*²⁸ reported that an $\text{Al}_{0.7}\text{Ga}_{0.3}\text{N}$ film with a Si concentration of $6.0 \times 10^{19} \text{ cm}^{-3}$ showed a resistivity of $7.5 \times 10^{-3} \Omega\cdot\text{cm}$ with an electron concentration of $3.3 \times 10^{19} \text{ cm}^{-3}$ and a mobility of $25 \text{ cm}^2/\text{V}\cdot\text{s}$. The effective donor activation energy increased from 10meV to 25meV as the Si concentration decreased from $6.0 \times 10^{19} \text{ cm}^{-3}$ to $2.6 \times 10^{19} \text{ cm}^{-3}$, which could be explained by the bandgap renormalization effect.

Nam *et al.*²⁹ reported that the conductivity of $\text{Al}_x\text{Ga}_{1-x}\text{N}$ alloys continuously increases with an increase in the Si doping level for a fixed value of the Al content and that there exists a critical Si concentration of about $1 \times 10^{18} \text{ cm}^{-3}$ that is needed to convert insulating $\text{Al}_x\text{Ga}_{1-x}\text{N}$ alloys ($x \geq 0.4$) to n-type. However, Taniyasu *et al.*²¹ found that the electron concentration of Si-doped $\text{Al}_{0.49}\text{Ga}_{0.51}\text{N}$ alloys saturated at $4.5 \times 10^{18} \text{ cm}^{-3}$ above a Si concentration of $1.0 \times 10^{19} \text{ cm}^{-3}$, indicating the onset of self-compensation.

P-type doping of $\text{Al}_x\text{Ga}_{1-x}\text{N}$ alloys has been reported^{19, 30-32} to be even more difficult than that of n-type. Mg is generally used as a p-type dopant for GaN; however, the hole concentration that can be achieved is lower than desired, particularly for applications such as high acceptor doping near contacts for improved ohmic behavior. In $\text{Al}_x\text{Ga}_{1-x}\text{N}$ alloys, the hole concentration that can be achieved with Mg doping has been observed to decrease rapidly with increasing Al content.^{19, 30-32} Bremser *et al.*¹⁹ were unable to achieve p-type conductivity with Mg doping for $x > 0.13$. Suzuki *et al.*³¹

reported that hole concentrations as high as $6.6 \times 10^{16} \text{ cm}^{-3}$ were obtained and that the acceptor thermal activation energy was as high as 250meV in $\text{Al}_x\text{Ga}_{1-x}\text{N}$ alloys with $x = 0.15$. These investigators³¹ also found that the electrical resistivity increased with increasing x , and that the value of $15 \text{ } \Omega\cdot\text{cm}$ was obtained for $x = 0.15$; this value was considerably higher than that measured by these investigators for GaN ($\sim 2 \text{ } \Omega\cdot\text{cm}$). Lee *et al.*³³ compared the acceptor activation energies in Mg-doped, p-type $\text{In}_x\text{Ga}_{1-x}\text{N}$ ($0 \leq x \leq 0.045$) and p-type $\text{Al}_x\text{Ga}_{1-x}\text{N}$ ($0 \leq x \leq 0.095$) and suggested that the values were proportional to the bandgaps energies of these two materials. Li *et al.*³⁴ reported that they obtained p-type $\text{Al}_x\text{Ga}_{1-x}\text{N}$ alloys with x up to 0.27; the hole concentration and mobility at room temperature were $6.6 \times 10^{16} \text{ cm}^{-3}$, and $3 \text{ cm}^2/\text{V}\cdot\text{s}$, respectively, for the composition with the maximum value of x . They also observed³⁴ that the Mg activation energy in $\text{Al}_x\text{Ga}_{1-x}\text{N}$ increased almost linearly with an increase in the Al content, as shown in Fig. 1.2. The activation energy and the resistivity were estimated³⁴ to be $\sim 0.4 \text{ eV}$ and as high as $2.2 \times 10^4 \text{ } \Omega\cdot\text{cm}$, respectively.

Mg- δ -doping has been employed by Nakarmi *et al.*³⁵ to improve p-type conductivity in an $\text{Al}_{0.07}\text{Ga}_{0.93}\text{N}$ alloy. They determined that this procedure reduced the self-compensation and enhanced the p-type lateral and vertical conductivities two-fold and five-fold, respectively, in this material. High p-type conductivity was also demonstrated in Mg-doped $\text{Al}_x\text{Ga}_{1-x}\text{N}/\text{GaN}$ superlattices. Kozodoy *et al.*³⁶ calculated that a Mg-doped $\text{Al}_{0.2}\text{Ga}_{0.8}\text{N}/\text{GaN}$ superlattice would have a hole concentration of $2.5 \times 10^{18} \text{ cm}^{-3}$, which is more than ten times than that obtained experimentally in single $\text{Al}_{0.2}\text{Ga}_{0.8}\text{N}$, films, as shown in Fig. 1.3, and a lateral resistivity of $0.2 \text{ } \Omega\cdot\text{cm}$. Such an improvement was attributed to valence band bending due primarily to piezoelectric and

spontaneous polarization. Kumakura *et al.*³⁷ also demonstrated that the sheet hole concentration of Mg-doped $\text{Al}_x\text{Ga}_{1-x}/\text{GaN}$ superlattices depends strongly on the period thickness and the Al mole fraction. These investigators measured a maximum sheet hole concentration of $8 \times 10^{12} \text{ cm}^{-2}$ for $\text{Al}_x\text{Ga}_{1-x}/\text{GaN}$ (24nm/12nm) superlattices having values of the Al mole fraction between 0.15 and 0.3, which corresponds to the hole concentration of $3 \times 10^{18} \text{ cm}^{-3}$. Yasan *et al.*³⁸ demonstrated that the hole concentration and the resistivity of Mg-doped $\text{Al}_{0.26}\text{Ga}_{0.74}/\text{GaN}$ superlattices reach values as high as $4.2 \times 10^{18} \text{ cm}^{-3}$ and as low as $0.19 \Omega\cdot\text{cm}$, respectively. They confirmed via temperature-dependent capacitance-voltage measurements that superlattices with a larger period and a higher Al composition have a higher concentration of holes. Obata *et al.*³⁹ reported that the optimum annealing temperature for p-type $\text{Al}_{0.22}\text{Ga}_{0.78}\text{N}$ is $\sim 900^\circ\text{C}$, which is approximately 50°C higher than that for p-type GaN. Additional studies by these authors showed that the use of a lower V/III ratio and a higher growth temperature is preferable for the growth of high Al content, p-type $\text{Al}_{0.22}\text{Ga}_{0.78}\text{N}$, in comparison with the growth parameters for p-type GaN. By controlling the growth and the annealing conditions, they achieved hole concentrations as high as $2.0 \times 10^{18} \text{ cm}^{-3}$ for Mg-doped $\text{Al}_{0.32}\text{Ga}_{0.68}\text{N}$.

1.3 Light Emitting Diodes

1.3.1. InGaN-based Visible Light Emitting Diodes (LEDs)

Much research has been performed to achieve high brightness blue LEDs for use in full-color displays and indicators, and as light sources for lamps with the characteristics of high efficiency and high reliability. ZnSe and SiC have been

extensively investigated for these purposes for several years; however, their luminous intensity was below 1cd. In the early 1990s, the highest reported⁴⁰ output power for Zn(S, Se)-based LEDs was 120 μ W at a forward current of 40 mA. The external quantum efficiency was as high as 0.1 % and the peak wavelength was 494 nm during operation at room temperature.⁴⁰ However, II-VI-based devices were never commercialized due to their short life-time, which was caused by the propagation of structural defects, primarily dislocations, into other defects leading to failure of the devices.⁴¹⁻⁴² The output power and brightness of SiC-based blue LEDs was only between 20 and 35 μ W and \sim 30 mcd, respectively, because it is an indirect band-gap material.⁴³

Based on the considerable progress in the growth of GaN and InGaN and the p-type doping of GaN and AlGaN,⁴⁴⁻⁵⁰ Nakamura *et al.*⁵¹ demonstrated that p-GaN/n-InGaN/n-GaN double heterostructures (DH), such as those shown schematically in Fig. 1.4, resulted in high brightness blue LEDs with an external quantum efficiency as high as 0.22% at a forward current of 20 mA at room temperature. The wavelength and the full width at half maximum (FWHM) of the electroluminescence (EL) peak were 440 nm and 180meV, respectively. By comparison, the output power and the external quantum efficiency of the InGaN/GaN DH were two times higher and the peak wavelength (440nm) was much shorter than that of the Zn(S, Se)-based LEDs (494nm) at the same forward current noted above.

Blue LEDs with a luminous intensity >1 cd were also demonstrated.⁵² Zn-doped $\text{In}_{0.06}\text{Ga}_{0.94}\text{N}/\text{Al}_{0.15}\text{Ga}_{0.85}\text{N}$ DH were used to obtain a strong blue emission. Thermal annealing replaced electron beam irradiation to achieve a more uniform activation of the Mg and p-type doping in the AlGaN and GaN films. The output power was 1500 μ W

and the external quantum efficiency was as high as 2.7% at a forward current of 20 mA at room temperature. The peak wavelength and the FWHM were 450nm and 70nm, respectively.

Blue-green LEDs were fabricated by the same group.⁵³ To achieve longer wavelength emission at ~500nm, the indium mole fraction on the InGaN active layer was increased to 0.23 by decreasing the growth temperature to 780°C. Co-doping of Zn and Si in the InGaN active layer in the InGaN/AlGaN DH LEDs was conducted to increase the output power of the LEDs. Their luminous intensity, output power, and external quantum efficiency were 2 cd, 1.2mW and 2.5%, respectively, at a forward current of 20 mA at room temperature. The peak wavelength and its FWHM were 500 nm and 80 nm, respectively.

When the thickness of the InGaN active layer is reduced below a particular value, the elastic strain is not relieved by the formation of misfit and threading dislocations, the latter of which are the principal sources of recombination centers in the LEDs. Thus an improvement in power in the blue LEDs was achieved by Nakamura et al.⁵⁴ by changing the InGaN active layer to a thin undoped InGaN layer. The active layer region in the blue LEDs is now a component layer in a single QW structure consisting of a 2nm-thick undoped $\text{In}_{0.2}\text{Ga}_{0.8}\text{N}$ well layer sandwiched between 50nm-thick, n-type $\text{In}_{0.02}\text{Ga}_{0.98}\text{N}$ and 100nm-thick, p-type $\text{Al}_{0.3}\text{Ga}_{0.7}\text{N}$ barrier layers. The LEDs fabricated using the single QW produced 4.8 mW at 20mA and sharply peaked blue emission at 450 nm, corresponding to an external quantum efficiency of 8.7%. The emission peak wavelength of these blue LEDs (450nm) was longer than the band-edge emission wavelength of a stress-free $\text{In}_{0.2}\text{Ga}_{0.8}\text{N}$ active layer (420nm). They ascribed this bandgap narrowing of the

active layer to the elastic tensile stresses in this layer caused by the differences in the coefficients of thermal expansion among the well and the barrier layers. For violet LEDs, the active layer was $\text{In}_{0.09}\text{Ga}_{0.9}\text{N}$. These LEDs produced 5.6 mW of output power at 20 mA with a sharp emission peak at 405 nm and exhibited an external quantum efficiency of 9.2%.

Nakamura and co-workers⁵⁵ also fabricated high-brightness green and yellow LEDs containing QW structures by changing the indium composition in the active layer. A single QW consisting of an undoped 2nm-thick $\text{In}_{0.43}\text{Ga}_{0.57}\text{N}$ well layer sandwiched by 50nm-thick, n-type $\text{In}_{0.05}\text{Ga}_{0.95}\text{N}$ and 100nm-thick p-type $\text{Al}_{0.1}\text{Ga}_{0.9}\text{N}$ barrier layers was used to make the green LEDs, as shown schematically in Fig. 1.5. The indium mole fraction was increased to 0.7 to achieve yellow emission at the peak wavelength. The green LEDs had a wavelength of 525 nm; the FWHM of this peak was 45 nm. The output power, the external quantum efficiency and the luminous intensity of these LEDs were 1 mW, 2.1 %, and 4 cd, respectively, at 20mA. The yellow LEDs had a peak wavelength of 590 nm; the FWHM of this peak was FWHM at 90 nm. The output power was 0.5mW at 20mA. As the peak wavelength became longer, the output power decreased and the value of the FWHM increased; the latter relationship is shown in Fig. 1.6. This change in the FWHM was probably due to the large strain between the well and the barrier layers in the QW, which is caused by the mismatches in the lattice parameters and in the coefficients of thermal expansion among these layers.

High-brightness, green LEDs were achieved by replacing the n-InGaN and n-AlGaN barrier layers with n-type GaN.⁵⁶ The luminous intensity of these improved LEDs was 12 cd, or more than 100 times higher than that of the conventional green GaP

LEDs (0.1 cd). The output power, the external quantum efficiency and the peak wavelength, were 3 mW, 6.5 % and 520 nm (FWHM=30nm), respectively, at 20 mA. Using the same n-type GaN barrier structures but with a different indium composition in the QW for the fabrication of the blue LEDs resulted in an output power and an external quantum efficiency of 5 mW and 9.1%, respectively. These values were higher than those obtained from the LEDs fabricated using the InGaN/AlGaN DH (1.5 mW and 2.7%)⁵⁷ and the InGaN single QW LEDs with n-InGaN and n-AlGaN barrier layers (4 mW and 7.3%).⁵⁸

1.3.2. Al(In)GaN-based Ultraviolet Light Emitting Diodes

Compact high power UV LEDs began to be intensively investigated⁵⁹ during the latter part of the 1990s due to the need for bright and efficient UV light sources for biochemical applications, solid-state white lighting, and high capacity data storage systems. Solid solutions of AlGaN are currently the materials of choice for LEDs that emit at shorter wavelengths than 360nm. All compositions in this system possess a direct bandgap; the energies of these bandgaps range from 3.4 eV (GaN) to 6.2 eV (AlN), corresponding to the UV wavelength range of 200 to 360 nm.

LEDs containing InGaN active layers and operational at wavelengths longer than 380 nm have been successfully developed and commercialized, as described above. However, the use of AlGaN active layers for UV emitting LEDs presents two serious problems. Firstly, the output power is much lower and the external quantum efficiency is lower by a factor of more than an order of magnitude than the analogous values for InGaN-based LEDs. Despite the presence of a high-density of dislocations, which act as

non-radiative recombination centers,⁶⁰ InGaN-based LEDs have high efficiency because the InN-GaN system is unstable to decomposition into In-rich, nano-sized InGaN precipitates that form in an InGaN matrix having a lower In concentration and that have a period of separation of ~ 30 lattice spacings. This period of separation is less than the distance between the threading dislocations; thus, electron-hole recombination can occur via transitions across the bandgap of the precipitates rather than via the recombination centers produced by the threading dislocations. Thus nonradiative recombination is markedly reduced, and the relative output power is essentially the same for LEDs fabricated from material structures grown on sapphire and having a dislocation density of $\sim 10^9 \text{ cm}^{-2}$ and from similar structures grown on epitaxially laterally overgrown (ELOG) GaN layers and having a dislocation density as low as 10^5 cm^{-2} , as shown in Fig. 1.7.⁶¹ By contrast, the emission intensity from AlGaIn active layers which do not undergo phase separation is very sensitive to the dislocation density within this layer, as shown in Fig. 1.8.⁶² Moreover, free carriers in AlGaIn can easily diffuse into the non-radiative recombination centers generated by the dislocations which, in turn, results in a reduction in the output power of the AlGaIn-based UV LEDs. Another problem is that achieving p-type doping is very difficult in high Al-content AlGaIn films, as discussed above.

To increase the output power and the efficiency of UV LEDs, it has been proposed to use the indium-rich clusters that form in quaternary $\text{In}_x\text{Al}_y\text{Ga}_{1-x-y}\text{N}$ layers. Hirayama *et al.*⁶³ have demonstrated intense UV emission at room temperature in the wavelength range of 315-370 nm from quaternary $\text{In}_x\text{Al}_y\text{Ga}_{1-x-y}\text{N}$ films. These investigators found that the UV emission was considerably enhanced by the introduction of 2-5 % indium into the AlGaIn films. Maximally efficient emission was obtained at

around 330-360 nm from $\text{In}_x\text{Al}_y\text{Ga}_{1-x-y}\text{N}$ layers ($x = 2.0\% - 4.8\%$, $y = 12\% - 34\%$). They also observed indium precipitates with submicron diameters from cathodoluminescence images of quaternary InAlGaN films. The same group⁶⁴ observed intense 318 nm emission at room temperature from quaternary $\text{In}_{0.05}\text{Al}_{0.34}\text{Ga}_{0.61}\text{N}$ / $\text{In}_{0.02}\text{Al}_{0.60}\text{Ga}_{0.38}\text{N}$ three layer multiple QWs. The intensity of this emission was as strong as the 410 nm band emission from InGaN-based QWs at room temperature. Wang *et al.*⁶⁵ reported that the optical output power of UV LEDs fabricated using the InAlGaN/AlGaN quaternary system as an active region, was as high as 1 mW at an injection current of 50mA; this value is one order of magnitude higher than that of obtained from UV LEDs with a GaN/AlGaN active region.

Since AlGaN-based UV LEDs are sensitive to the density of dislocations present in the material, low dislocation density substrates were also proposed in order to reduce the dislocations that thread into the growing films, and indirectly, to increase the output power and efficiency of these devices. Kamiyama *et al.*⁶⁶ demonstrated AlGaN-based UV LEDs with an emission wavelength from 323 to 363 nm fabricated from material structures grown on heteroepitaxially laterally overgrown $\text{Al}_{0.22}\text{Ga}_{0.78}\text{N}$ layers having a dislocation density of $2 \times 10^7 \text{ cm}^{-2}$. The highest output power of 1.2 mW at 50 mA injection current was obtained at a wavelength of 363 nm. UV LED material structures have also been grown on free-standing GaN substrates produced via hydride vapor-phase epitaxy (HVPE) and having a dislocation density of $\sim 10^7 \text{ cm}^{-2}$. Nishida *et al.*⁶⁷ reported that these LEDs exhibited 3 mW output power at 352 nm using an injection current of 100mA, which is about ten times higher than that of similar devices tested under similar conditions and grown on SiC substrates. Yasan *et al.*⁶⁸ reported that the output power at

340 nm from UV LEDs grown on free-standing GaN wafers that were removed via laser ablation from sapphire substrates was more than one order of magnitude higher than that from UV LEDs on sapphire substrates, as shown in Fig. 1.9. This substantial difference was believed to be due to the higher thermal conductivity of the GaN wafers. The output power of the LEDs also saturated at higher injection currents compared to the devices grown on sapphire. The same group also reported⁶⁹ a 30% reduction in series resistance, an increase in output power of more than 200 % and saturation at higher currents at 280 nm from UV LEDs grown on thick HVPE-GaN (14 μ m) wafers on sapphire substrates relative to the values of these parameters acquired from the LEDs having the same structure but that were not removed from these substrates.

UV LEDs that exhibit even better characteristics have been fabricated using the combination of both quaternary InAlGaN active layers and low dislocation density GaN substrates. Akita *et al.*⁷⁰ compared the electrical and optical characteristics of InAlGaN-based UV LEDs fabricated from structures deposited on free-standing GaN wafers grown via HVPE on and removed from sapphire substrates and on 3.5 μ m-thick GaN templates also grown on sapphire substrates. The dislocation densities of these two GaN substrates were $<1 \times 10^6 \text{ cm}^{-2}$ and $1 \times 10^9 \text{ cm}^{-2}$, respectively. The UV LEDs on freestanding GaN showed much higher output power without saturation even at an injection current of 500mA. The output power was 1.1 mW at the emission wavelength of 351 nm and at the injection current of 100 mA, which is 30 times higher than that of UV LEDs whose material structures were deposited on a GaN template. They also demonstrated that InAlGaN-based UV LEDs grown on free-standing GaN substrates exhibited maximum

values of output power of 3.8 mW and 6.2 mW at wavelengths of 351 nm and 358 nm, respectively, for an injection current of 400 mA.⁷¹

To surmount the difficulty of p-type doing of high Al-content AlGa_N films, Mg-doped AlGa_N/Ga_N superlattice layers have been introduced during the growth of UV LED material structures. Kinoshita *et al.*⁷² have reported emission at 333 nm from AlGa_N-based UV LEDs containing Mg-doped superlattice layers. Nishida *et al.*⁷³ also fabricated AlGa_N-based LEDs from material structures grown on SiC substrates using n-type and p-type, 75 period, 1.5nm-thick Al_{0.14}Ga_{0.86}N/1.5 nm-thick Al_{0.18}Ga_{0.82}N superlattices below and above the QWs, respectively, as shown in Fig. 1.10. Low electrical resistivity due to superlattice layers and the high thermal conductivity of the SiC substrate enabled stable device operation at large current injection of up to 1.7 kA/cm².

Khan *et al.*⁷⁴⁻⁸⁰ have reported a series of studies on AlGa_N-based UV LEDs with emissions from 340 nm to 250 nm. They deposited a AlN/Al_{0.85}Ga_{0.15}N superlattice on the AlN/sapphire substrates for strain-relief at the outset of the growth of the LEDs that exhibited a 325 nm-emission.⁸¹ Three Al_{0.14}Ga_{0.86}N(3nm)/ Al_{0.19}Ga_{0.81}N(8nm) QWs and a 15nm-thick Mg-doped p-Al_{0.42}Ga_{0.58}N electron blocking layer were subsequently deposited. The output power was 1 mW and 10.2 mW at pulsed injection currents of 100 mA and 1 A, respectively. Four Al_{0.44}Ga_{0.56}N(3.5nm)/Al_{0.50}Ga_{0.50}N(6.5nm) QWs and 20nm Mg-doped p- Al_{0.53}Ga_{0.47}N electron blocking layers were used in the LEDs that emitted at 287 nm.⁸²

1.4 Outline of Dissertation

Chapter 2 contains a comparison of the microstructure and the chemistry of the GaN films grown using TEG and TMG on AlN/SiC(0001) substrates. Optimum growth temperatures wherein smooth surfaces were obtained using both precursors were determined. The growth rate, surface microstructure and concentrations of impurities of the GaN films grown using both precursors were determined using various analysis techniques.

Chapter 3 describes the growth and n-type doping of high Al content $\text{Al}_x\text{Ga}_{1-x}\text{N}$ ($x \leq 0.61$) and AlN films on Si- and C-terminated SiC(0001) substrates. The electron affinity and the work function were also measured and evaluated for electron emission applications.

Chapter 4 details the growth, fabrication and characterization of AlGaN-based UV LEDs on 6H-SiC(0001) substrates. It covers the growth and doping of $\text{Al}_x\text{Ga}_{1-x}\text{N}$ films, the development of optimum quantum well compositions and structures, the development of ohmic contacts on p-GaN and n-SiC, and the fabrication and electrical, and optical characterization of UV LEDs.

Chapter 5 describes the effect of electron blocking layers on the emission characteristics of AlGaN-based UV LEDs, which were fabricated using the results of Chapter 4. The optical characteristics of the LEDs with and without p-type and n-type AlGaN carrier blocking layers at the top and the bottom of QWs, respectively, were studied.

1.5 Summary

$\text{Al}_x\text{Ga}_{1-x}\text{N}$ alloys ($0 \leq x \leq 1$) possess direct bandgaps, the energies of which span a range from 3.4 eV (GaN), to 6.2 eV (AlN) corresponding to the range of UV wavelengths from 200 to 360 nm. A strong gas-phase pre-reaction occurs between TMA and NH_3 ; thus, optimization of the growth parameters, especially pressure, is very important to achieve $\text{Al}_x\text{Ga}_{1-x}\text{N}$ films with a high Al content. The difficulty in achieving n-type doping of high Al content $\text{Al}_x\text{Ga}_{1-x}\text{N}$ films is due to an increase in the donor activation energy with an increase in the value of x and to compensation of the Si donor by acceptor-type defects such as oxygen, carbon and cation vacancies. Indium-silicon co-doping and heavy doping of Si over $5 \times 10^{19} \text{ cm}^{-3}$ have been proposed to achieve n-type doping in $\text{Al}_x\text{Ga}_{1-x}\text{N}$ films having a value of $x > 0.5$. P-type doping is also very difficult to achieve in these $\text{Al}_x\text{Ga}_{1-x}\text{N}$ films, since the Mg activation energy increases with an increase in the Al content. Mg- δ -doping and Mg-doped $\text{Al}_x\text{Ga}_{1-x}\text{N}/\text{GaN}$ superlattices have been proposed to achieve p-type doping of $\text{Al}_x\text{Ga}_{1-x}\text{N}$.

High brightness yellow, green, and blue LEDs have been achieved with the use of InGaN active layers. The values of the power and the efficiency of AlGaN-based UV LEDs are much lower than those measured in InGaN-based visible LEDs, since the AlN-GaN system does not undergo phase separation in the manner of the InN-GaN system and which makes the nano-precipitate sources in the latter much less sensitive to recombination at the states produced in the band gap of the matrix material by the very high density of dislocations. Low dislocation density substrates and quaternary $\text{In}_x\text{Al}_y\text{Ga}_{1-x-y}\text{N}$ active layers have been proposed for high-power UV LEDs. $\text{Al}_x\text{Ga}_{1-x}\text{N}/\text{GaN}$ (or AlN) superlattices have been effectively used for p-type doping and stress relief.

1.6 References

1. A. Pikhtin, Soviet. Phys. Semicond. **11**, 245 (1977).
2. *Group III Nitride Semiconductor Compounds: Physics and Application*, edited by Bernard Gil, (Oxford University press, NY, 1998).
3. J. Hagan, R.D. Metcalfe, D. Wickenden, and W. Clark, J. Phys. C **11**, L143 (1978).
4. B. Branov, L. Doweritz, V.B. Gutan, G. Jungk, H. Neumann, and H. Raidt, Phys. Stat. Solidi (a) **49**, 629 (1978).
5. S. Yosida, S. Misawa, and S. Gonda, J. Appl. Phys. **53**, 6844 (1982).
6. S. Bass, C. Pickering, M. Young, J. Cryst. Growth **64**, 68 (1983).
7. C. Kuo, J. Yuan, R. Cohen, J. Dunn, and G. Stringfellow, Appl. Phys. Lett. **44**, 550 (1984).
8. D. Mazzaresse, A. Tripathi, W. Conner, K. Jones, L. Caleron, and D. Eckart, J. Electron. Mater. **18**, 369 (1989).
9. A. Thon and T.F. Kuech, Appl. Phys. Lett. **69**, 55 (1996).
10. L.V. Interrante, L.E. Carpenter II, C. Whitmarsh, W. Lee, M. Garbaskas, and G.A. Slack, Mater. Res. Soc. Proc. **73**, 359 (1986).
11. C.H. Chen, H. Liu, D. Steigerwald, W. Imler, C.P. Kuo, M.G. Craford, M. Ludowise, S. Lester, J. Amano, J. Electron. Mater. **25**, 1004 (1996).
12. M.A. Khans, R.A. Skogman, and R.G. Schulze, Appl. Phys. Lett **43**, 492 (1983).
13. Y. Koide, H. Itoh, N. Sawaki, I. Akasaki, and M. Hashimoto, J. Electrochem. Soc. **133**, 1956 (1986).

14. J. Han, J.J. Figiel, M.H. Crawford, M.A. Banas, M.E. Bartram, R.M. Biefeld, Y.K. Song, and A.V. Nurmikko, *J. Cryst. Growth* **195**, 291 (1998).
15. S.C. Choi, J.-H. Kim, J.Y. Choi, K.J. Lee, K.Y. Lim, and G.M. Yang, *J. Appl. Phys.* **87**, 172 (2000).
16. A.V. Kondratyev, R.A. Talalaev, W.V. Lundin, A.V. Sakharov, A.V. Tsatul'nikov, E.E. Zavarin, A.V. Fomin, and D.S. Sizov, *J. Cryst. Growth* **272**, 420 (2004).
17. H.G. Lee, M. Gershenson, and B.L. Goldengerg, *J. Electron. Mater.* **20**, 621 (1991).
18. M.D. McCluskey, N.M. Johnson, C.G. Van de Walle, D.P. Bour, M. Kneissl, and W. Walukiewicz, *Phys. Rev. Lett.* **80**, 4008 (1998).
19. M.D. Bremser, W.G. Perry, T. Zheleva, N.V. Edwards, O.-H. Nam, N. Parikh, D.E. Aspnes, and R.F. Davis, *MRS Internet J. Nitride Semicond. Res.* **1**, 8 (1996).
20. A.Y. Polyakov, N.B. Smirnov, A.V. Govorkov, M.G. Milividski, J.M. Redwing, M. Shin, M. Skowronski, D.W. Greve, and R.G. Wilson, *Solid State Electron.* **42**, 627 (1998).
21. Y. Taniyasu, M. Kasu, and N. Kobayashi, *Appl. Phys. Lett.* **81**, 1255 (2002).
22. R. Zeisel, M.W. Bayerl, S.T.B. Goennenwein, R. Dimitrov, O. Ambacher, M.S. Brandt, and M. Stutzmann, *Phys. Rev. B* **61**, R16238 (2000).
23. P. Boguslawski, and J. Bernholc, *Phys. Rev. B* **56**, 9496 (1997).
24. C.G. Van de Walle, C. Stampfl, J. Neugebauer, M.D. McCluskey, and N.M. Johnson, *MRS Internet J. Nitride Semicond. Res.* **4S1**, G10.4 (1999).
25. S. Fischer, C. Wetzel, E.E. Haller, and B.K. Meyer, *Appl. Phys. Lett.* **67**, 1298 (1996).
26. C. Stampfl, and C.G. Van de Walle, *Appl. Phys. Lett.* **72**, 459 (1998).

27. Cantu, S. Keller, U.K. Mishra, and S.P. DenBaars, Appl. Phys. Lett. **82**, 3683 (2003).
28. K. Zhu, M.L. Nakarmi, K.H. Kim, J.Y. Lin and H.X. Jiang, Appl. Phys. Lett. **85**, 4669 (2004).
29. K.B. Nam, J. Li, M.L. Nakarmi, J.Y. Lin, and H.X. Jiang, Appl. Phys. Lett. **81**, 1038 (2002).
30. T. Tanaka, A. Watanabe, H. Amano, Y. Kobayashi, I. Akasaki, S. Yamazaki, and M. Koike, Appl. Phys. Lett. **65**, 593 (1994).
31. M. Suzuki, J. Nishio, M. Onomura, and C. Hongo, J. Cryst. Growth **189/190**, 511 (1998).
32. M. Katsuragawa, S. Sota, M. Komori, C. Anbe, T. Takeuchi, H. Sakai, H. Amano, and I. Akasaki, J. Cryst. Growth **189/190**, 528 (1998).
33. S.N. Lee, J. Son, T. Sakong, W. Lee, H. Paek, E. Yoon, J. Kim, Y.-H. Cho, O. Nam, and Y. Park, J. Cryst. Growth **272**, 455 (2004).
34. J. Li, T.N. Oder, M.L. Nakarmi, J.Y. Lin, and H.X. Jiang, Appl. Phys. Lett. **80**, 1210 (2002).
35. M.L. Nakarmi, K.H. Kim, J. Li, J.Y. Lin, and H.X. Jiang, Appl. Phys. Lett. **82**, 3041 (2003).
36. P. Kozodoy, M. Hansen, S.P. DenBaars, and U. Mishra, Appl. Phys. Lett. **74**, 3681 (1999).
37. K. Kumakura, and N. Kobayashi, Jpn. J. Appl. Phys. **38**, L1012 (1999).
38. A. Yasan, R. McClintock, S.R. Darvish, Z. Lin, K. Mi, P. Kung, and M. Razeghi, Appl. Phys. Lett. **80**, 2108 (2002).

39. T. Obata, H. Hirayama, Y. Aoyagi, and K. Ishibashi, *Phys. Stat. Sol. (a)* **201**, 2803 (2004).
40. W. Xie, D.C. Grillo, R.L. Gunshor, M. Kobayashi, H. Jeon, J. Ding, A.V. Nurmikko, G.C. Hua, and N. Otsuka, *Appl. Phys. Lett.* **60**, 1999 (1992).
41. G.C. Hua, D.C. Grillo, Y. Fan, J. Han, M.D. Ringle, R.L. Gunshor, M. Hovinen, and A.V. Nurmikko, *Appl. Phys. Lett.* **65**, 1331 (1994).
42. A. Ishibashi, *IEEE Select. Topics in Quantum Electron.* **1**, 741 (1995).
43. J. Edmond, H. Kong, A. Suvorov, D. Waltz, and C. Carter Jr., *Phys. Stat. Sol. (a)* **162**, 481 (1997).
44. H. Amano, N. Sawaki, I. Akasaki, and Y. Toyada, *Appl. Phys. Lett.* **48**, 353 (1986)
45. I. Akasaki, H. Amano, Y. Koide, K. Hiramatsu, and N. Sawaki, *J. Cryst. Growth* **98**, 209 (1989)
46. H. Amano, M. Kito, K. Hiramatsu, and I. Akasaki, *Jpn. J. Appl. Phys.* **28**, L2112 (1989).
47. S. Nakamura, M. Senoh, and T. Mukai, *Jpn. J. Appl. Phys.* **30**, L1708 (1991)
48. T. Nagatomo, T. Kuboyama, H. Minamino, and O. Omoto, *Jpn. J. Appl. Phys.* **28**, L1334 (1989)
49. N. Yoshimoto, T. Matsuoka, T. Sasaki, and A. Katsui, *Appl. Phys. Lett.* **59**, 2251 (1991).
50. S. Nakamura, and T. Mukai, *Jpn. J. Appl. Phys.* **31**, L1457 (1992).
51. S. Nakamura, M. Senoh, and T. Mukai, *Jpn. J. Appl. Phys.* **32**, L8 (1993).
52. S. Nakamura, T. Mukai, and M. Senoh, *Appl. Phys. Lett.* **64**, 1687 (1994).
53. S. Nakamura, T. Mukai, and M. Senoh, *J. Appl. Phys.* **76**, 8189 (1994).

54. S. Nakamura, M. Senoh, N. Iwasa, and S. Nagahama, Appl. Phys. Lett. **67**, 1868 (1995).
55. S. Nakamura, M. Senoh, N. Iwasa, and S. Nagahama, Jpn. J. Appl. Phys. **34**, L797 (1995).
56. S. Nakamura, M. Senoh, N. Iwasa, S. Nagahama, T. Yamada, and T. Mukai, Jpn. J. Appl. Phys. **34**, L1332 (1995).
57. S. Nakamura, T. Mukai, and M. Senoh, **64**, 1687 (1994).
58. S. Nakamura, M. Senoh, N. Iwasa, and S. Nagahama, Jpn. J. Appl. Phys. **34**, L797 (1995).
59. T. Nishida, and N. Kobayashi, Phys. Stat. Sol. (a) **176**, 45 (1999).
60. T. Sugahara, M. Hao, T. Wang, D. Nakagawa, Y. Naoi, K. Nishino, and S. Sakai, Jpn. J. Appl. Phys. **37**, L1195 (1998).
61. T. Mukai, and S. Nakamura, Jpn. J. Appl. Phys. **37**, L839 (1998).
62. M. Hirayama, S. Terao, T. Sano, S. Takanami, T. Ukai, R. Nakamura, S. Kamiyama, and I. Akasaki, Phys. Stat. Sol. (a) **188**, 117 (2001).
63. H. Hirayama, A. Kinoshita, T. Yamabi, Y. Enomoto, A. Hirata, T. Araki, Y. Nanishi, and Y. Aoyagi, Appl. Phys. Lett. **80**, 207 (2002).
64. H. Hirayama, Y. Enomoto, A. Kinoshita, A. Hirata, and Y. Aoyagi, Appl. Phys. Lett. **80**, 1589 (2002).
65. T. Wang, Y.H. Liu, Y.B. Lee, J.P. Ao, J. Bai, and S. Sakai, Appl. Phys. Lett. **81**, 2508 (2002).
66. S. Kamiyama, M. Iwaya, H. Amano, and I. Akasaki, Opto-Electron. Rev. **10**, 225 (2002).

67. T. Nishida, H. Saito, and N. Kobayashi, Appl. Phys. Lett. **79**, 711 (2001).
68. A. Yasan, R. McClintock, K. Mayers, S.R. Darvish, H. Zhang, P. Kung, M. Razeghi, S.K. Lee, and J. Y. Han, Appl. Phys. Lett. **81**, 2151 (2002).
69. A. Yasan, R. McClintock, K. Mayers, S.R. Darvish, H. Zhang, P. Kung, M. Razeghi, S.K. Lee, and J. Y. Han, Opto-Electron. Rev. **10**, 287 (2002).
70. K. Akita, T. Nakamura, and H. Hirayama, Phys. Stat. Sol. (a) **201**, 2624 (2004).
71. H. Hirayama, K. Akita, T. Kyono, and T. Nakamura, Phys. Stat. Sol. (a) **201**, 2639 (2004).
72. A. Kinoshita, H. Hirayama, M. Ainoya, Y. Aoyagi, and A. Hirata, Appl. Phys. Lett. **77**, 175 (2000).
73. T. Nishida, H. Saito, and N. Kobayashi, Appl. Phys. Lett. **78**, 399 (2001).
74. V. Adivarahan, A. Chitnis, J.P. Zhang, M. Shatalov, J.W. Yang, G. Simin, and M.A. Khan, Appl. Phys. Lett. **79**, 4240 (2001).
75. A. Chitnis, R. Pachipulusu, V. Mandavilli, M. Shatalov, J.P. Zhang, V. Adivarahan, M.A. Khan, Appl. Phys. Lett. **81**, 2938 (2002).
76. V. Adivarahan, S. Wu, A. Chitnis, R. Pachipulusu, V. Mandavilli, M. Shatalov, J.P. Zhang, M.A. Khan, G. Tamilaitis, A. Sereika, I. Yilmaz, M.S. Shur, R. Gaska, Appl. Phys. Lett. **81**, 3666 (2002).
77. J.P. Zhang, A. Chitnis, V. Adivarahan, S. Wu, V. Mandavilli, R. Pachipulusu, M. Shatalov, G. Simin, J.W. Yang, and M.A. Khan, Appl. Phys. Lett. **81**, 4910 (2002).
78. A. Chitnis, J.P. Zhang, V. Adivarahan, M. Shatalov, S. Wu, R. Pachipulusu, V. Mandavilli, and M.A. Khan, Appl. Phys. Lett. **82**, 2565 (2003).

79. W.H. Sun, J.P. Zhang, V. Adivarahan, A. Chitnis, M. Shatalov, S. Wu, V. Mandavilli, J.W. Yang, and M.A. Khan, *Appl. Phys. Lett.* **85**, 531 (2004).
80. V. Adivarahan, W.H. Sun, A. Chitnis, M. Shatalov, S. Wu, H.P. Maruska, and M.A. Khan, *Appl. Phys. Lett.* **85**, 2175 (2004).
81. A. Chitnis, J.P. Zhang, V. Adivarahan, M. Shatalov, S. Wu, R. Pachipulusu, V. Mandavilli, and M.A. Khan, *Appl. Phys. Lett.* **82**, 2565 (2003).
82. W.H. Sun, J.P. Zhang, V. Adivarahan, A. Chitnis, M. Shatalov, S. Wu, V. Mandavilli, J.W. Yang, and M.A. Khan, *Appl. Phys. Lett.* **85**, 531 (2004).

Table 1.1 Lattice parameters and interplanar distances of the III-Nitride compounds and the substrates of α -Al₂O₃ and 6H-SiC used for the growth of LED material structures. All hexagonal forms of SiC and the solid solutions in the AlGaN system belong to the space group P6₃mc (186). The coefficients of linear thermal expansion of the nitrides vary with temperature in a nonlinear fashion.²

Crystalline properties		GaN	AlN	InN	α -Al ₂ O ₃	6H-SiC
Lattice parameters (Å) at room temperature	a	3.186	3.1114	3.5446	4.758	3.081
	c	5.178	4.9792	5.7034	12.991	15.092
Coefficients of thermal expansion ($\times 10^{-6} \text{ C}^{-1}$)	a	5.59	4.2	5.7	7.5	4.2
	c	3.17	5.3	3.7	8.5	4.68
Interplanar distances (Å) at room temperature	Basal	2.59	2.49	2.85	2.165	2.516
	(1-100)	2.760	2.695	3.070	1.374	2.669
	(11-20)	1.593	1.556	1.772	2.379	1.541

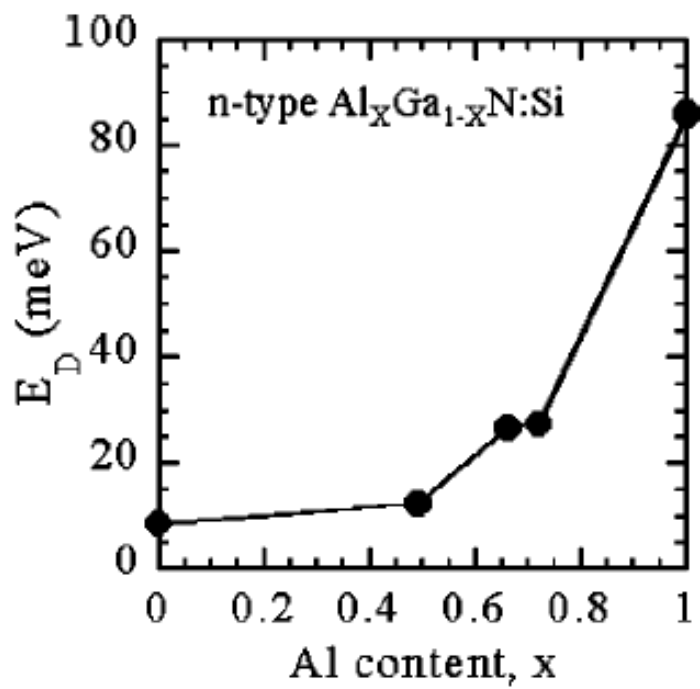


Figure 1.1 Ionization energy of the Si donor in $\text{Al}_x\text{Ga}_{1-x}\text{N}$ as a function of the Al content, x .²¹

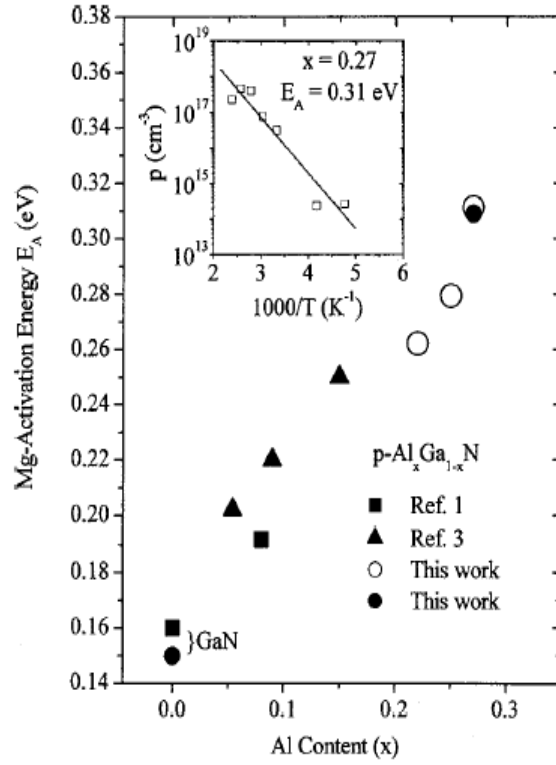


Figure 1.2 Activation energy of Mg acceptors in Mg-doped, p-type $\text{Al}_x\text{Ga}_{1-x}\text{N}$ as a function of the Al content, x . The inset shows the measured temperature dependence of the hole concentration in the p-type $\text{Al}_{0.27}\text{Ga}_{0.73}\text{N}$ sample from which an activation energy of 0.310 eV was obtained.³⁴

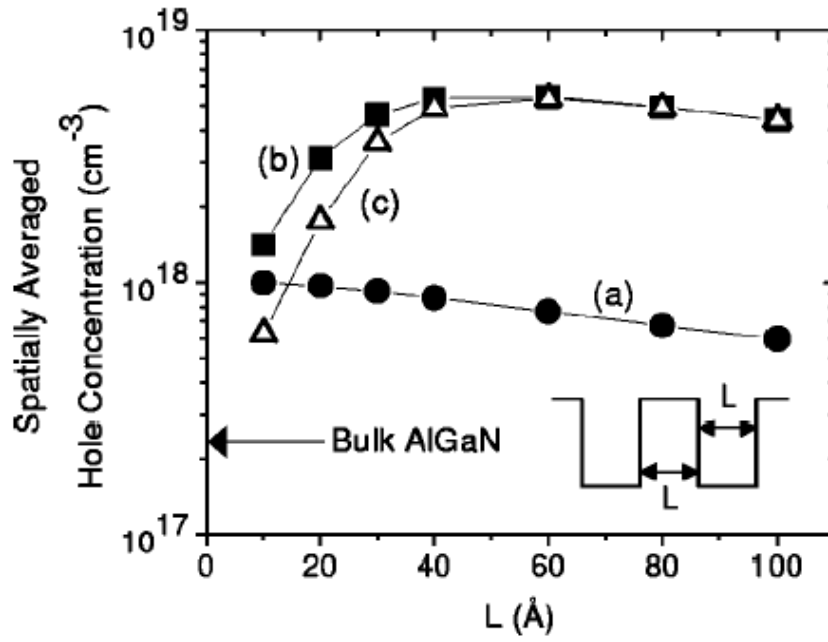


Figure 1.3 Calculations of the spatially averaged hole concentration (at 300 K) for a Mg-doped AlGaIn/GaN superlattice as a function of the superlattice dimension L . The calculations (a) ignore the polarization fields, (b) include them, and (c) include both polarization fields and quantization effects. The hole concentration calculated for a bulk AlGaIn film is indicated by the arrow.³⁶

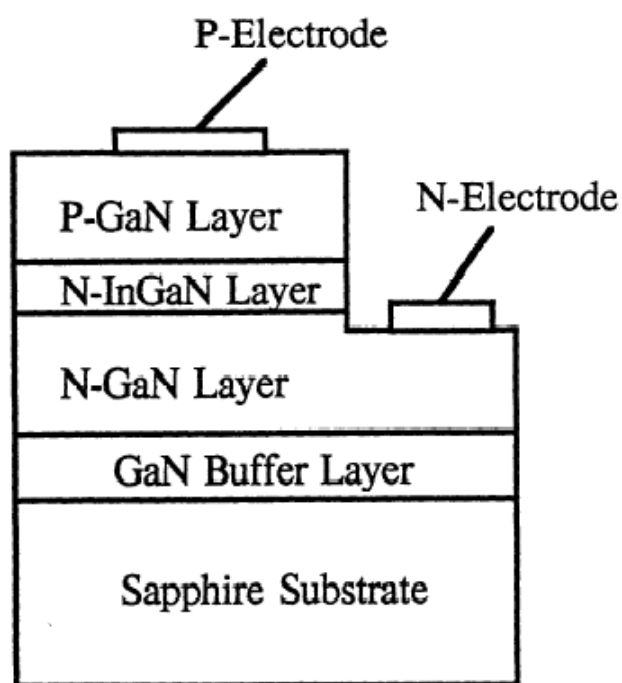


Figure 1.4 Schematic of a representative p-GaN/n-InGaN/n-GaN double heterostructure developed for blue LEDs by Nakamura *et al.*⁵¹

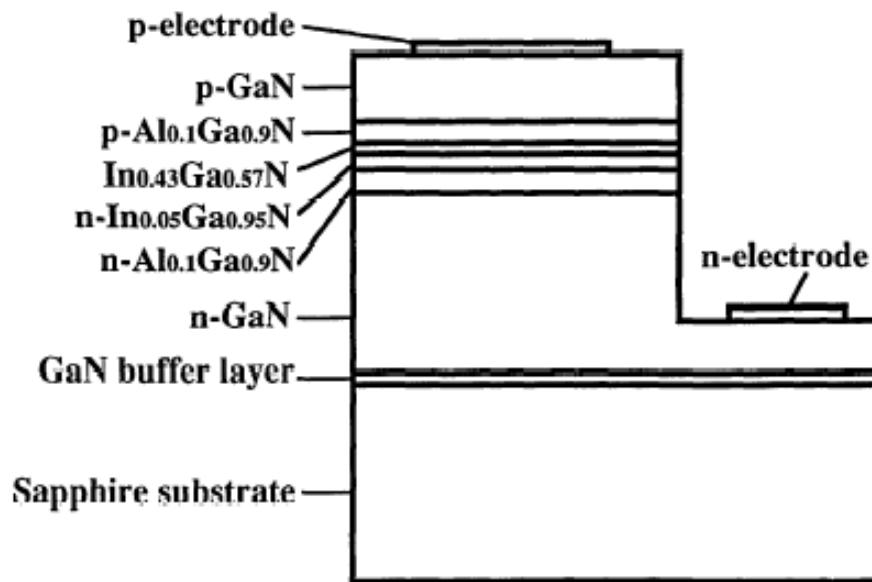


Figure 1.5 Schematic of the material structure used to fabricate green, single QW LEDs.⁵⁵

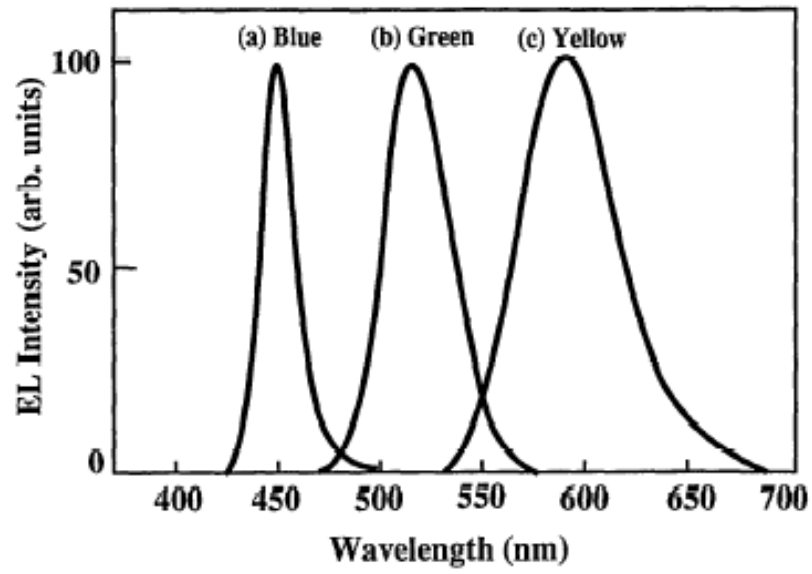


Figure 1.6 Electroluminescence of (a) blue, (b) green, and (c) yellow single QW LEDs at a forward current of 20 mA.⁵⁵

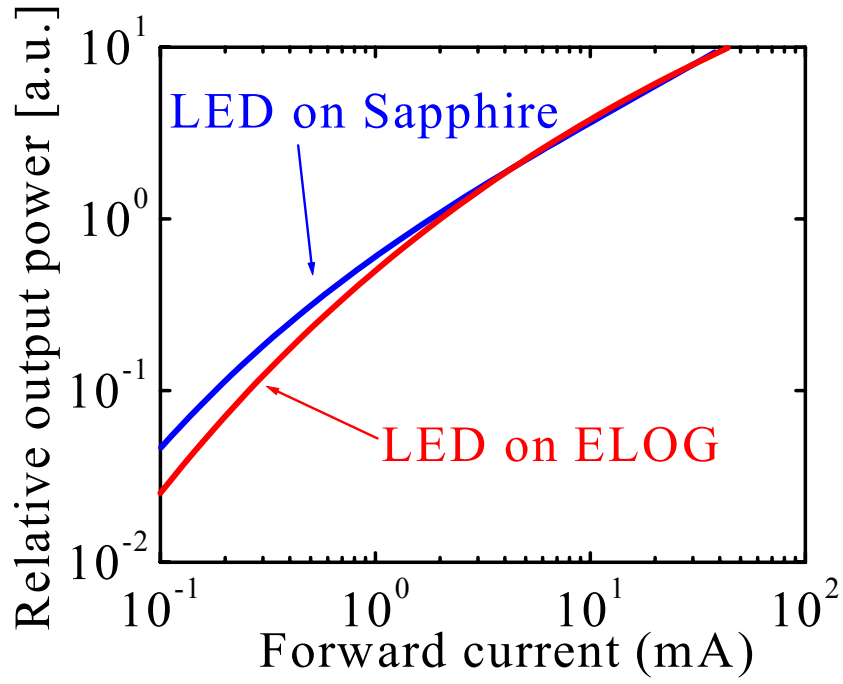


Figure 1.7 The relative output power of blue InGaN single QW LEDs grown on ELOG GaN with a lower dislocation density and on sapphire substrates as a function of the forward current. Note that the LEDs on sapphire substrates show almost the same output power as the LEDs on the ELOG GaN despite the much higher dislocation density of the latter material.⁶¹

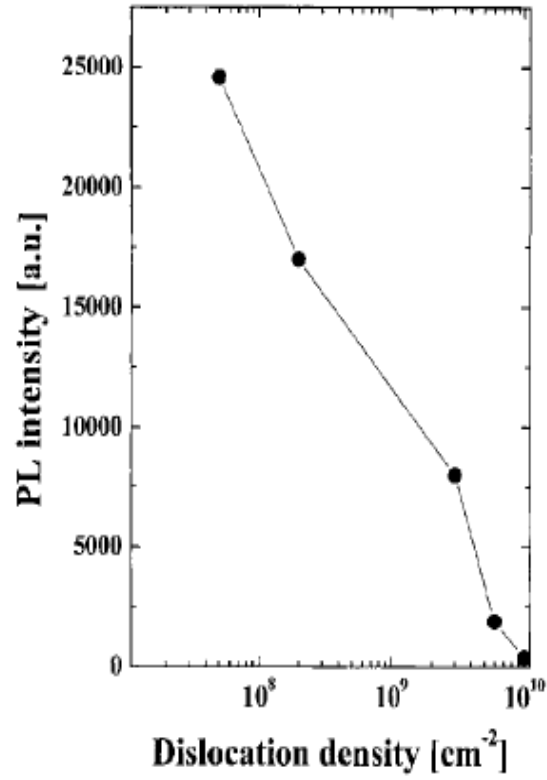


Figure 1.8 The relationship between the intensity of the photoluminescence peak and the threading dislocation density in GaN/Al_{0.08}Ga_{0.82}N multi-QWs grown on Al_{0.22}Ga_{0.78}N films.⁶²

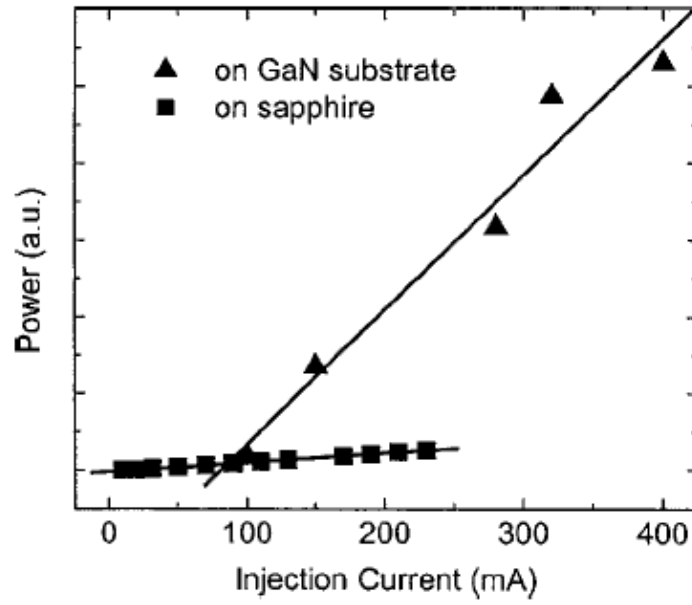


Figure 1.9 Comparison of the output power at 340 nm from LEDs grown on free-standing GaN substrates (triangles) and on sapphire (squares) in pulsed injection mode.⁶⁸

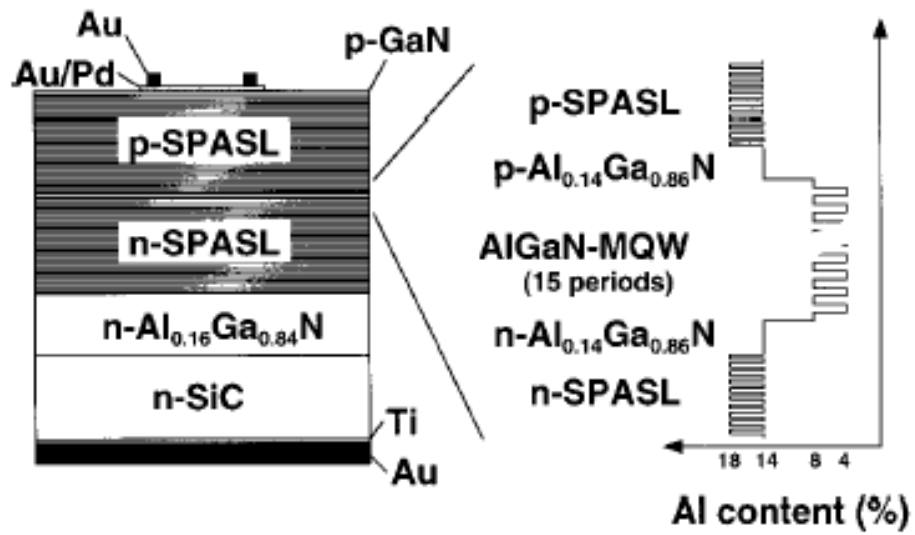


Figure 1.10 Schematic drawing of the LED structure grown by Nishida *et al.*⁷³ containing n- and p-type short period alloy superlattices (SPASL) below and above the multi-quantum wells. The SPASLs were used as transparent conductive layers.

2. Comparison of the Microstructure and Chemistry of GaN(0001) Films Grown using Trimethylgallium and Triethylgallium on AlN/SiC Substrates

Ji-Soo Park, Zachary J. Reitmeier and Robert F. Davis

*Department of Materials Science and Engineering, North Carolina State University,
Raleigh, NC 27695-7907*

Abstract

The metalorganic chemical vapor deposition of GaN(0001) films using triethylgallium (TEG) and trimethylgallium (TMG) precursors on AlN/6H-SiC(0001) substrates has been conducted using various sets of two temperatures, and the microstructural and chemical differences in the films determined. Growth of films at 980°C and 1020°C using TEG and TMG, respectively, resulted in the formation of separate elongated islands. Growth at the optimum temperatures (for our system) of 1020°C and 1050°C using these two respective precursors resulted in smooth surface microstructures. Analogous depositions at 1050°C and 1080°C resulted in the formation of hillocks over most of the surfaces. In the GaN films grown using TEG at 1020°C the concentrations of carbon ($3 \times 10^{17} \text{ cm}^{-3}$) and hydrogen ($1 \times 10^{18} \text{ cm}^{-3}$) were ~ 10 times and ~ 2 times lower than in the films deposited using TMG at 1050°C. The concentrations of oxygen and silicon were $1 \times 10^{17} \text{ cm}^{-3}$ in the films grown using either precursor. Atomic force microscopy of the films grown using TEG and TMG at 1020°C and 1050°C, respectively, revealed a similar surface roughness with rms values of $\sim 1.8 \text{ nm}$ within $50 \mu\text{m} \times 50 \mu\text{m}$ scans. The full width at half maxima determined from omega scans of the GaN(0002) peak were ~ 250 arcsec for films grown using both precursors.

2.1 Introduction

Triethylgallium (TEG) and trimethylgallium (TMG) are the Ga-containing precursors of choice for the growth of GaN films. Three different deep levels in the bandgap have been determined in GaN grown using TMG (TMG GaN); however, only one of these levels has been detected in GaN grown using TEG (TEG GaN).¹⁻² Ishibashi *et al.*³ reported that carbon from TMG that resides on the nitrogen sites in GaN is responsible for an acceptor level and carbon from TEG that resides on interstitial sites forms deep levels because of the C-C bonding in the ethyl radicals. Saxler *et al.*⁴ showed that TEG GaN had superior electrical and optical properties and a lower concentration of carbon compared to TMG GaN. Song *et al.*⁵ reported that TEG GaN is superior in terms of structural and electrical properties; however, TMG GaN is better in terms of morphological and optical properties. In each of these studies the GaN films were grown under the same conditions (in a given study) rather than the optimum conditions for each Ga precursor. As such, the concentrations of the incorporated impurities and the surface microstructures of the films may be different in the use of a given precursor than would be determined for films grown with this precursor under optimum conditions.

In this study, GaN films were grown on AlN/SiC(0001) substrates using TEG and TMG at the optimum temperatures (in our reactor) for each precursor, and the properties of the films compared.

2.2 Experimental Procedures

100nm thick AlN buffer layers and 1 μ m thick GaN layers were sequentially deposited on on-axis 6H-SiC(0001) substrates in a cold-walled, vertical, pancake-style

metal-organic vapor phase epitaxy reactor. The reactants (chemical symbol and flow rates) were trimethylaluminum ($(\text{CH}_3)_3\text{Al}$; $5.4\mu\text{mol/min}$), TMG ($(\text{CH}_3)_3\text{Ga}$), TEG ($(\text{C}_2\text{H}_5)_3\text{Ga}$) and ammonia (NH_3 ; 0.14mol/min); hydrogen served as both the carrier and the diluent. The flow rates of both Ga precursors were varied from 26-to-101 $\mu\text{mol/min}$; the flow rate of NH_3 was held constant. The reactor pressure was fixed at 20Torr. The growth temperatures of the AlN and the GaN layers were 1100°C and $980\text{-}1080^\circ\text{C}$, respectively. Secondary ion mass spectroscopy (SIMS) was performed to measure the concentrations of carbon, oxygen, hydrogen and silicon in the GaN films. The surface roughness and the full width at half maximum (FWHM) of the GaN(0002) peak were measured using atomic force microscopy (AFM) and x-ray diffraction analysis, respectively.

2.3 Results and Discussion

Figure 2.1 shows three different characteristics in surface microstructure of TEG GaN and TMG GaN films as a function of growth temperature. Elongated, three-dimensional islands, possibly formed from the coalescence of a very few individual islands, were observed after deposition at 980°C and 1020°C using TEG and TMG, respectively, as shown in Figure 2.1 (a). Figure 2.1 (b) reveals that increasing the growth temperatures to the optimum values (for our reactor geometry and growth conditions) of 1020°C and 1050°C resulted in complete films with smooth surfaces. These results are due to a significant increase in the lateral growth rate from the sidewalls of the islands and subsequent coalescence of these features.⁶ Growth at 1050°C and 1080°C using TEG and TMG, respectively, caused the formation of hillocks over most of the surfaces.

In summary, the surface microstructures of the films deposited using TEG GaN and TMG GaN are essentially the same, if the deposition temperatures employed with the latter precursor are 30°C-40°C higher than those used with the former precursor. All films discussed in the following paragraphs were grown at the optimum temperature for the precursor employed.

The effect of varying the V/III ratio on the deposition time necessary to achieve a 1 μm thick GaN film for both precursors is shown in Figure 2.2. The quasi-linear relationships indicate that the growth rates are controlled by the flux of the Ga species to the surfaces of the growing films. Growth using TEG requires about a 1.6 times longer period than TMG to achieve a 1 μm thick film at the optimum temperatures. To compare TEG GaN and TMG GaN directly, GaN films were deposited at the optimum growth temperature of each precursor using the V/III ratios of 1323 for TEG GaN and 2045 for TMG GaN. These values were chosen because TEG GaN and TMG GaN show almost the same growth rate at the respective ratios. All films discussed in the following paragraphs were grown using these respective V/III ratios.

Figure 2.3 shows the SIMS depth profiles of silicon, oxygen, carbon and hydrogen in the GaN films. Silicon⁹ and oxygen¹⁰ have been shown to be shallow donors in GaN. The silicon concentrations in both GaN films, were approximately the same value of $1 \times 10^{17} \text{cm}^{-3}$. Ishibashi *et al.*³ reported that TEG GaN has a seven times higher silicon concentration than TMG GaN. This indicates that the silicon originates from the metalorganic sources. However, our results show that high-purity TEG and TMG are not major sources of silicon and that the contributions by these precursors, if any, are approximately the same at the optimum growth temperatures and V/III ratios for

our system. It has been suggested that the SiC susceptor may be a significant source of background silicon during GaN growth, since heating this susceptor in the more corrosive NH_3/H_2 mixture may produce a silicon background concentration larger than produced in pure H_2 .¹¹

The oxygen concentrations were also approximately $1 \times 10^{17} \text{cm}^{-3}$ in both TEG GaN films and TMG GaN films. Saxler *et al.*⁴ reported that the oxygen concentration is seven times higher in TMG GaN films than in TEG GaN films. However, our results again show no significant difference in oxygen concentrations in these films.

The concentrations of C in the TEG GaN and the TMG GaN films are $\sim 3 \times 10^{17} \text{cm}^{-3}$ and $\sim 2 \times 10^{18} \text{cm}^{-3}$, respectively. Several groups³⁻⁵ have compared TEG and TMG for GaN growth. Two groups⁴⁻⁵ observed less carbon in their films when TEG was used; however, Ishibashi *et al.*³ observed more carbon when TEG was used relative to that measured after the use of TMG. Carbon most likely incorporates on the N lattice⁷ and has been investigated⁸ as an acceptor in GaN.

Metal-alkyl metalorganic compounds decompose by either β -hydride elimination or homolysis.¹² β -hydride elimination forms alkene and hydride ligands as reaction products, e.g., C_2H_4 and $\text{GaH}(\text{C}_2\text{H}_5)_2$, respectively, in TEG. This process occurs from adsorbed molecules on the surface at temperatures below those used in this research. This process would also likely result in an increase in the hydrogen concentration in the GaN films, which was not observed. Thus, the expected reaction pathway for GaN growth using TEG is both β -hydride elimination and homolysis which occurs via cleavage of carbon-metal bonds in the gas phase to generate free, relatively stable ethyl (C_2H_5) radicals.¹³ Pyrolysis of TMG involves breaking the Ga-C bond resulting in the

loss of a methyl radical (CH_3), which is very reactive. It is also possible that GaC is produced on the surface of the growing films in tandem with hydrogen incorporation into the films, as discussed for the growth of GaAs by Kuech.¹⁴ However, the temperatures used for growth of GaN from TMG in this research were significantly higher than those used for the growth of GaAs films. Carbon incorporation on into GaN films is also dependent on the growth conditions. The C concentration is lower in TEG GaN films grown at lower temperatures, lower pressures and lower NH_3 flow rates; these conditions do not favor high rates of H_2 dissociation on the GaN surface.¹⁵ Thus, the use of relatively low growth pressures, e.g., 20 Torr, may contribute to lowered carbon concentration in TEG GaN films than in TMG GaN films.

The hydrogen concentration in the TEG GaN films ($2 \times 10^{18} \text{cm}^{-3}$) was approximately half that measured in the TMG GaN ($1 \times 10^{18} \text{cm}^{-3}$) films. Koleske *et al.*¹¹ have determined that the hydrogen concentration in GaN films is independent of growth conditions when the same precursors are used for all depositions. As the carbon concentration in our TEG GaN films is lower than in our TMG GaN films, the higher hydrogen concentration measured in the latter may result from the incorporation of hydrogen bonded with carbon and derived from the Ga precursors.

Figure 2.4 shows the values of both the FWHM of the GaN(0002) peaks and the rms roughness of the surfaces of the films grown using TEG and TMG. The values of the former were both ~ 250 arcssec. The values of the latter were ~ 1.8 nm within $50 \mu\text{m} \times 50 \mu\text{m}$ scans for films grown using both precursors.

2.4 Conclusions

The surface microstructures of GaN(0001) films deposited using TEG and TMG are essentially the same, if the deposition temperatures employed with the latter precursor are 30°C-40°C higher than used with the former precursor. In the TEG GaN films grown at 1020°C the concentrations of carbon and hydrogen were ~10 times and ~2 times lower than in the TMG GaN grown at 1050°C, while the concentrations of oxygen and silicon were similar in the films grown using either precursor. Both GaN films grown at 1020°C using TEG and at 1050°C using TMG, respectively, showed similar value for rms surface roughness and FWHM of the GaN(0002) peak.

Acknowledgements

This research was supported by the Office of Naval Research under contract N00014-98-1-0654, Harry Dietrich, monitor. R.F. Davis was partially supported by the Kobe Steel Ltd. University Professorship. The authors also wish to thank the reviewer for thoughtful and very helpful comments, some of which have been incorporated into the revised paper.

2.5 References

1. W.I. Lee, T.C. Huang, J.D. Guo, and M.S. Feng, Appl. Phys. Lett. **67**, 1721 (1995).
2. J.F. Chen, N.C. Chen, W.Y. Huang, W.I. Lee, and M.S. Feng, Jpn. J. Appl. Phys. **35**, L810 (1996).

3. A. Ishibashi, H. Takeishi, M. Mannoh, Y. Yabuuchi, and Y. Ban, *J. Electron. Mater.* **25**, 799 (2001).
4. A. Saxler, D. Walker, P. Kung, X. Zhang, M. Razeghi, J. Solomon, W.C. Mitchel, and H.R. Vydyanath, *Appl. Phys. Lett.* **71**, 3272 (1995).
5. K.-M. Song, D.-J. Kim, Y.-T. Moon, and S.-J. Park, *J. Crystal Growth* **233**, 439 (2001).
6. P.Q. Miraglia, E.A. Preble, A.M. Roskowski, S. Einfeldt, and R.F. Davis, *J. Crystal Growth* **253**, 16 (2003).
7. K.H. Ploog, and O. Brandt, *J. Vac. Sci. Technol.* **A16**, 1609 (1998).
8. U. Birkle, M. Fehrer, V. Kirchner, S. Einfeldt, D. Hommel, S. Strouf, P. Michler, and J. Gutowski, *MRS Internet Nitride Semicond. Res.* **4S1**, G56 (1999).
9. N. Koide, H. Kato, M. Sassa, S. Yamasaki, K. Kanabe, M. Hshimoto, H. Amano, K. Hiramatsu, and I. Akasaki, *J. Crystal Growth* **115**, 639 (1991).
10. R. Niebuhr, K.H. Bachem, U. Kaufmann, M. Maier, C. Merz, B. Santic, P. Shclotter, and H. Jurgensen, *J. Electron. Mater.* **26**, 1127 (1997).
11. D.D. Koleske, A.E. Wikenden, R.L. Henry, and M.E. Twigg, *J. Crystal Growth* **242**, 55 (2002).
12. P.J. Davison, M.F. Lappert, R. Pearce, *Chem. Rev.* **76**, 219 (1976).
13. K.C. Wong, B.G. McBurnett, R.D. Culp, A.H.Cowley, and J.G. Ekerdt, *Surf. Sci.* **416**, 480 (1998).
14. T. F. Kuech and J. M. Redwing, *J. Crystal Growth* **145**, 382 (1994).

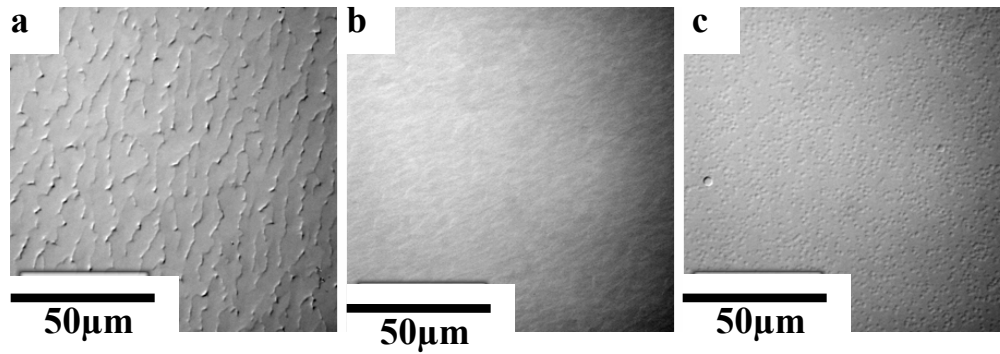


Figure 2.1 Optical micrographs obtained using Nomarski interference filter and showing the effect of growth temperature on the surface microstructure of 1 μ m GaN films deposited using TEG at (a) 980°C, (b) 1020°C and (c) 1050°C. Similar surface microstructures were obtained using TMG at 1020°C, 1050°C, and 1080°C, respectively.

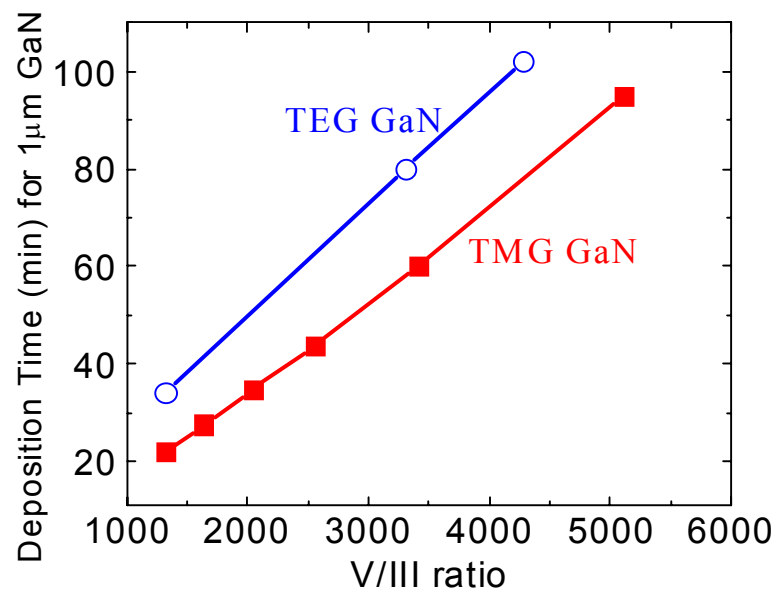


Figure 2.2 Time necessary to grow 1 μm thick GaN films at 1020°C using TEG and at 1050°C using TMG as a function of V/III ratio.

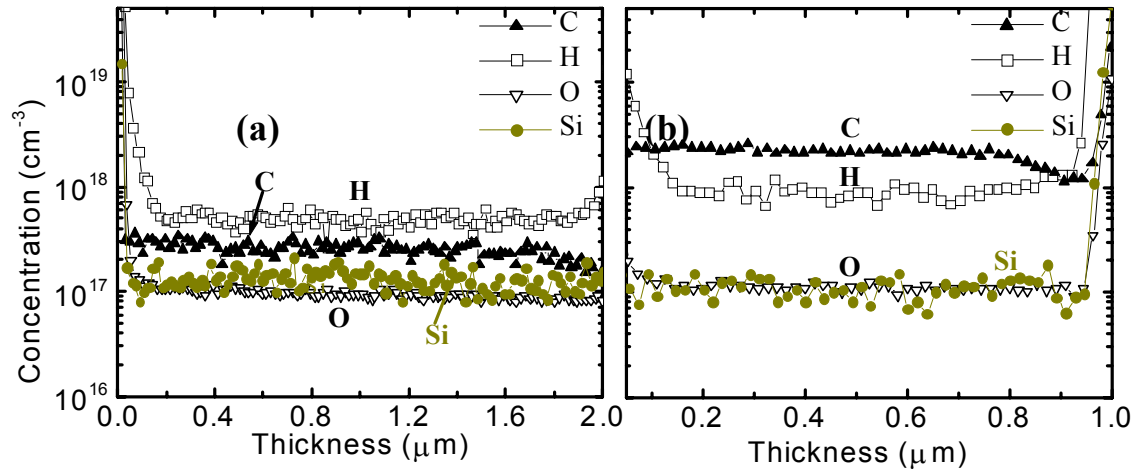


Figure 2.3 SIMS depth profiles of carbon, oxygen, hydrogen and silicon in (a) TEG GaN grown at 1020°C ($\text{V/III}=1323$) and (b) TMG GaN grown at 1050°C ($\text{V/III}=2045$).

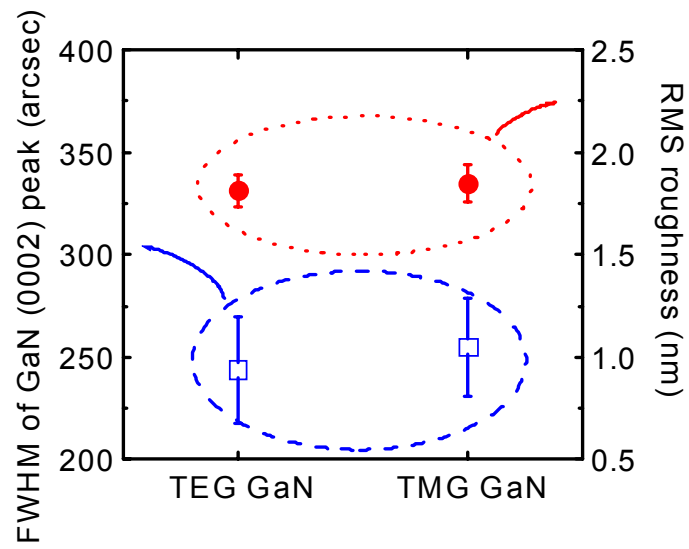


Figure 2.4 FWHM of GaN(0002) peak and RMS roughness in $50\mu\text{m} \times 50\mu\text{m}$ scans of TEG GaN grown at 1020°C ($V/\text{III}=1323$) and TMG GaN grown at 1050°C ($V/\text{III}=2045$). Number of measurements is 10; the error bars show standard deviation.

3. Growth, Doping and Characterization of $\text{Al}_x\text{Ga}_{1-x}\text{N}$ ($0 < x \leq 1$) Alloys on Si- and C-terminated 6H-SiC{0001} Substrates for Electron Emission Applications.

Ji-Soo Park, Yingjie Tang¹, Robert J. Nemanich¹, and Robert F. Davis

*Department of Materials Science and Engineering, North Carolina State University,
Raleigh, NC 27695-7907*

¹*Department of Physics, North Carolina State University, Raleigh, NC 27695-8202*

Abstract

$\text{Al}_x\text{Ga}_{1-x}\text{N}$ films ($x < 0 \leq 1$) have been grown on Si- and C-terminated 6H-SiC{0001} substrates and characterized for electron emission applications. The large range in the values of x was achieved by changing the fraction of Al in the gas phase from 0.0 to 0.45. The ionized donor concentration in the n-type, Si-doped $\text{Al}_x\text{Ga}_{1-x}\text{N}$ films decreased as the mole fraction of Al was increased due to the reduction in the donor energy level and compensation. The upper limit of the mole fraction of Al wherein n-type doping could be achieved was ~ 0.61 using the SiH_4 flow rate which yields a Si concentration of $\sim 1 \times 10^{19} \text{ cm}^{-3}$ in GaN. The electron affinity of the Si-doped $\text{Al}_{0.61}\text{Ga}_{0.39}\text{N}$ films was as low as 0.1 eV. Increasing the Si doping concentration in AlN films to as high as $1 \times 10^{21} \text{ cm}^{-3}$ caused slight but increasing degradation in crystal perfection. No difference was found in the Al core level binding energies between heavily undoped and Si-doped AlN films. Both XPS and UPS showed that the work function of N-terminated AlN films was 0.6 eV lower than that of Al-terminated films.

3.1 Introduction

Interest in electron field emitters produced using wide-band gap semiconductors such as $\text{Al}_x\text{Ga}_{1-x}\text{N}$ has been increasing, because the electron affinity of these materials is expected to be very small or even negative.¹⁻² $\text{Al}_x\text{Ga}_{1-x}\text{N}$ solid solutions possess values of the electron affinity that are directly proportional to the mole fraction of Al.³ Different compositions of these alloys have been reported⁴ to be appropriate for either anode or cathode components of a thermionic energy converter.

Donor-type $\text{Al}_x\text{Ga}_{1-x}\text{N}$ thin films wherein $x \leq 0.5$ has been achieved via Si doping during growth using either metalorganic vapor phase epitaxy⁵ or molecular beam epitaxy.⁶ By contrast, in $\text{Al}_x\text{Ga}_{1-x}\text{N}$ solid solutions for which $x > 0.5$, the electron concentration decreases sharply and the resistivity increases by five orders of magnitude, with increasing values of x .⁷⁻⁸

The III-nitrides occur primarily in the wurzite crystal structure. As such, spontaneous polarization along $\langle 0001 \rangle$ is an inherent characteristic of the III-nitride compounds and the solid solutions composed of these compounds. Moreover, the gradient in the polarization induces bound surface charges which create strong internal electric fields, which, in turn, modify the energy bands at the surface.⁹ As a result, metal-terminated materials, e.g., the $\text{Al}_x\text{Ga}_{1-x}\text{N}$ solid solutions, exhibit higher surface electron affinities than the N-terminated compositions as a result of surface band bending.¹⁰ Fortunately, Ga(Al)- and N-terminated films can be grown using Si- and C-terminated SiC substrates, respectively.¹¹⁻¹²

In this research, Si-doped $\text{Al}_x\text{Ga}_{1-x}\text{N}$ films ($0 < x \leq 1$) were grown on Si- and C-terminated SiC substrates. The upper limit of the mole fraction of Al for n-type doping

as well as the electron affinity and the work function of particular compositions were determined as indicators of the efficacy of these compositions for electron emission applications.

3.2 Experimental Procedures

All the $\text{Al}_x\text{Ga}_{1-x}\text{N}$ films used in this research were grown by metalorganic vapor phase epitaxy using a cold-walled, vertical, pancake-style system that was evacuated to 10^{-6} Torr prior to growth. The on-axis, n-type 6H-SiC(0001) substrates were etched in an $\text{HF}:\text{H}_2\text{O}$ (1:10) solution for 10 min at room temperature, rinsed in de-ionized water and blown dry with nitrogen prior to loading into the growth reactor. Trimethylaluminum (TMA), triethylgallium (TEG), and ammonia were used as the precursors; hydrogen served as both the carrier and the diluent gas. The reactor pressure was fixed at 20 Torr for the growth of all films. The temperature of the SiC-coated graphite susceptor was measured using a single wavelength optical pyrometer.

Each undoped and Si-doped 100nm-thick $\text{Al}_x\text{Ga}_{1-x}\text{N}$ ($0 < x \leq 0.61$) layer was grown on a 100nm-thick Si-doped $\text{Al}_{0.15}\text{Ga}_{0.85}\text{N}$ buffer layer ($N_D - N_A = 5 \times 10^{18} \text{ cm}^{-3}$), which was optimized for growth directly on the SiC substrates.¹³ The growth temperature of the $\text{Al}_{0.15}\text{Ga}_{0.85}\text{N}$ buffer layer and the $\text{Al}_x\text{Ga}_{1-x}\text{N}$ layers was fixed at 1020°C. The flow rates of the TEG and the TMA were varied to change the mole fractions of Al and Ga in the films. For growth of $\text{Al}_x\text{Ga}_{1-x}\text{N}$ layers with $0 < x \leq 0.5$, the sum of the molar flow rates of TEG and TMA was fixed at 31.3 $\mu\text{mol}/\text{min}$, and the flow rates of these precursors were varied from 31.3 to 20.3 $\mu\text{mol}/\text{min}$ and from 0 to 11.0 $\mu\text{mol}/\text{min}$, respectively. The last value was the maximum molar flow rate of TMA that

could be measured using the flow meter on our system. Thus, to achieve the growth of $\text{Al}_x\text{Ga}_{1-x}\text{N}$ films with $0.5 < x \leq 0.61$, the total flow rate from both metalorganic sources was fixed at $24.1 \mu\text{mol}/\text{min}$ and the molar flow rates of TEG and TMA were changed independently to achieve the desired composition of each film. The NH_3 flow rate was fixed at 3 slm. Silicon doping was achieved using a mixture of 5 ppm SiH_4 balanced in H_2 .

The 100nm-thick AlN films were grown directly on the SiC(0001) substrates at 1100°C using the molar flow rate of TMA of $5.4 \mu\text{mol}/\text{min}$. Heavy doping of these films with Si was achieved using 1000 ppm SiH_4 balanced in H_2 . Al- and N-terminated AlN films were grown on Si- and C-terminated SiC substrates, respectively.

The crystal perfection of the Si-doped AlN films was evaluated from rocking curves acquired using x-ray diffraction (Phillips X'Pert MRD). The ionized donor concentration ($N_D - N_A$) of the $\text{Al}_x\text{Ga}_{1-x}\text{N}$ films was determined using capacitance-voltage (C-V) measurements (MDC Model CSM/2-VF6) in tandem with a mercury probe. The Al mole fraction, x , of the various compositions of the $\text{Al}_x\text{Ga}_{1-x}\text{N}$ layers was calculated using Eq. (1). The values of the bandgap energies, E_g , of the solid solutions of concern were determined from the wavelengths of the respective peaks of the bandedge emission acquired via cathodoluminescence (CL) studies conducted at room temperature using a Kimball Physics EMG-14 electron gun as an excitation source. The bowing parameter, b , was assumed to be zero.

$$E_g(\text{Al}_x\text{Ga}_{1-x}\text{N}) = x \cdot E_g(\text{AlN}) + (1-x) \cdot E_g(\text{GaN}) - b \cdot x \cdot (1-x) \quad (1)$$

The Si concentration of the AlN films was analyzed using secondary ion mass spectrometry (SIMS, Cameca ims-6f). The reference sample was fabricated for the SIMS

study via ion implantation of Si^+ at an energy of 90 keV and a fluence of $8 \times 10^{14} \text{ cm}^{-2}$ into a 300nm-thick AlN film grown on a SiC substrate. X-ray photoelectron spectroscopy (XPS) and ultraviolet photoelectron spectroscopy (UPS) measurements were conducted by Tang to measure the binding energy, the electron affinity, and the work function of the $\text{Al}_x\text{Ga}_{1-x}\text{N}$ and AlN films.

3.3 Results and Discussion

3.3.1. $\text{Al}_x\text{Ga}_{1-x}\text{N}$ films ($0 < x \leq 0.61$)

Figure 3.1(a) shows the CL spectrum acquired at room temperature from an undoped $\text{Al}_{0.41}\text{Ga}_{0.59}\text{N}$ film. The bandedge emission peak is located at 273 nm. Figure 3.1(b) shows the relationship between the Al mole fraction of the $\text{Al}_x\text{Ga}_{1-x}\text{N}$ films and the fraction of Al in the growth ambient. It was determined that a maximum in the mole fraction of Al of 61% could be achieved by increasing the Al fraction in the growth ambient to 45%.

The efficiency of n-type doping of the $\text{Al}_x\text{Ga}_{1-x}\text{N}$ films using a constant flow rate of SiH_4 was determined as a function of the Al mole fraction from measurements of the ionized donor concentration, $N_D - N_A$. The results of this study are shown in Fig. 3.2. The (0001) surface of GaN begins to roughen when the volume concentration of Si exceeds $1 \times 10^{19} \text{ cm}^{-3}$. Thus, the molar flow rate of SiH_4 was kept constant at 1.43 nmol/min; this procedure resulted in a Si concentration of approximately $1 \times 10^{19} \text{ cm}^{-3}$ in GaN. The value of $N_D - N_A$ decreased with increasing mole fraction of Al in $\text{Al}_x\text{Ga}_{1-x}\text{N}$; at ~0.60 mole fraction of Al a value of this electrical parameter could not be determined, as it was below the detection limit ($\sim 1 \times 10^{17} \text{ cm}^{-3}$) of our C-V equipment, as shown in Fig. 3.2.

This inverse functional relationship between $N_D - N_A$ and the mole fraction of Al in the solid solution has been reported by several research groups.⁷⁻⁸ The principal reason for this relationship is the increase in the donor ionization energy with an increase in the Al mole fraction in the films. And this increase becomes more significant as the Al mole fraction exceeds ~50%.⁷⁻⁸ In addition, as the Al mole fraction increases, the Si donors are compensated by acceptor-type defects such as oxygen in alloys having a mole fraction of Al in excess of 30%,¹⁵ carbon,¹⁶ and cation vacancies.¹⁷ Thus, the efficiency of donor doping by Si decreases as the mole fraction of Al increases. The results shown in Fig. 3.2 make obvious the fact that if measurable donor doping is to be achieved in $Al_xGa_{1-x}N$ alloys having an Al mole fraction ≥ 0.60 , the flow rate of SiH_4 must be increased above 1.34 nmol/min.

To confirm that our $Al_xGa_{1-x}N$ films were n-type, CL measurements were performed at room temperature. Figure 3.3 (a) shows the CL spectra of Si-doped and undoped $Al_{0.41}Ga_{0.59}N$ films. The peak of band-edge emission from the undoped film occurred at 273 nm; however, the analogous peak for the Si-doped sample occurred at the slightly higher wavelength at 281 nm, and the intensity of latter peak was much stronger than that of the former. The reason for the red shift in the wavelength of the doped sample can be understood by consideration of the information presented in Figure 3.3 (b), which is a schematic of the band diagram of energy versus momentum of the electrons. In the case of the Si-doped $Al_{0.41}Ga_{0.59}N$ sample, there is band-tailing at the lowest part of the conduction band due to a high concentration of donor states. Thus, the effective bandgap energy in this alloy is slightly smaller than that of the undoped sample. This

leads to a bandedge emission peak at a slightly longer wavelength, and to luminescence that is much stronger due to the increased number of electrons.

UPS measurements were conducted to determine the electron affinity of a Si-doped $\text{Al}_{0.61}\text{Ga}_{0.39}\text{N}$ film. UPS allows one to characterize the electronic structure of the valence band in materials having a bandgap. For semiconductors, finding the high-energy turn-on (valence band maximum) and the low-energy cut-off (vacuum level) are important for determining the electron affinity of the material. This is illustrated in Fig. 3.4(a). The semiconductor electron affinity (χ_s) and work function (Φ_s) can be expressed as

$$\chi_s = h\nu - E_g - W \quad (2)$$

$$\Phi_s = h\nu - E_g - (E_F - E_v) \quad (3)$$

where $h\nu$ is the energy of the incident photons, E_g is the semiconductor bandgap energy, W is the width of the UPS spectrum, E_F is the Fermi level, and E_v is the valence band maximum. Figure 3.4(b) shows the UPS spectrum of a Si-doped $\text{Al}_{0.61}\text{Ga}_{0.49}\text{N}$ film. The value of $h\nu$ is 21.2 eV, which is the energy of the UV light from the He discharge. The value of E_g , calculated from the bandedge emission peak of the room temperature CL spectrum, is 5.1 eV. The value of W , the width of UPS spectrum, is 16.0 eV, as shown in Fig. 3.4(b). From the foregoing values, the electron affinity of the $\text{Al}_{0.61}\text{Ga}_{0.39}\text{N}$ film was calculated from Eq. (2). to be 0.1 eV

3.3.2. AlN films

It has been reported¹⁸⁻²⁰ that heavily Si-doped AlN films show improved electron emission characteristics in spite of their high resistivity. To prove or deny these claims

for our material, heavily Si-doped AlN films were grown, and the effect of this doping on electron affinity was studied. Figure 3.5(a) shows the quasi-Gaussian SIMS depth profile of the AlN reference sample containing the Si implant that was used to determine the Si concentration in the AlN films grown in this research. Figure 3.5(b) shows the Si depth profiles determined in the AlN films doped using 5 ppm and 1000 ppm SiH₄. Using the same flow rate of SiH₄, the Si concentrations achieved in the AlN films doped with these two fractions of SiH₄ were $4.5 \times 10^{18} \text{ cm}^{-3}$ and $1.0 \times 10^{21} \text{ cm}^{-3}$, respectively. The atomic density of AlN has been reported²¹ to be $4.8 \times 10^{22} \text{ cm}^{-3}$; thus, the Si concentration of $1.0 \times 10^{21} \text{ cm}^{-3}$ corresponds to the mole fraction of 2 %.

SIMS depth profiles of Si in the AlN films grown on Si- and C-terminated SiC substrates and doped using 1000 ppm SiH₄ are shown in Fig. 3.5(c). Both AlN films have almost the same Si concentration of $\sim 1 \times 10^{21} \text{ cm}^{-3}$ irrespective of their polarity.

The values of the FWHM of the AlN(0002) peak in the undoped and Si-doped films are given in Table 3.1. The FWHM of the undoped AlN film was 133 arcsec. By comparison, the FWHM in the (0002) peak acquired from the AlN films doped with $8 \times 10^{19} \text{ cm}^{-3}$ and $1 \times 10^{21} \text{ cm}^{-3}$ Si were 268 and 246 arcsec, indicating that the crystal perfection of the AlN films was degraded by heavy doping with Si.

The foregoing positive results provided impetus for complementary XPS and UPS experiments to measure the binding energy, electron affinity and work function of both the undoped and the Si-doped AlN films on the Si- and C-terminated SiC(0001) substrates. Figure 3.6(a) shows the XPS spectra of the Si doped ($1 \times 10^{21} \text{ cm}^{-3}$) Al and the N-terminated AlN films grown on the Si- and the C-terminated SiC substrates, respectively. The Al 2p core level binding energy of the N-terminated AlN film was 0.6

eV higher than that of the Al terminated film, indicating that the work function of the former is lower than that of the latter. Figure 3.6(b) is a schematic showing the relation between binding energy and work function. Since a value of zero for the binding energy is, by definition, the Fermi level,²² the difference between binding energies leads to the difference between work functions. The XPS spectra of the undoped and the heavily Si-doped AlN films are shown in Fig. 3.7. The Al 2p core level binding energy was similar for the undoped and the Si-doped AlN films, indicating that the effect of heavy Si-doping on lowering the work function is negligible.

Figures 3.8(a) and (b) show the UPS spectra of Si doped ($1 \times 10^{21} \text{ cm}^{-3}$) Al- and N-terminated AlN films on Si- and C-terminated SiC(0001) substrates, respectively. The electron affinity of the Al-terminated AlN was calculated using Eq. (2). From Fig. 4.8(a), W is 15.0 eV ($= 18.7 \text{ eV} - 3.7 \text{ eV}$), $h\nu$ is 21.2 eV, and $E_g = 6.2 \text{ eV}$ for AlN; thus, χ_s is calculated to be 0 eV ($= 21.2 \text{ eV} - 15.0 \text{ eV} - 6.2 \text{ eV}$) according to Eq.(2). The work function of the AlN films can also be calculated using this spectrum. Since the energy difference between the Fermi level, measured using a Au film on Si and confirmed using a Au film on AlN in the UPS spectra,¹⁴ and the valence band maximum is 3.2 eV ($= 21.9 \text{ eV} - 18.7 \text{ eV}$), the work function of the AlN film is calculated to be 3.0 eV ($= 21.2 \text{ eV} - 15.0 \text{ eV} - 3.2 \text{ eV}$) according to Eq.(3). In the case of the N-terminated AlN film, W is also 15.0 eV; thus, its electron affinity is also calculated to be 0 eV. The energy difference between the Fermi level and the valence band maximum is 3.7 eV ($= 21.9 \text{ eV} - 18.2 \text{ eV}$); thus, the work function is 2.5 eV ($= 21.2 \text{ eV} - 15.0 \text{ eV} - 3.7 \text{ eV}$). In summary, the electron affinities of the Al- and the N-terminated AlN films were both

zero; however, the work function of the N-terminated AlN film was 0.5 eV lower than that of the Al-terminated AlN film, which is consistent with the XPS results.

3.4 Summary

Undoped and donor doped $\text{Al}_x\text{Ga}_{1-x}\text{N}$ films having values of $x \leq 0.61$ were grown by changing the fraction of Al in the gas phase from 0.0 to 0.45. The ionized donor concentration in the n-type, Si-doped $\text{Al}_x\text{Ga}_{1-x}\text{N}$ films decreased as the mole fraction of Al was increased due to the reduction in the donor energy level and compensation. Using a SiH_4 flow rate of $1.43 \times 10^{-3} \mu\text{mol/min}$ yielded a Si concentration of about $1 \times 10^{19} \text{ cm}^{-3}$ in GaN films. The maximum mole fraction of Al in the donor doped $\text{Al}_x\text{Ga}_{1-x}\text{N}$ films for which a value of $N_D - N_A$ could be measured was ~ 0.61 . The electron affinity of a Si-doped $\text{Al}_{0.61}\text{Ga}_{0.39}\text{N}$ films was determined to be as low as 0.1 eV. Heavy doping of the AlN films with Si concentrations as high as $1 \times 10^{21} \text{ cm}^{-3}$ caused some degradation in the crystal perfection. UPS and XPS studies revealed no difference in the Al core level binding energies between undoped and heavily Si-doped AlN films. These studies also showed that the electron affinity was zero in both films and the work function of the N-terminated AlN films was 0.6 eV lower than that of the Al-terminated films.

3.5 References

1. M.C. Benjamin, M.D. Bremser, T.W. Weeks, Jr., S.W. King, R.F. Davis, and R.J. Nemanich, *Appl. Surf. Sci.* **104-105**, 455 (1996).

2. R.J. Nemanich, P.K. Baumann, M.C. Benjamin, O.-H. Nam, A.T. Sowers, B.L. Ward, H. Ade, and R.F. Davis, Appl. Surf. Sci. **130-132**, 694 (1998).
3. S.P. Grabowiski, M. Schneider, H. Niehaus, Monch, R. Dimitrov, O. Ambacher, and M. Stutzman, Appl. Phys. Lett. **78**, 2503 (2001).
4. C.W. Hartfield, and G.L. Bilbro, J. Vac. Sci. Technol. **B17**, 1970 (1999).
5. M.D. Bremser, W.G. Perry, O.-H. Nam, D.P. Griffis, R. Loesing, D.A. Ricks, and R.F. Davis, J. Electron. Mater. **27**, 229 (1998).
6. M. Ahoujja, J.L. MaFall, Y.K. Yeo, R.L. Hengehold, and J.E. Van Nostrand, Mater. Sci. Eng., **B91-92**, 285 (2002).
7. A.Y. Polyakov, N.B. Smirnov, A.V. Govorkov, M.G. Milividski, J.M. Redwing, M. Shin, M. Skowronski, D.W. Greve, and R.G. Wilson, Solid State Electron. **42**, 627 (1998).
8. Y. Taniyasu, M. Kasu, and N. Kobayashi, Appl. Phys. Lett. **81**, 1255 (2002).
9. U. Karrer, O. Ambacher, and M. Stutzmaqqn, Appl. Phys. Lett. **77**, 2012 (2000).
10. W.-C. Yang, B.J. Rodriguez, R.J. Nemanich, O. Ambacher, and V. Cimalla, J. Appl. Phys. **94**, 5720 (2003).
11. E.S. Hellman, MRS Internet J. Nitride Semicond. Res. **3**, 11 (1988).
12. F.A. Ponce, Van de Walle, and J.E. Northrup, Phys. Rev. **B 53**, 7473 (1996).
13. S. Einfeldt, Z.J. Reitmeier, and R.F. Davis, J. Cryst. Growth **253**, 129 (2003).
14. K.M. Tracy, Doctor of Philosophy Thesis, North Carolina State University, 2000.
15. M.D. McCluskey, N.M. Johnson, C.G. Van de Walle, D.P. Bour, M. Kneissl, and W. Walukiewicz, Phys. Rev. Lett. **80**, 4008 (1998).

16. S. Fischer, C. Wetzel, E.E. Haller, and B.K. Meyer, Appl. Phys. Lett. **67**, 1298 (1995).
17. C.G. Van de Walle, C. Stampfl, J. Neugebauer, M.D. McCluskey, and N.M. Johnson, MRS Internet. J. Nitride Semidcond. Res. **4S1**, G10.4 (1999).
18. M. Kasu and N. Kobayashi, Appl. Phys. Lett. **76**, 2910 (2000).
19. M. Kasu, and N. Kobayashi, Appl. Phys. Lett. **78**, 1835 (2001).
20. M. Kasu, and N. Kobayashi, Appl. Phys. Lett. **79**, 3642 (2001).
21. M. Kasu, Y. Taniyasu, and N. Kobayashi, Jpn. J. Appl. Phys. **40**, L1049 (2001).
22. J.F. Moulder, W.M.F. Stickle, P.R.E. Sobol, and K.D.H. Bomben, Handbook of X-Ray Photoelectron Spectroscopy, First ed. (Perkin Elmer, Physical Electronics Div. 1992).

Table 3.1 FWHM values of the (0002) peak acquired from undoped and Si-doped AlN films. The number of measurements acquired from each film was 10.

FWHM (arcsec)	Undoped AlN	Si-doped AlN ($8\text{E}19\text{ cm}^{-3}$)	Si-doped AlN ($1\text{E}21\text{ cm}^{-3}$)
Average	133	268	246
Std. dev.	23	32	67

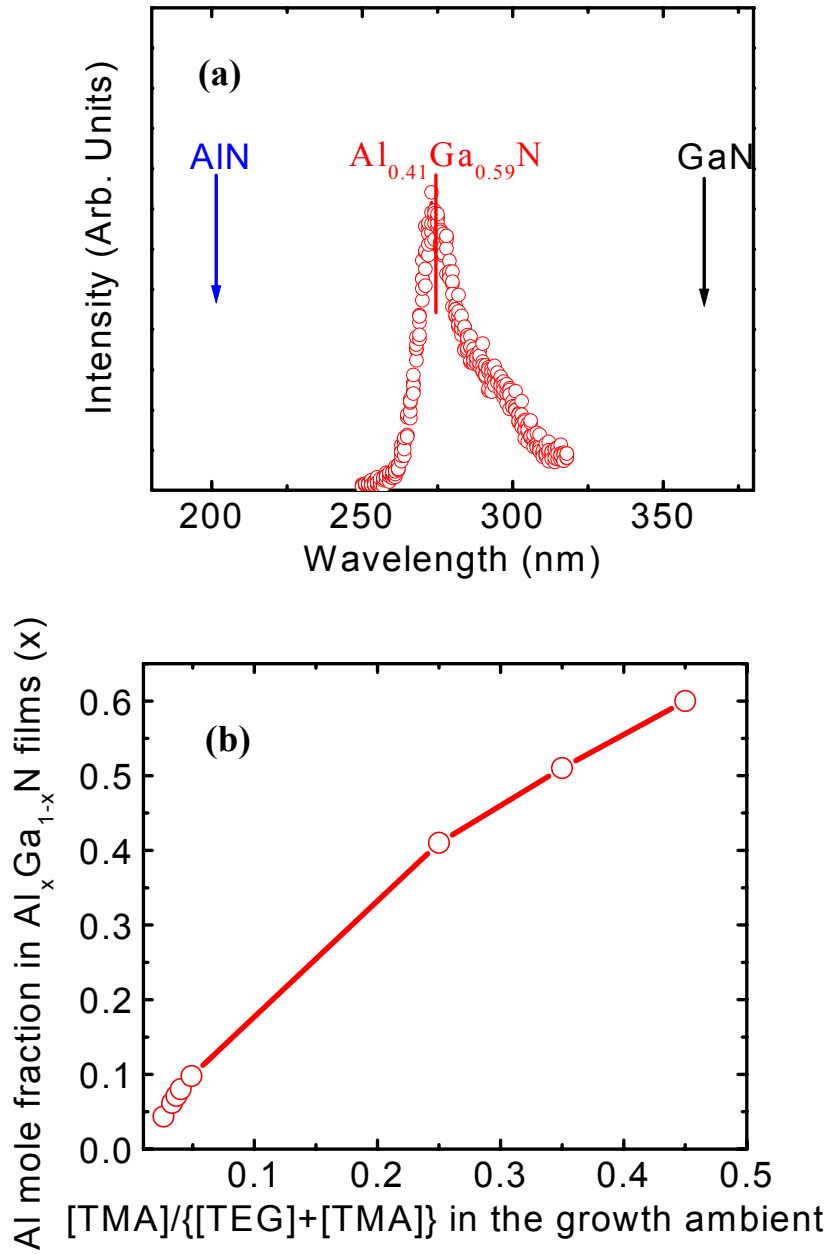


Figure 3.1 (a) Room temperature CL spectra of undoped $\text{Al}_{0.41}\text{Ga}_{0.59}\text{N}$ film and (b) Al mole fraction in $\text{Al}_x\text{Ga}_{1-x}\text{N}$ films as a function of Al source fraction in the growth ambient.

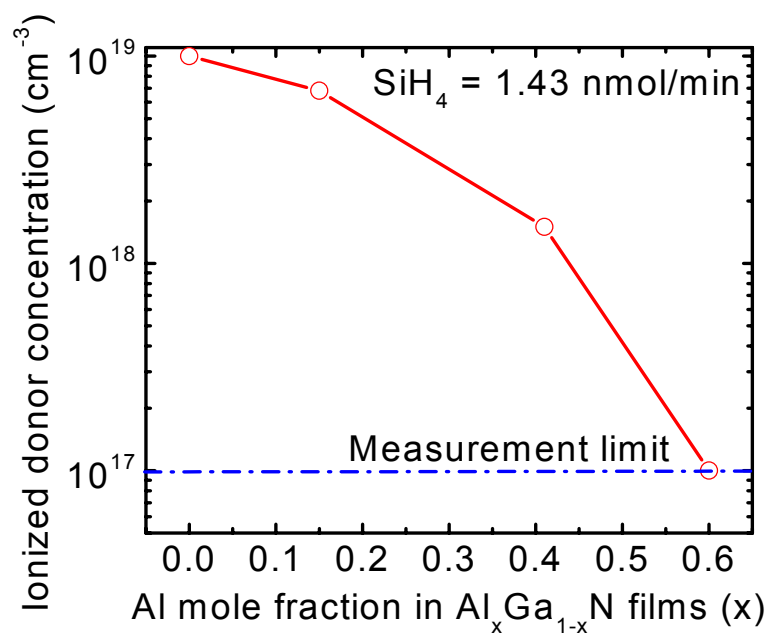


Figure 3.2 Ionized donor concentration, $N_D - N_A$, as a function of Al mole fraction in $\text{Al}_x\text{Ga}_{1-x}\text{N}$ films. The SiH_4 flow rate was held constant at 14.3 nmol/min.

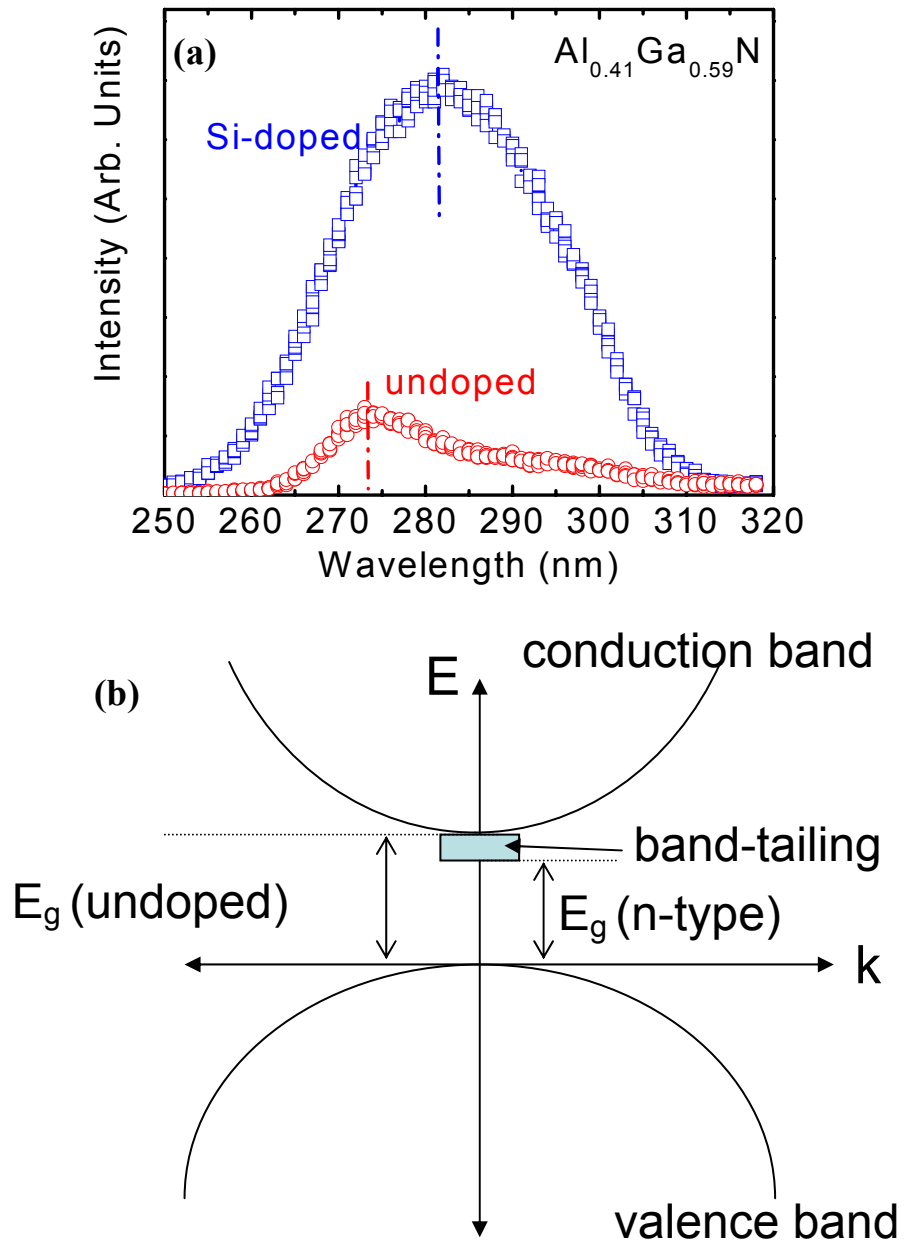


Figure 3.3 (a) Room temperature CL spectra of undoped and Si-doped $\text{Al}_{0.41}\text{Ga}_{0.59}\text{N}$ films and (b) schematic showing conduction and valence bands and their respective bandgap energies as a function of momentum of the electrons.

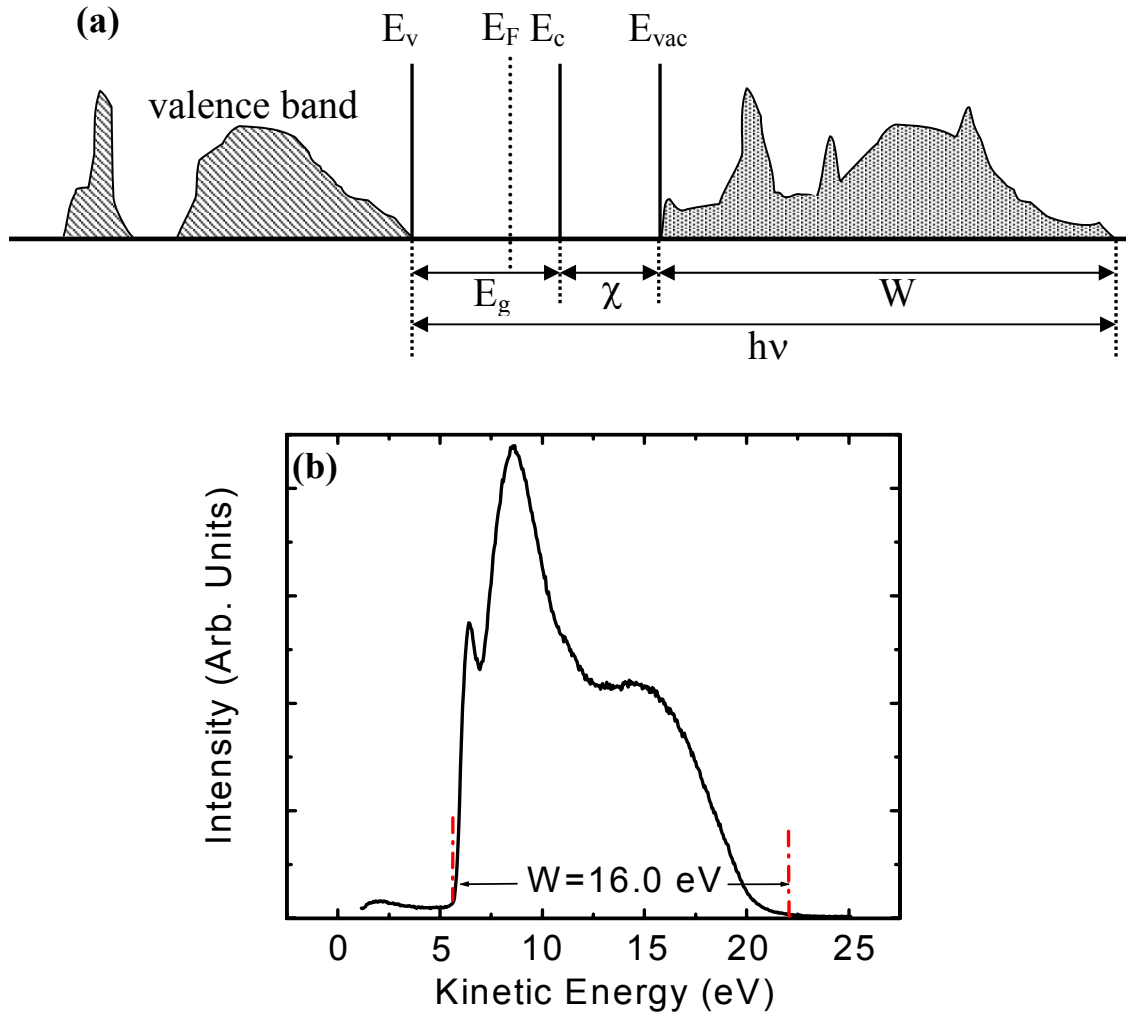


Figure 3.4 (a) Illustration of the use of various critical energies to determine the electron affinity of a semiconductor from UPS spectra and (b) the UPS spectrum of our Si-doped $Al_{0.61}Ga_{0.39}N$ film.

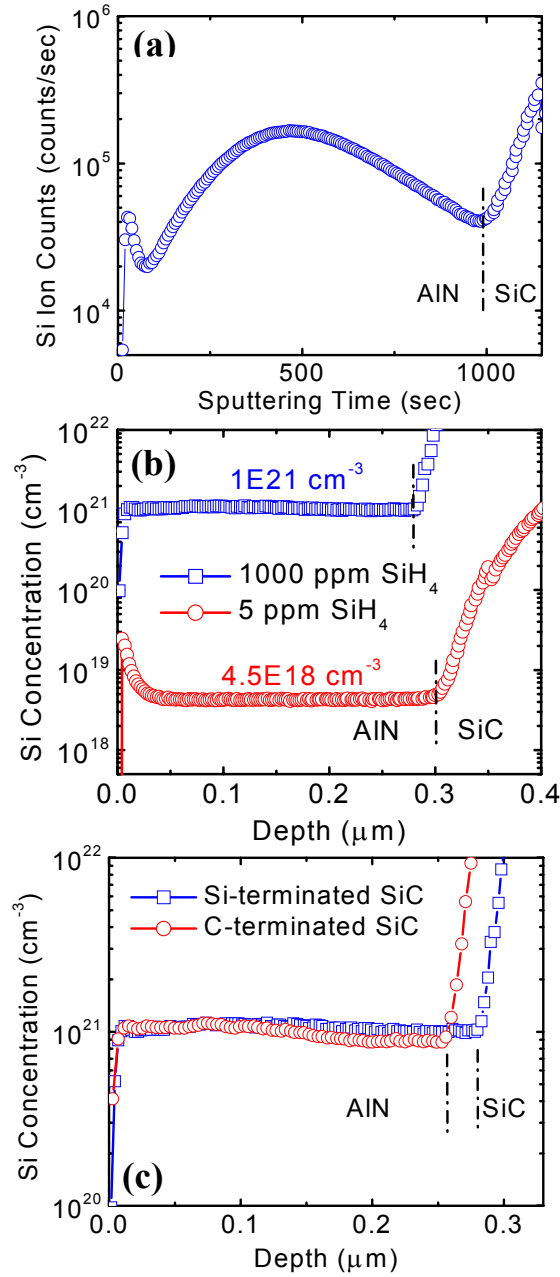


Figure 3.5 SIMS depth profiles of Si in (a) the reference AlN sample implanted with Si^+ using an energy of 90 keV and a fluence of $8 \times 10^{14} \text{ cm}^{-2}$, (b) the AlN samples doped with 5 ppm and 1000 ppm SiH_4 contained in H_2 , and (c) the AlN samples doped with 1000 ppm SiH_4 and grown on Si- and C-terminated SiC substrates.

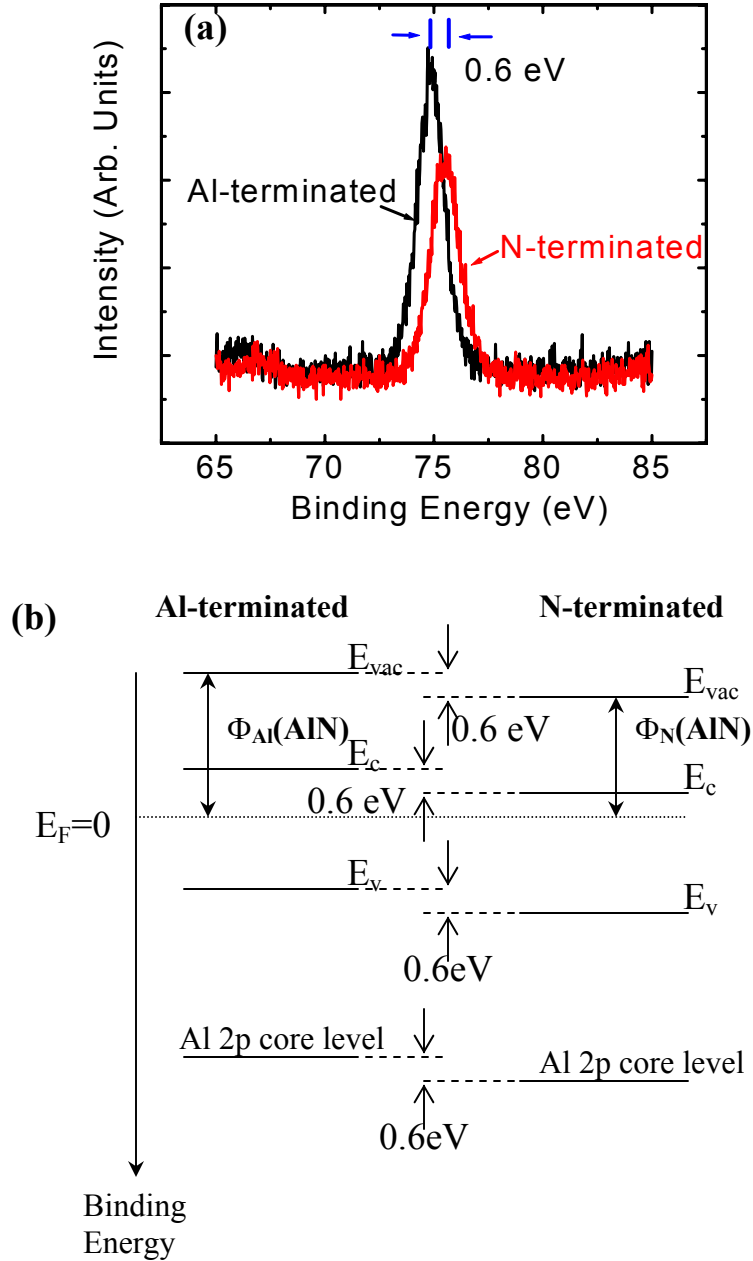


Figure 3.6 (a) XPS spectra of the Al 2p core level binding energy acquired from Si-doped ($1 \times 10^{21} \text{ cm}^{-3}$) AlN films on Si- and C-terminated SiC{0001} substrates, (b) schematic of the energy bands of Al- and N-terminated AlN showing the relation between the Al core level binding energy and the work function.

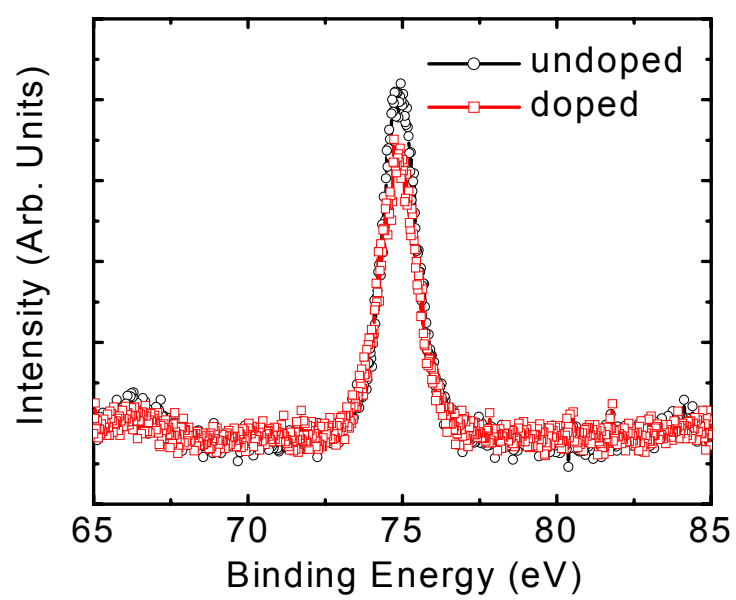


Figure 3.7 XPS spectra of undoped and Si-doped ($1 \times 10^{21} \text{ cm}^{-3}$) AlN films.

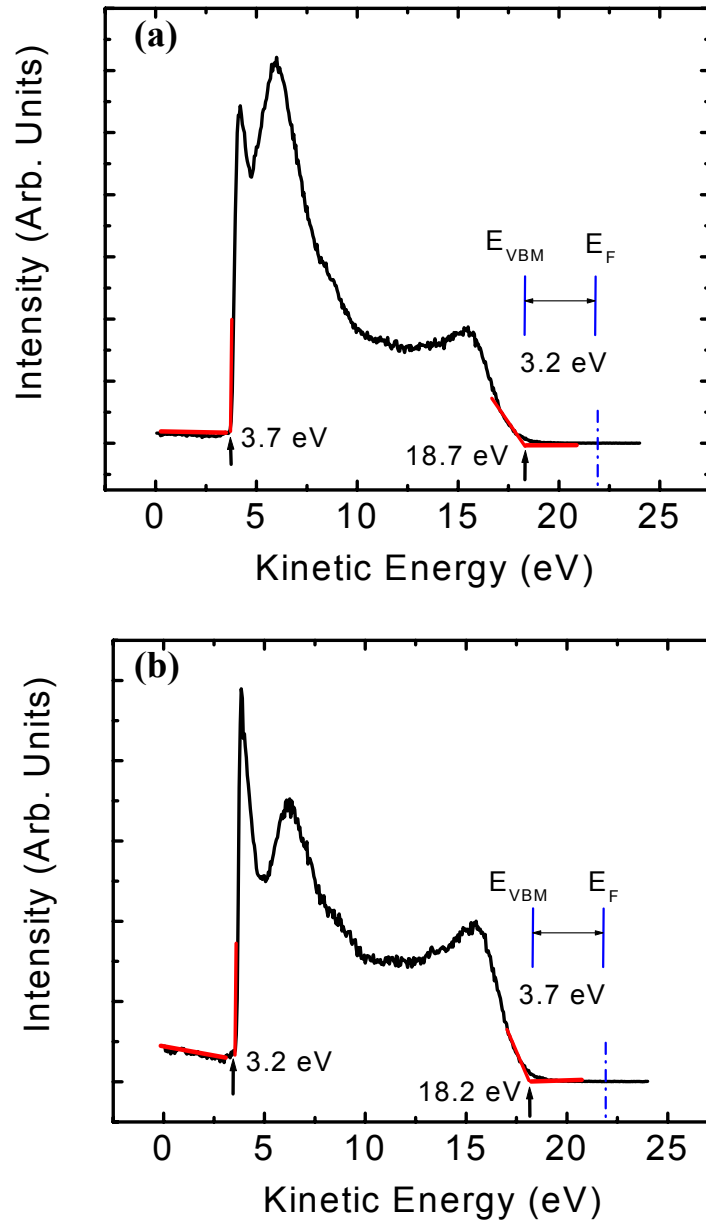


Figure 3.8 UPS spectra acquired from Si-doped ($1 \times 10^{21} \text{ cm}^{-3}$) AlN films on (a) Si-terminated and (b) C-terminated $\text{SiC}\{0001\}$ substrates.

4. Growth and Fabrication of AlGaN-based Ultraviolet Light Emitting Diodes on 6H-SiC(0001) Substrates

Ji-Soo Park, Zachary J. Reitmeier, and Robert F. Davis

Materials Science and Engineering, North Carolina State University, Raleigh, NC 27695.

Abstract

Growth, fabrication and the electrical and optical characterization of ultraviolet light emitting diodes and their components, including $\text{Al}_x\text{Ga}_{1-x}\text{N}$ films with different values of x and ohmic contacts on p-GaN films and the n-SiC(0001) substrates, and the process integration of these components have been investigated. The Al mole fraction within the $\text{Al}_x\text{Ga}_{1-x}\text{N}$ thin films was increased to a maximum value of 0.10 by changing the fraction of Al source in the growth ambient to 5%. The emission intensity of the diodes increased with an increase in the number of $\text{Al}_{0.06}\text{Ga}_{0.94}\text{N}/\text{Al}_{0.10}\text{Ga}_{0.90}\text{N}$ quantum wells. An increase in the luminescence intensity of the devices was also achieved with the use of Si-doped, rather than undoped, n-type barrier layers. Ni/Au ohmic contacts with a specific contact resistivity of $2.2 \times 10^{-4} \Omega \cdot \text{cm}^2$ were achieved on annealed, Mg-doped ($5 \times 10^{19} \text{ cm}^{-3}$), p-type GaN layers that had been cleaned in HCl at 85°C. Ni/Au ohmic contacts with a resistivity of $2.0 \times 10^{-2} \Omega \cdot \text{cm}^2$ was also formed on the backside of the SiC substrates after annealing in nitrogen. The current at 2.5V in the LEDs was 100 μA ; the total series resistance was 18.4 Ω . The peak of the primary wavelength was constant at 353 nm up to an injection current density of 0.3 kA/cm^2 . Stable luminescence was achieved to 1.4 kA/cm^2 ; only a +3 nm shift of the wavelength was observed at this current density due to the high thermal conductivity of the SiC substrates.

4.1 Introduction

Compact and efficient ultraviolet (UV) light emitting diodes (LEDs) with high output power are of considerable interest for several diverse and commercially important applications including solid-state white lighting, high-capacity data storage systems and the detection and destruction of harmful pathogens. LEDs fabricated from thin film heterostructures containing the binary compounds and the solid solutions in the GaN-AlN system are the candidates of choice for UV light sources for the aforementioned applications, because these materials possess direct bandgaps that range in energies (wavelengths) from 3.4 (360 nm in GaN) to 6.2 eV (200 nm in AlN). However, the light output power of AlGaN-based UV LEDs has been reported¹⁻⁴ to be much smaller than that obtained from InGaN-based visible LEDs.

The high density of threading dislocations present in III-nitride-based films grown on foreign substrates act as non-radiative recombination centers⁵ and have proven to have a significant impact on the output power of UV LEDs. By contrast, visible LEDs have high efficiency in spite of the high density of threading dislocations due to the presence of In-rich clusters.⁶ Growth and doping of AlGaN films with high Al concentrations are also difficult to achieve. For example when an AlGaN film is grown on a GaN template, the critical thickness for cracking, though dependent on the Al mole fraction and the quality of the GaN template, is typically lower than 100nm.⁷⁻⁹ And n-type and p-type doping efficiencies decrease with an increase in the concentration of Al¹⁰⁻¹¹ which results in a decrease in the efficiency of the injection current. AlGaN-based UV LEDs with emission at 340 and 350nm and grown and fabricated on n-type SiC(0001) substrates have been reported^{2,12} to offer advantages of vertically conducting geometry and better

thermal management, especially for dc injection currents, even though the substrate is absorbing below $\sim 360\text{nm}$.

In the present work, a vertically integrated program of research leading to the successful operation of UV LEDs fabricated from various AlGa_xN-based thin film heterostructures deposited on 6H-SiC(0001) substrates has been designed and conducted. We have investigated the growth of AlGa_xN thin films with various Al concentrations, the design and growth of quantum wells, the deposition and characteristics of ohmic contacts on p-GaN and n-SiC materials and the design of LED masks. We have also achieved the necessary process integration that has resulted in the fabrication of UV LEDs and determined the electrical and optical characteristics of these devices.

4.2 Experimental Procedures

4.2.1 Growth of $\text{Al}_x\text{Ga}_{1-x}\text{N}$ Films

On-axis, n-type 6H-SiC(0001)_{Si} wafers having a resistivity of $0.05\ \Omega\cdot\text{cm}$ were used as substrates for the growth of n- and p-type $\text{Al}_x\text{Ga}_{1-x}\text{N}$ films having AlN/GaN ratios suitable for a buffer layer atop each substrate and for the subsequently grown layers that comprised the UV LED material heterostructures. Each wafer was etched in an HF:H₂O (1:10) solution for 10 min at room temperature, rinsed in de-ionized water and blown dry with nitrogen prior to loading into the growth reactor. All films were grown via metalorganic vapor phase epitaxy (MOVPE) using a cold-walled, vertical, pancake-style system that was evacuated to 10^{-6} Torr prior to growth. Trimethylaluminum (TMA), triethylgallium (TEG), and ammonia were used as the principal precursors; five ppm SiH₄ contained in H₂ and biscyclopentadienyl-magnesium (CP₂Mg) were the sources of

the donor (Si) and the acceptor (Mg) dopants; hydrogen served as both the carrier and the diluent gas. The total pressure in the reactor and the temperature of the SiC-coated graphite heater containing the substrate were fixed at 20 Torr and 1020°C, respectively, during the growth of all layers. The temperature was measured using a single wavelength optical pyrometer.

The optimum V/III ratios that allowed the growth rate of the buffer layer and the layers that comprised the LED structure to be sufficiently small, well controlled and reproducible were determined to be 4600 and 4275, respectively; the NH₃ flow rate was fixed at 3 slm. The values of these ratios are approximately three times higher than that employed for the growth of a 1 µm-thick GaN in our MOVPE system.¹⁵ The growth rate of an Al_xGa_{1-x}N layer deposited using the V/III ratio of 4275 was ~9 nm/min.

The Al and Ga mole fractions within the Al_xGa_{1-x}N layers that comprised the LEDs were varied by changing the flow rates of both the TEG and the TMA from 31.3 to 29.8 µmol/min and from 0 to 0.03 µmol/min, respectively; the total flow rate of these precursors was maintained constant at 31.3 µmol/min. If only the flow rate of the TMA is increased, the Al composition in Al_xGa_{1-x}N layer reportedly saturates due to a gas-phase pre- (or parasitic) reaction between the NH₃ and the TMA.¹⁶⁻¹⁷

The initial studies involved the optimization of the deposition parameters for the growth of 100nm-thick, Si-doped, electrically conducting Al_{0.15}Ga_{0.85}N buffer layers on the SiC(0001) substrates.¹³ Several 300nm-thick Al_xGa_{1-x}N layers of various compositions (0≤x≤0.1) were subsequently deposited on each buffer layer and characterized. The growth temperature for both the Al_{0.15}Ga_{0.85}N and the Al_xGa_{1-x}N layers was 1020°C. The Al mole fractions of the buffer layer and the Al_xGa_{1-x}N layers

were measured using cathodoluminescence (CL) performed at room temperature using a Kimball Physics EMG-14 electron gun as the excitation source. These results indicated the flow rates of TEG and TMA to employ to achieve the desired compositions within (1) the buffer layer, (2) the cladding layers and (3) the wells and barriers that comprised the quantum well (QW) structures, as described in the following subsection.

4.2.2 Growth of the LED Heterostructures

The use of low resistivity SiC(0001) substrates allow the fabrication and operation of vertical structure LEDs containing top and bottom contacts. Thus, a mesa structure, which must be formed for the fabrication of LEDs on insulating substrates such as sapphire, does not have to be fabricated. Figure 4.1 is a cross-sectional schematic of the LED structure grown in this research. A 100nm-thick Si-doped, electrically conducting $\text{Al}_{0.15}\text{Ga}_{0.85}\text{N}$ buffer layer¹³ was initially deposited on the surface of a SiC(0001) substrate. This was followed by the growth of a 300nm-thick Si-doped $\text{Al}_{0.10}\text{Ga}_{0.90}\text{N}$ cladding layer. The value of $N_D - N_A$ in the buffer layers and in the n-type cladding layers was $5 \times 10^{18} \text{ cm}^{-3}$. Five QWs consisting of interleaving 3nm-thick undoped $\text{Al}_{0.06}\text{Ga}_{0.94}\text{N}$ wells separated by 6nm-thick, undoped or Si-doped ($N_D - N_A = 5 \times 10^{18} \text{ cm}^{-3}$) $\text{Al}_{0.10}\text{Ga}_{0.90}\text{N}$ barrier layers and a 50 nm-thick undoped- $\text{Al}_{0.10}\text{Ga}_{0.80}\text{N}$ capping layer were subsequently grown on the n-type cladding layer. Subsequent layers consisted of a 200nm-thick, p-type, Mg-doped $\text{Al}_{0.10}\text{Ga}_{0.90}\text{N}$ cladding layer followed by 50nm-thick, Mg-doped, p-type GaN ($[\text{Mg}] \sim 5 \times 10^{19} \text{ cm}^{-3}$) layer.

Ionicity in wurtzite and other non-cubic crystal structures creates internal dipoles that produce positive and negative surface charges on the crystallographic planes that are

orthogonal to the orientation of the dipoles. These surface charges, in turn, produce internal spontaneous polarization parallel to the orientation of the dipoles. The magnitude of the spontaneous polarization in AlGaIn solid solutions increases with an increase in the Al concentration.¹⁸ Piezoelectric polarization is also induced along the $\langle 0001 \rangle$ directions in heterostructures of III-nitride materials due to the in-plane stresses generated among the layers of different composition due to the mismatches in the atom-atom distances and in the coefficients of thermal expansion¹⁸. These large polarization fields deform the potential profiles of nitride-based QWs that cause a red shift in the wavelength of the emitted light. An increase in the thickness of the QW¹⁹⁻²⁰ and/or a large difference in the Al mole fraction between the well and the barrier of each QW produces changes in the polarization field that are sufficient to change the mechanism of carrier recombination from direct to spatially indirect, resulting in poor emission.²¹ As the principal objective of the research was to fabricate UV LEDs with the principal light emission having a peak wavelength of $\sim 350\text{nm}$, an $\text{Al}_{0.06}\text{Ga}_{0.94}\text{N}$ layer which has a band-edge emission at 348nm , as shown in Fig. 4.2, was used as a well. The well thickness and the Al mole fraction of the barrier were fixed at 3nm and 10% , respectively, to avoid a reduction in the probability of radiative recombination due to the large internal polarization field in the well. The thickness of barrier layer was 6nm .

The wavelength and the intensity of the radiation emitted by the quantum wells were determined via photoluminescence in tandem with a Ti:sapphire laser having the wavelength and power of 280nm and 70mW , respectively, as the excitation source.

4.2.3 Contacts on P-type GaN Films and on N-type SiC Substrates and Design of LED Mask

The samples used for the investigations concerned with ohmic contacts on p-GaN were obtained by the sequential growth of a 100 nm-thick undoped-Al_{0.15}Ga_{0.85}N buffer layer on each 6H-SiC(0001) substrate followed by a 500 nm-thick, Mg-doped GaN layer. The growth conditions were the same as those noted above. Biscyclopentadienyl-magnesium (CP₂Mg) was used as the Mg source. The desired Mg concentrations of $2 \times 10^{19} \text{ cm}^{-3}$ and $5 \times 10^{19} \text{ cm}^{-3}$ were achieved in the GaN films using flow rates of CP₂Mg of 0.04 $\mu\text{mol/min}$ or 0.1 $\mu\text{mol/min}$, respectively, as determined via secondary ion mass spectrometry. The films were subsequently annealed at 800°C for 20 min under nitrogen at atmospheric pressure to activate the Mg.

The annealed samples were cleaned either in an HCl:H₂O (1:1) solution at either room temperature or 85°C or in aqua regia (HCl:HNO₃=3:1) at room temperature for 10min. A 30nm-thick film of Ni followed and a 100nm-thick film of Au were subsequently deposited onto each p-type layer by e-beam evaporation and patterned using standard photolithography lift-off techniques. The samples were annealed at 450~550°C either for 30sec in N₂ using an AG Associates 610 rapid thermal annealing unit or for 10min in air using a conventional furnace. Transfer length method (TLM) or circular transmission line method (CTLM) test structures¹⁴ and an HP4145 Semiconductor Parameter Analyzer were used for the current-voltage (I-V) measurements. The TLM test structure consisted of 300 μm x 1500 μm rectangular pads spaced at distances between 5 and 30 μm . The specific contact resistivity, ρ_c , was determined from the I-V data acquired using the CTLM patterns. These patterns consisted of large rectangular

contacts with circular cutouts of radius R that were horizontally and vertically aligned. Circular contacts with radii, r , were placed at the center of each cutout region such that the gap spacing ($R - r$) between the concentric cutout and the contact was varied. The relationships between total resistance for the CTLM patterns and radii of patterns are given in the following equations.

$$R_t = (R_s / 2\pi) \cdot \{ \ln(R/r) + L_t \cdot (r^{-1} + R^{-1}) \} \quad (1)$$

$$L_t = (\rho_c / R_s)^{1/2} \quad (2)$$

where R_t is total resistance between internal circular contacts and external rectangular contact, R_s denotes the sheet resistance of p-GaN, and L_t is the transfer length. If the total resistance is measured for various gap spacings as a function of $\ln(R/r)$ from the straight line plot of the data for R_t and $\ln(R/r)$ from Eq.(1), the slope leads to R_s , and the intercept at $\ln(R/r) = 0$ is $R_s \cdot L_t / \pi r$ which allows the calculation of L_t . Thus, the specific contact resistivity, ρ_c , can be obtained from Eq.(2). The CTLM patterns were designed with a constant inner radius, $r = 100 \mu\text{m}$ and spacings of 15, 20, 25, 30, 40, and 50 μm .

Semi-transparent metal electrodes of sequentially deposited 4nm-thick Ni and 4nm-thick Au layers were also grown on 50nm-thick, Mg-doped, p-type GaN layers contained in the LED material structures and were annealed at 450, 500, and 550°C for 10 min in air. I-V measurements, similar to those described above, were performed to determine the optimum annealing conditions wherein the lowest specific contact resistivity was achieved.

As n-type 6H-SiC(0001) wafers were used for the substrates on which the material heterostructures that comprised the LEDs were grown, it was also necessary to develop suitable ohmic contacts to the unpolished C-terminated face of this material.

These substrates possessed a resistivity of $0.05 \Omega\cdot\text{cm}$. Layers comprised of 50 nm-thick Ni and 100 nm-thick Au were sequentially deposited via e-beam evaporation onto the backside of each SiC substrate immediately after cleaning in an $\text{HF:H}_2\text{O}$ (1:10) solution for 10 min. The metal bilayers were then patterned using standard photolithography lift-off techniques and annealed at 800°C for 20 min in either a nitrogen or a forming gas ($90\% \text{N}_2 + 10\% \text{H}_2$) ambient. The I-V characteristics and the specific resistivity were measured using CTLM test structures as described above.

Figure 4.3 (a) shows the schematic in plan-view of the mask set designed in-house and used to deposit the Au/Ni semi-transparent electrode and the Au/Ti thick electrodes on the top p-GaN contact. Figure 4.3 (b) is an illustration of the arrangement and relative thickness of these electrodes. The thickness, length and width of the semi-transparent electrode was usually $<10\text{nm}$, $390 \mu\text{m}$ and $390 \mu\text{m}$, respectively. A thick electrode for probing or wire bonding for electrical and optical measurements was subsequently formed atop the semi-transparent electrode. The sheet resistance of the latter was very high due to its small thickness; thus, the achievement of current spreading throughout its volume was very important to obtain uniform light emission. The shape of the thick electrode shown in Fig. 4.3(a) was designed to achieve efficient current spreading in the semi-transparent electrode. The area of the semi-transparent electrode that allowed transmission of light was $10.5 \times 10^{-4} \text{cm}^2$.

4.2.4 Fabrication and Electrical and Optical Characterization of the UV LEDs

Vertical LEDs were fabricated using the optimized compositions, heterostructures and process routes described in the foregoing subsections. The initial step in the

fabrication of each vertical structure LEDs consisted of the sequential deposition of a 50 nm-thick Ni layer and a 100 nm-thick Au layer on the SiC substrate. These metal layers were annealed at 800°C for 20 min in nitrogen at atmospheric pressure to obtain a backside ohmic contact and to achieve p-type character within the two Mg-containing layers. A 4nm-thick Ni layer and a 4 nm-thick Au layer were subsequently deposited on the top p-type GaN contact layer and annealed at 500 °C for 10 min in air to form a semitransparent electrode. Thick electrodes consisting of a 100nm-thick Ti layer covered by a 1000 nm-thick Au layer were deposited. All metal layers were deposited via electron beam evaporation. All contacts were patterned using standard photolithography and a lift-off process.

The electrical and optical characteristics of the LEDs were measured under direct current operation at room temperature using bare-wafer geometry. I-V measurements were performed using an HP 4145B Semiconductor Parameter Analyzer. Electroluminescence (EL) experiments were conducted using a USB2000 spectrometer (Ocean Optics, Inc). The light detector was placed ~ 5 mm from the device.

4.3 Results and Discussion

4.3.1 Optical Properties of the $Al_xGa_{1-x}N$ Films and Quantum Wells

The bandgap energies, E_g , of the $Al_xGa_{1-x}N$ layers grown in this research were determined from the values of the bandedge emission peaks acquired at room temperature via CL. The former were used to calculate the values of the Al mole fraction, x , of the $Al_xGa_{1-x}N$ layer using Eq. (3).

$$E_g(Al_xGa_{1-x}N) = x \cdot E_g(AlN) + (1-x) \cdot E_g(GaN) - b \cdot x \cdot (1-x) \quad (3)$$

where $E_g(\text{AlN})$ and $E_g(\text{GaN})$ are the bandgap energies of AlN and GaN, respectively, at room temperature. The bowing parameter, b , was assumed to be zero. Figure 4.2 shows the correspondence among the values of the wavelengths of the bandedge emission peaks, the mole fraction of Al in the $\text{Al}_x\text{Ga}_{1-x}\text{N}$ layers and the fraction of Al in the growth ambient. A perusal of this graph reveals that (1) the mole fraction of Al in the films increased linearly with an increase in the fraction of Al in the precursor gas mixture in the growth ambient and (2) increases in the mole fraction of Al to as high as 10 % could be achieved by increasing the fraction of Al in this mixture over the range from 0 to ~5%.

Figure 4.4(a) shows the PL spectra acquired from the undoped $\text{Al}_{0.06}\text{Ga}_{0.94}\text{N}$ quantum wells with Si-doped $\text{Al}_{0.10}\text{Ga}_{0.90}\text{N}$ barriers having one, three and six periods. In general, there are two peaks at ~336nm and ~357nm. The former is from the 50nm-thick $\text{Al}_{0.10}\text{Ga}_{0.90}\text{N}$ capping layer, since the position of this peak corresponds to bandedge emission from a layer having the composition of $\text{Al}_{0.10}\text{Ga}_{0.90}\text{N}$, and the peak intensity as well as the wavelength are essentially constant in the different QW structures. The peaks at ~357nm emitted by the six period MQW and the SQW had the highest and the lowest intensities, respectively, indicating that larger numbers of wells show stronger emission. The wavelength of these QW peaks was ~9nm longer than the wavelength of the peak observed in the CL spectra emitted by the thick $\text{Al}_{0.06}\text{Ga}_{0.94}\text{N}$ layer, as indicated in Fig. 4.2. The reason for this difference is not obvious; however, it may be attributed to the strong internal electric field. The optical bandgap in AlGaN QWs is narrower than that of single, thicker films of the well material due to the deformation of the well energy caused by the strong internal electric field. This effect may also be caused by a difference in the Al composition in the wells compared to that in the thick films grown

using the same parameters. The growth times for the former were as short as 20sec, the system was repeatedly switched between run and vent conditions at the end of the growth of each well and each barrier and the concentration of the TMA was repeatedly toggled in the attempt to achieve the desired compositions of the wells and barriers. As such, the flow rates of the TMA and the TEG may not be stabilized during the growth of the very thin films.

Figure 4.4(b) shows the PL spectra acquired from MQWs with undoped and Si-doped ($N_D - N_A = 5 \times 10^{18} \text{ cm}^{-3}$) barriers. The intensity of the $\sim 357\text{nm}$ peak of the latter was greater than that of the MQW with the undoped-barriers. Oh *et al.*²² have also reported that AlGaIn/GaN QWs with Si-doped barriers show enhanced emission, which they attributed to an increased density of carriers due possibly to a reduction in the density of misfit dislocations and, therefore, the density of recombination centers.²³ Nakamura *et al.*²⁴ have reported that if the Si concentration in the barrier exceeds $4.2 \times 10^{19} \text{ cm}^{-3}$, the emission efficiency is decreased due to the formation of V-shaped defects. A synthesis of the results from our studies with those reported by other investigators indicates that six period MQWs and the Si concentration (or the $N_D - N_A$ value) used in the barriers in this research are an optimum QW scheme for UV LEDs with emission in the range of 350nm.

4.3.2 P-GaN Contacts

The I-V characteristics of the Ni/Au contacts after deposition on the p-GaN layers having a Mg concentration of $2 \times 10^{19} \text{ cm}^{-3}$ and after sequential anneals under different conditions are shown in Fig. 4.5(a). The curve of the as-deposited contact exhibited the

typical asymmetric, nonlinear behavior. The curves of the annealed samples were also non-linear; however, they were symmetric due to interfacial reactions that have been reported²⁵ to occur among Ni, Au, and either GaN or GaN-containing alloys and to extend into the underlying film when annealed at the temperatures used in this research. The sample annealed in the air showed the least rectifying behavior. Prior research conducted in this laboratory by King *et al.*²⁶ determined that low contact resistivities could be achieved in a Ni/Au contact after oxidation due to the formation of p-type NiO and an amorphous Ni-Ga-O phase. These former studies also found that the contact resistance was very high when the measuring voltage was $<1\text{ V}$, indicating the presence of a contamination layer such as GaO_x on the surface of the nitride, which increased the barrier height within the Ni/p-GaN interface. The removal of the native surface contamination is reportedly²⁷ very critical for the attainment of ohmic contacts with low contact resistivity. As such, the efficacy of several methods of cleaning the nitride surface prior to metal deposition on the decrease in the resistance of these contacts was evaluated in this research.

Figure 4.5(b) reveals the I-V curves exhibited by the Ni/Au contacts deposited on similar p-GaN films after cleaning the surface of the latter in either HCl at room temperature or at 85°C or in aqua regia at room temperature. The curves of the three samples were again symmetric, however, they remained non-linear. The resistance values of the sample cleaned in the HCl solution at 85°C was much less at high voltages (i.e., $> 2\text{ V}$) than those of the sample cleaned in this solution at room temperature. The I-V characteristics of the contacts deposited on the p-GaN sample cleaned in aqua regia were slightly better than those exhibited by the contacts cleaned in the warm HCl;

however, it was subsequently determined that the photoresist employed in the metal lift-off process was damaged by the aqua regia. The integration of the results presented in Figs. 4.5 (a) and (b) revealed that the optimum processes for the achievement of the best possible behavior in the Ni/Au contacts involved the submersion of the p-GaN surface in HCl at 85°C for 10 min, drying in flowing nitrogen, the immediate insertion into the metal deposition chamber and the annealing of the contact assembly in air for 10min. These processes were used in all subsequent studies. However, as ohmic behavior could not be achieved, subsequent investigations, concerned with the effect of the Mg concentration in the p-GaN layer on the behavior of these contacts, were conducted.

Figure 4.6 shows the I-V behavior of Ni/Au contacts deposited on p-GaN layers cleaned in HCl at 85°C and containing different Mg concentrations. Linear I-V characteristics were achieved after increasing the Mg concentration from $2 \times 10^{19} \text{ cm}^{-3}$ to $5 \times 10^{19} \text{ cm}^{-3}$ and annealing the contact/GaN assembly at 450°C for 10 minutes in air. The ionization energy and the concentration of ionized Mg at room temperature in GaN have been reported to be in the range of 125 to 215 meV²⁸ and less than 1%,²⁹ respectively. As such, it is difficult to achieve tunneling through the interface barrier between a p-GaN film and a metal contact. However, the increased Mg concentration apparently results in both an increase in the concentration of holes in the GaN and a sufficiently narrow space-charge region between the Ni and the GaN such that the holes at the bottom of the top of the valence band of valence band of the latter can tunnel directly into the metal. However increasing the Mg concentration above $\sim 1 \times 10^{20} \text{ cm}^{-3}$ results in a severely degraded GaN surface and a decrease in the hole concentration.³⁰

Figure 4.7(a) shows the I-V characteristics of the optimally annealed Ni/Au contacts as a function of the gap spacing in the CTLM test patterns deposited on GaN films having the optimum Mg concentration and cleaned using the optimum annealing conditions described above. The sheet resistance of the p-GaN layer was $3 \Omega\cdot\text{cm}$. These curves exhibit typical ohmic behavior i.e., the slope decreases with an increase in the gap spacing. The values of the total resistance, R_t , calculated using the data in Fig. 4.7(a) and Eq (1), were also typical; a linear relationship was obtained in the plots of these values as a function of $\ln(R/r)$, as shown in Fig. 4.7(b). The values of the specific contact resistivity were as low as $2.2 \times 10^{-4} \Omega\cdot\text{cm}^2$.

The LED structures fabricated in this study require a semi-transparent metal electrode to be deposited on the p-GaN layer to allow the UV light generated from the quantum wells to pass into the surroundings. This was achieved via the sequential deposition of 4nm-thick Ni and 4nm-thick Au films on 50nm thick, Mg-doped GaN layers that were sequentially annealed at 450, 500, and 550°C for 10 min in air. Figure 4.8 shows the I-V curves of the contacts before and after annealing in air at 450, 500, and 550°C for 10 min. All the annealed contacts showed a lower resistance than the as-deposited contact; the contact annealed at 500°C showed the lowest resistance; this temperature and the associated annealing procedure were used in the fabrication of all the LEDs in this study. As discussed above, the formation of NiO and a Ni-Ga-O phase is very important for the attainment of a low contact resistivity; thus, Ni may be not fully oxidized below 500°C. Heating the Ni/Au contacts to a higher temperature resulted in the formation of more voids in the metal layers that caused deterioration in the contact resistivity.³¹ The contacts may also become detached from the p-GaN.³¹

4.3.3 N-SiC Contacts

Usually, ohmic contacts on n-type SiC(0001) wafers are reported³⁴ to be achieved after annealing above 900°C. The I-V characteristics of the Ni/Au contacts deposited initially on n-type SiC(0001) wafers and those annealed in various ambients at 800°C are shown in Fig. 4.9 (a). The former exhibited rectifying behavior, as revealed by the non-linear and asymmetric curves. The contact annealed in nitrogen was also rectifying; however, its resistance was much reduced compared to that of the as-deposited contact. The contact annealed in forming gas showed the lowest resistance even though it was not totally ohmic. A Ni-silicide is formed in the interface during annealing, which improves contact resistivity.³² However, the reason(s) for the improved characteristics of the contacts annealed in forming gas is not understood. The sample annealed in nitrogen after a forming gas anneal showed almost the same I-V characteristics as the sample annealed only in nitrogen, indicating that the effect of the anneal in the forming gas is lost if the sample is subsequently annealed in nitrogen.

Ni/Au electrodes were also used to connect the applied power to the Mg-doped GaN contact layer. These doped layers must be annealed at ~800°C in nitrogen to activate the Mg via decomposition of Mg-H complexes in the as-grown material.³³ To determine the effect of the forming gas anneal used to reduce the resistivity of the contacts on the n-type SiC substrates, as discussed above, on the resistivity of contacts to p-GaN, Ni/Au contacts were deposited on Mg-doped GaN samples that had been previously annealed either in nitrogen at 800°C for Mg activation or in forming gas at the same temperature after the Mg activation step. The contacts on the latter material

showed a much higher resistance than those deposited on the p-type GaN that had been annealed only in nitrogen. This indicates that a forming gas anneal at 800 °C allows one to achieve low resistivity contacts on, n-type SiC; however, the top, p-type GaN layer in the LED may begin to decompose and the resistivity of contacts to this layer may be increased.³⁵ The SiC contacts annealed in nitrogen were not perfectly ohmic, and they showed higher resistance than the sample annealed in a forming gas; however, the contact resistivity was as low as $2.0 \times 10^{-2} \Omega\text{-cm}^2$ in the CTLM test structures. Moreover, if the sample is annealed in forming gas and degradation of the p-GaN layer occurs, this will increase the series resistance of the LEDs. It is the belief of this investigator that the increase in the resistance of the contacts to n-type SiC as a result of annealing in nitrogen at 800 °C would be less than the increase in the series resistance of the LEDs after annealing in the forming gas at 800 °C. Thus, nitrogen annealing at 800 °C was chosen as the optimum conditions for annealing the ohmic contacts on SiC.

4.3.4 Electrical and Optical Characteristics of UV LEDs

Figure 4.10 (a) and (b) shows the I-V characteristics of the LEDs on linear and semi-log scales, respectively. The current at 2.5 V was 100 μA , and the total series resistance was 18.4 Ω , which is comparable to the reported values reported by other investigators^{12, 36-37} for AlGaIn-based UV LEDs with a peak wavelength of $\sim 350\text{nm}$.

The EL spectra of the LEDs were obtained at different injection currents, as shown in Figs. 4.11 (a)-(c). Different integration times were used to acquire the data shown in the three figures to avoid peak saturation. A QW peak at 353 nm as well as an associated shoulder at $\sim 370\text{nm}$ and a broad peak at $\sim 530\text{ nm}$ were observed at an

injection current of 40mA, as shown in Fig. 4.11 (a). The intensities of all the peaks increased with an increase in the injection current to 90mA; however, that of the QW peak increased more rapidly, as also shown in this figure. Further increases in the injection current caused significantly increases in the intensity of the QW peak to the extent that the intensities of the broad peak became negligible relative to the former peak, as shown in Figs. 4.11 (b) and (c). The possible origin(s) of 370nm and the 530 nm peaks will be discussed in detail in Chapter 5. These luminescence features of these devices were stable even at an injection current as high as 1400mA ($\sim 1.4 \text{ kA/cm}^2$), as shown in Fig. 4.11 (c).

Figure 4.12 shows the principal EL peak derived from the QW within the LED and acquired using injection currents within the range of 400mA to 1400mA. Figures 4.11 (a) and (b) show that the wavelength of the QW peak was essentially constant when the injection currents were in the range from 40mA to 300mA ($\sim 0.3 \text{ kA/cm}^2$). However, at injection currents $>400\text{mA}$ the wavelength shifted to slightly longer values with every increase in the current. At 1400mA, the shift in the QW peak was $\sim 3\text{nm}$ longer relative to its position at low currents. This peak shift has been reported¹⁻⁴ to be due to heating within the devices due to the high injection currents. Nishida *et al.*³⁸ have reported that a shift in the wavelength of this QW peak occurred at an injection current density as low as 0.15 kA/cm^2 in AlGaIn-based UV LEDs grown on sapphire substrates due to the insufficient thermal conductivity ($0.5 \text{ W/cm}\cdot\text{K}$) of this material. By contrast, the position in the QW peaks in the LEDs fabricated in this research was stable to 0.3kA/cm , and only a 3nm shift was observed at 1.4 kA/cm^2 . This stability in peak position is due to the

negligible heating within these LEDs as a result of the high thermal conductivity of the SiC substrates (3.4 W/cm·K).

4.4 Summary

AlGaN-based UV LEDs containing five sets of $\text{Al}_{0.06}\text{Ga}_{0.94}\text{N}/\text{Al}_{0.10}\text{Ga}_{0.90}\text{N}$ QWs that emitted the principal radiation at the wavelength of 353 nm have been grown and fabricated on 6H-SiC(0001) substrates. The Al mole fraction in the $\text{Al}_x\text{Ga}_{1-x}\text{N}$ thin films in the LED material structures was varied between 0% and 10% by increasing the fraction of Al in the growth ambient to 5%. The intensity of the QW peak increased with an increase in the number of QWs. The introduction of Si into the barrier layers resulted in a marked increase in the luminescence relative to that emitted when undoped barriers were used. Ni/Au contacts deposited on the top, p-GaN layer having a Mg concentration of $5 \times 10^{19} \text{ cm}^{-3}$ and previously cleaned in HCl at 85 °C possessed a specific contact resistivity of $2.2 \times 10^{-4} \Omega \cdot \text{cm}^2$ after annealing in air at 450 °C for 10 min. Ni/Au contacts were also formed on the backside of the SiC substrates. These latter contacts possessed a contact resistivity of $2.0 \times 10^{-2} \Omega \cdot \text{cm}^2$ after annealing in nitrogen at 800 °C for 10 min. The current in the LEDs was 100 μA at a voltage of 2.5V. The total series resistance in these devices was 18.4 Ω . They exhibited stable luminescence at injection current densities as high as 1.4 kA/cm^2 . The peak of the QW emission was constant to current densities as high as 0.3 kA/cm^2 . Only a +3 nm shift in the wavelength occurred at 1.4 kA/cm^2 as a result of heating within the device. This very small shift is attributed to the high thermal conductivity of the SiC substrates.

4.5 References

1. T. Nishida, H. Saito, and N. Kobayashi, App. Phys. Lett. **78**, 3927 (2001).
2. V. Adivarahan, A. Chitnis, J.P. Jhang, L.W. Yang, G. Simin, A.A. Khan, R. Gaska, and M.S. Shur, Appl. Phys. Lett. **79**, 4240 (2001).
3. A. Kinoshita, H. Hirayama, M. Ainoya, Y. Aoyagi, and A. Hirata: Appl. Phys. Lett., **77**, 175 (2000).
4. M.A Sanchez-Garcia, F.B. Naranjo, J.L. Pau, A. Jimenez, E. Calleja and E. Munoz, J. Appl. Phys., **87** 1569 (2000).
5. T. Sugahara, M. Hao, T. Wang, D. Nakagawa, Y. Naoi, K. Nishino, and S. Sakai, Jpn. J. Appl. Phys. **37**, L1195 (1998).
6. T. Mukai, and S. Nakamura, Jpn. J. Appl. Phys. **38**, 5735 (1999).
7. K. Itoh, K. Hiramatsu, H. Amano, and I. Akasaki, J. Cryst. Growth **104**, 533 (1990).
8. S.J. Hearne, J. Han, S.R. Lee, J.A. Floro, D.M. Follstaedt, E. Chason, and I.S.T. Tsong, Appl. Phys. Lett. **76**, 1534 (2000).
9. S. Einfeldt, V. Kirchner, H. Heinke, M. DieBelberg, S. Figge, K. Vogeler, and D. Hummel, J. Appl. Phys. **88**, 7029 (2000).
10. M. Suzuki, J. Nishio, M. Onomura, and C. Hongo, J. Cryst. Growth **189/190**, 511 (1998).
11. A.Y. Polyakov, N.B. Smirnov, A.V. Govorkov, M.G. Milividskii, J.M. Redwing, M. Shin, M. Skowronski, D.W. Greve, and R.G. Wilson, Solid State Electronics **42**, 627 (1998).
12. T. Nishida, H. Saito, and N. Kobayashi, Appl. Phys. Lett. **78**, 399 (2001).
13. S. Einfeldt, Z.J. Reitmeier, and R.F. Davis, J. Cryst. Growth **253**, 129 (2003).

14. D.K. Schroder, Semiconductor Material and Device Characterization, (John Wiley and Sons, Inc., New York, 1998), p.156.
15. A.M. Roskowski, P.Q. Miraglia, E.A. Preble, S. Einfeldt, and R.F. Davis, J. Cryst. Growth **241**, 141 (2002).
16. J. Han, J.J. Figiel, M.H. Crawford, M.A. Banas, M.E. Bartram, R.M. Biefeld, Y.K. Song, and A.V. Nurmikko, J. Cryst. Growth **195**, 291 (1998).
17. S.C. Choi, J.-H. Kim, J.Y. Choi, K.L. Lee, K.Y. Lim, and G.M. Yang, J. Appl. Phys., **87**, 172 (2000).
18. F. A. Ponce and D. P. Bour, Nature **386**, 351 (1997).
19. S. Chichibu, T. Azuhara, T. Sota, and S. Nakamura, Appl. Phys. Lett. **70**, 2822 (1997).
20. F. Bernardi, V. Fiorentini, and D. Vanderbilt, Phys. Rev. B **56**, R10024 (1997).
21. T. Deguchi, K. Sekiguchi, A. Nakamura, T. Sota, R. Matsuo, S. Chichibu, and S. Nakamura, Jpn. J. Appl. Phys. **38**, L914 (1999).
22. E. Oh, C. Sone, O. Nam, H. Park, and Y. Park, Appl. Phys. Lett. **76**, 3242 (2000).
23. K. C. Zeng, J. Y. Lin, A. Salvador, G. Popovici, H. Tang, W. Kim, and H. Morkoc, Appl. Phys. Lett., **71**, 1368 (1997).
24. T. Nakamura, S. Mochizuki, S. Terao, T. Sano, M. Iwaya, S. Satoshi, H. Amano, and I. Akasaki, J. Cryst. Growth **237-239**, 1129 (2002).
25. J.K. Shue, Y.K. Su, G.C. Chi, W.C. Chen, C.Y. Chen, C.N. Huang, J.M. Hong, Y.C. Yu, C.W. Wang, and E.K. Lin, J. Appl. Phys. **83**, 3172 (1998).
26. S.W. King, J.P. Barnak, M.D. Bremser, K.M. Tracy, C. Ronning, R.F. Davis, and R.J. Nemanich, J. Appl. Phys. **84**, 5248 (1998).

27. P.J. Hartlieb, A. Roskowski, and R.F. Davis, J. Appl. Phys. **91**, 9151 (2002).
28. P. Kozodoy, H. Xing, S.P. DenBarrs, and U.K. Mishra, A. Saxler, R. Perrin, S. Elhamri, and W.C. Mitchel, J. Appl. Phys. **87**, 1832 (2000).
29. S. Nakamura, M. Senoh, and T. Mukai, Jpn. J. Appl. Phys. **30**, L1708 (1991).
30. I.P. Smorchkova, E. Haus, B. Heying, P. Kozodoy, P. Fini, J.P. Ibbetson, S. Keller, S.P. DenBaars, J.S. Speck, and U.K. Mishra, Appl. Phys. Lett. **76**, 718 (2000).
31. J.K. Ho, C.S. Jong, C.C. Hiu, C.N. Huang, K.K. Shih, L.C. Chen, F. R. Chen, J.J. Kai, J. Appl. Phys. **86**, 4491 (1999).
32. J. Crofton, L.M. Porter, and J.R. Williams, Phys. Status Solidi (b) **202**, 581 (1997).
33. W. Gotz, N.M. Johnson, J. Walker, D.P. Bour, H. Amano, and I. Akasaki, Appl. Phys. Lett. **67**, 2666 (1995).
34. M.W. Cole, P.C. Joshi, C.W. Hubbard, M.C. Wood, M.H. Ervin, B. Geil and F. Ren, J. Appl. Phys. **88**, 2652 (2000).
35. D.D Koleske, A.E. Wickenden, R.L. Henry, J.C. Culbertson, and M.E. Twigg, J. Cryst. Growth **223**, 466 (2001).
36. K. Akita, T. Nakamura, and H. Hirayama, Phys. Status Solidi (a) **201**, 2624 (2004).
37. H. Hirayama, K. Akita, T. Kyono and T. Nakamura, Phys. Status Solidi (a) **201**, 2639 (2004).
38. T. Nishida, T. Ban, and N. Kobayashi, Appl. Phys. Lett. **81**, 1 (2003).

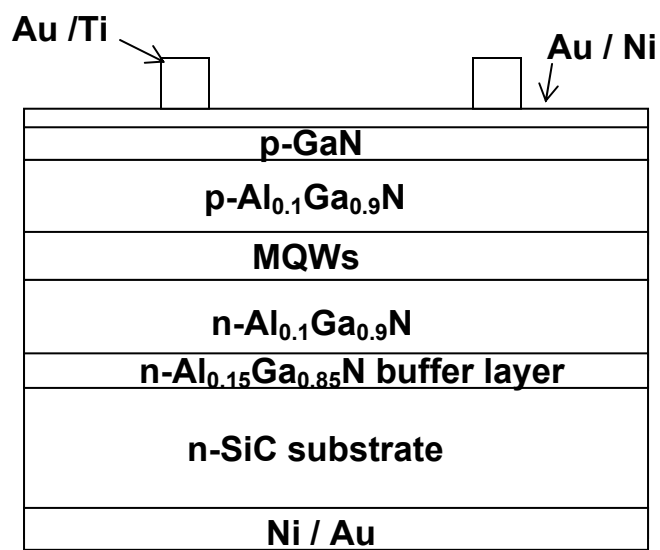


Figure 4.1 Cross-sectional schematic of the LED structure

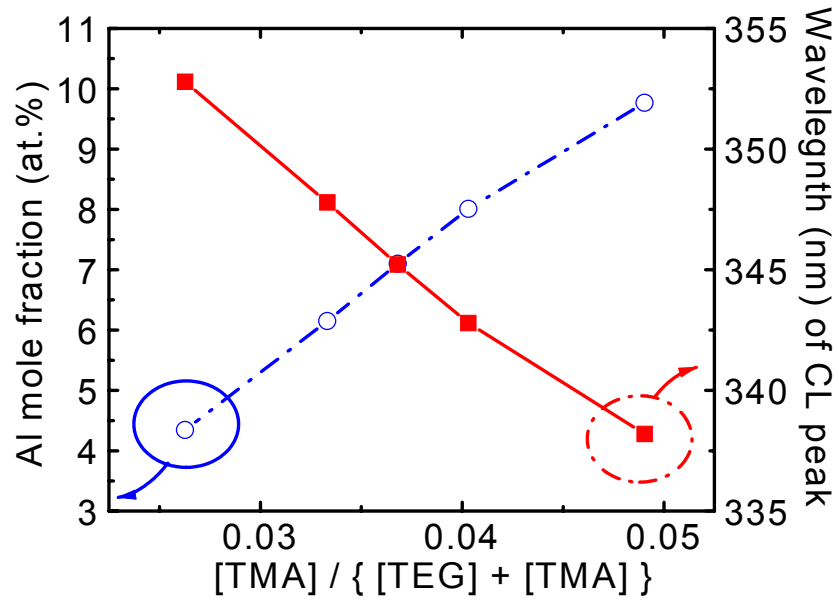


Figure 4.2 Al mole fraction in the $\text{Al}_x\text{Ga}_{1-x}\text{N}$ films and the wavelength of the bandedge emission peak determined via CL as a function of the fraction of Al in the growth ambient.

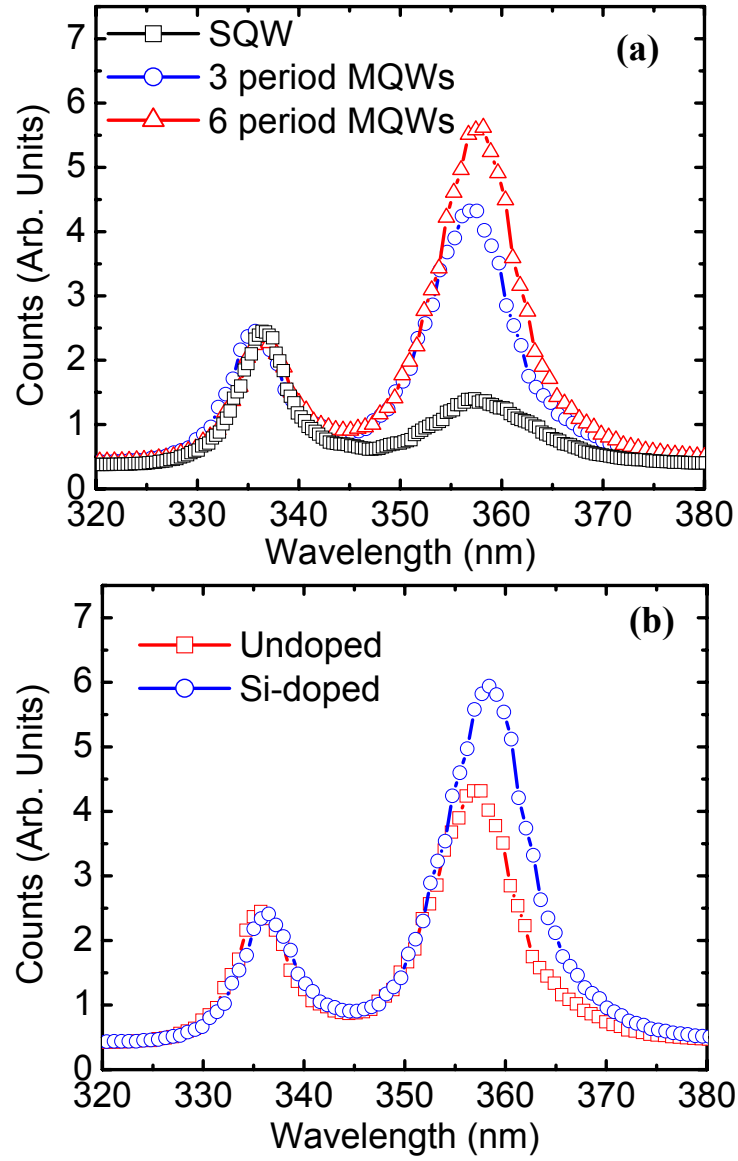


Figure 4.4 PL spectra acquired from (a) one, three and six period quantum wells with undoped barriers and (b) three period quantum wells with undoped and Si-doped ($N_D - N_A = 5 \times 10^{18} \text{ cm}^{-3}$) barriers.

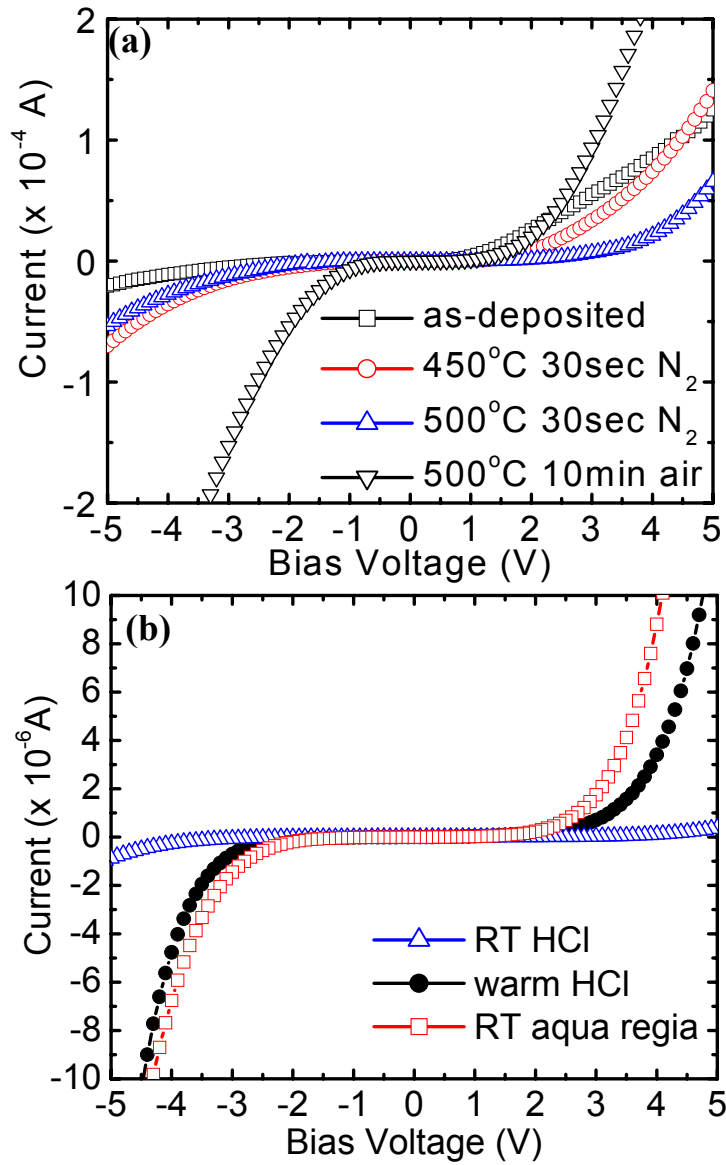


Figure 4.5 I-V characteristics of Ni/Au contacts on p-GaN having a Mg concentration of $2 \times 10^{19} \text{ cm}^{-3}$ (a) as-deposited and sequentially annealed at 450 °C or 500 °C for 30 sec in nitrogen or 500 °C for 10min in air, and (b) after cleaning the GaN surface in either HCl at room temperature or at 85 °C or in aqua regia at room temperature prior to metal deposition. The contacts were annealed at 550 °C for 10 min in air. The contact spacing within the TLM patterns was (a) 10 μm and (b) 30 μm .

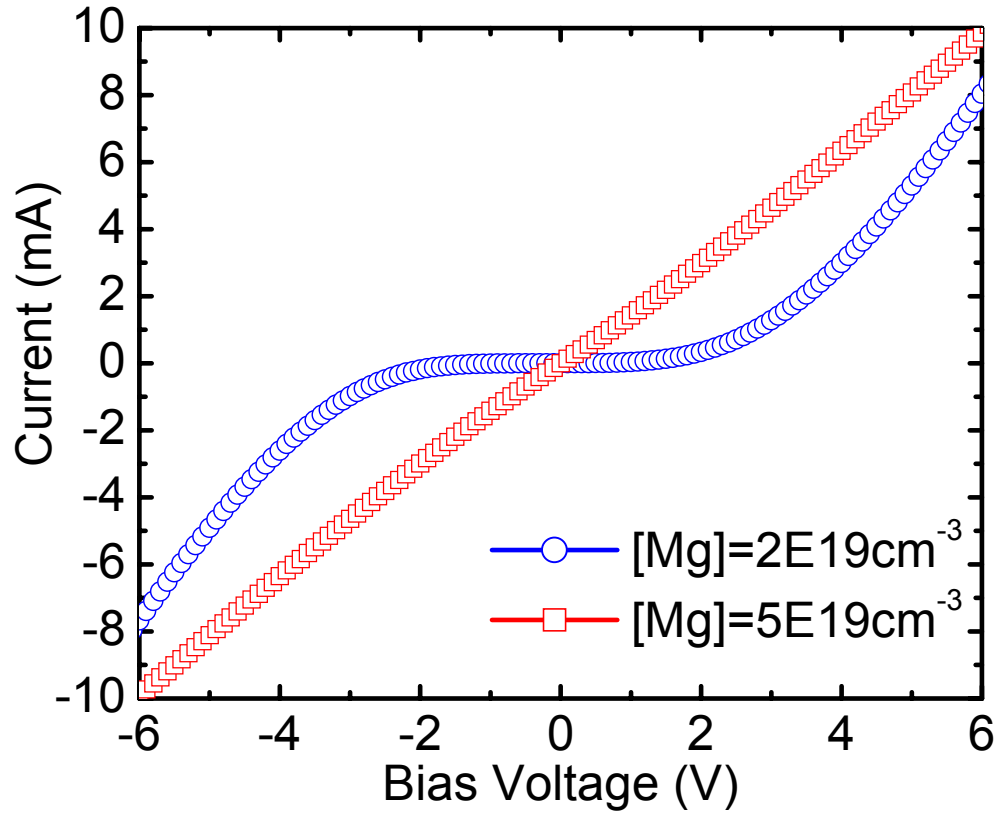


Figure 4.6 I-V characteristics of Ni/Au contacts on p-GaN films with Mg concentrations of $2 \times 10^{19} \text{ cm}^{-3}$ and $5 \times 10^{19} \text{ cm}^{-3}$. The surface of each film was cleaned using an HCl solution at 85 °C. The film/contact assemblies were annealed in air at 450 °C for 10 min. The contact spacing in the CTLM patterns was 15 μm .

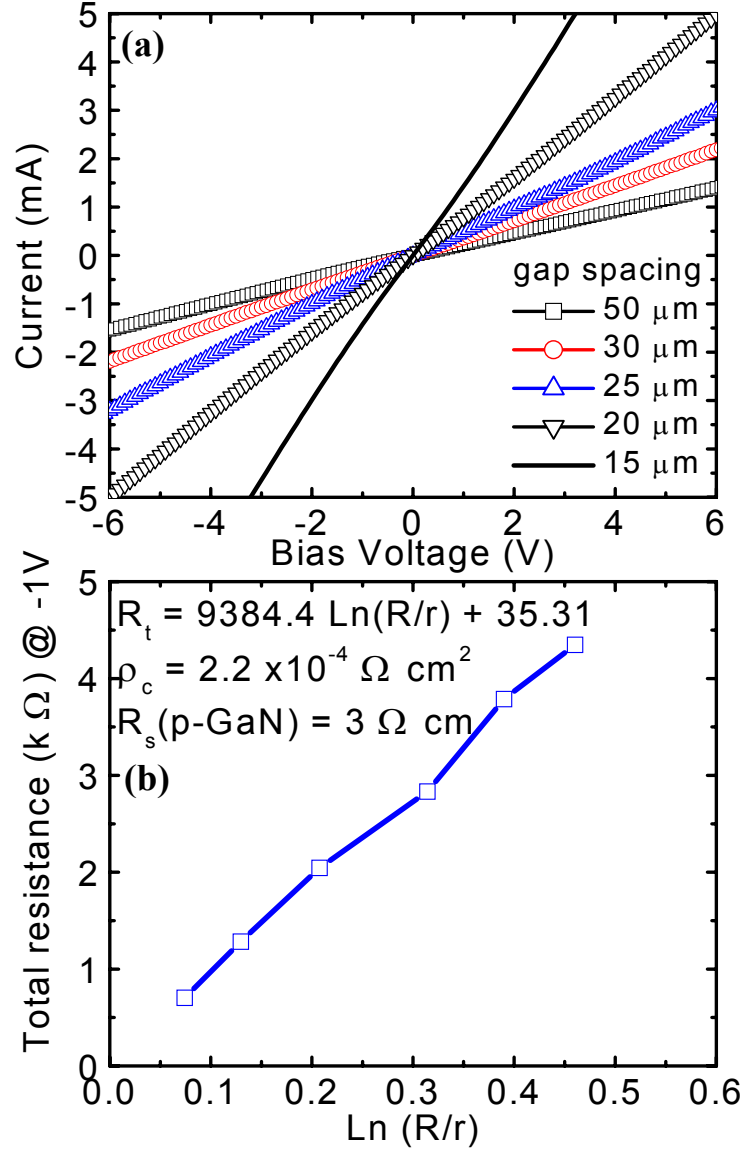


Figure 4.7 (a) Current-voltage (I-V) characteristics of annealed Ni/Au contacts deposited on cleaned p-GaN containing $5 \times 10^{19} \text{ cm}^{-3}$ Mg as a function of the contact spacing of the CTLM pattern and (b) total resistance (R_t) as a function of $\ln(R/r)$, where R and r denote the radii of the circular cutouts and the circular contacts inside the circular cutouts, respectively.

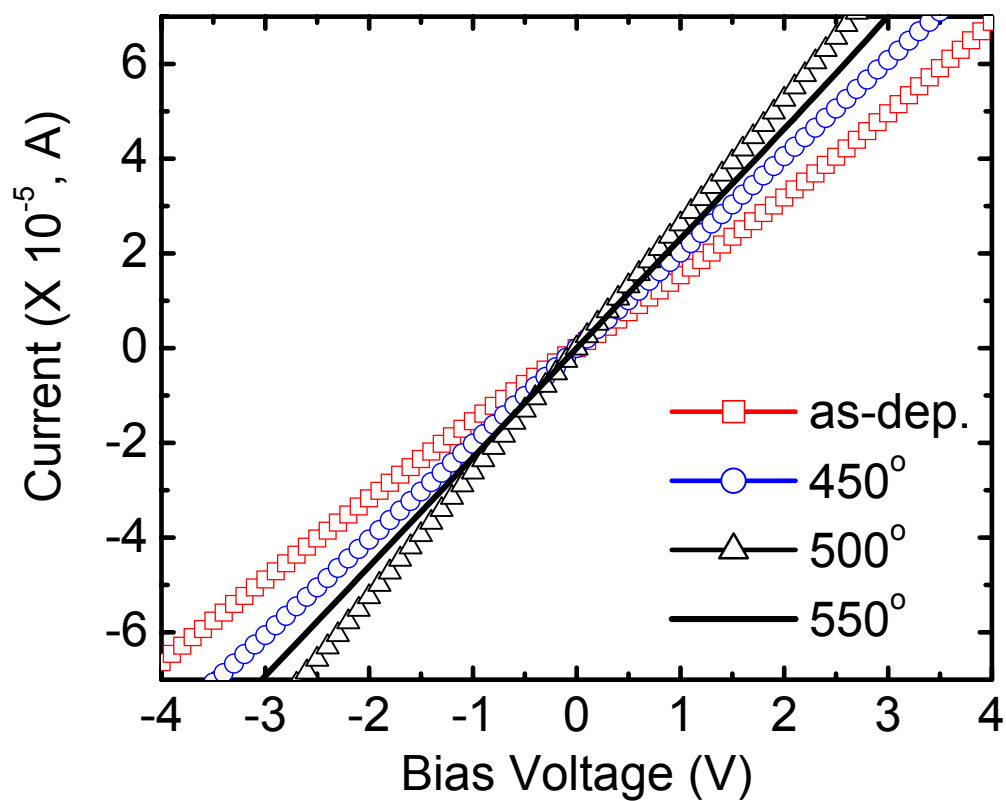


Figure 4.8 Current-voltage (I-V) characteristics of semi-transparent electrode (4nm-thick Ni and 4nm-thick Au) as-deposited and sequentially annealed at different temperatures in air for 10 min.

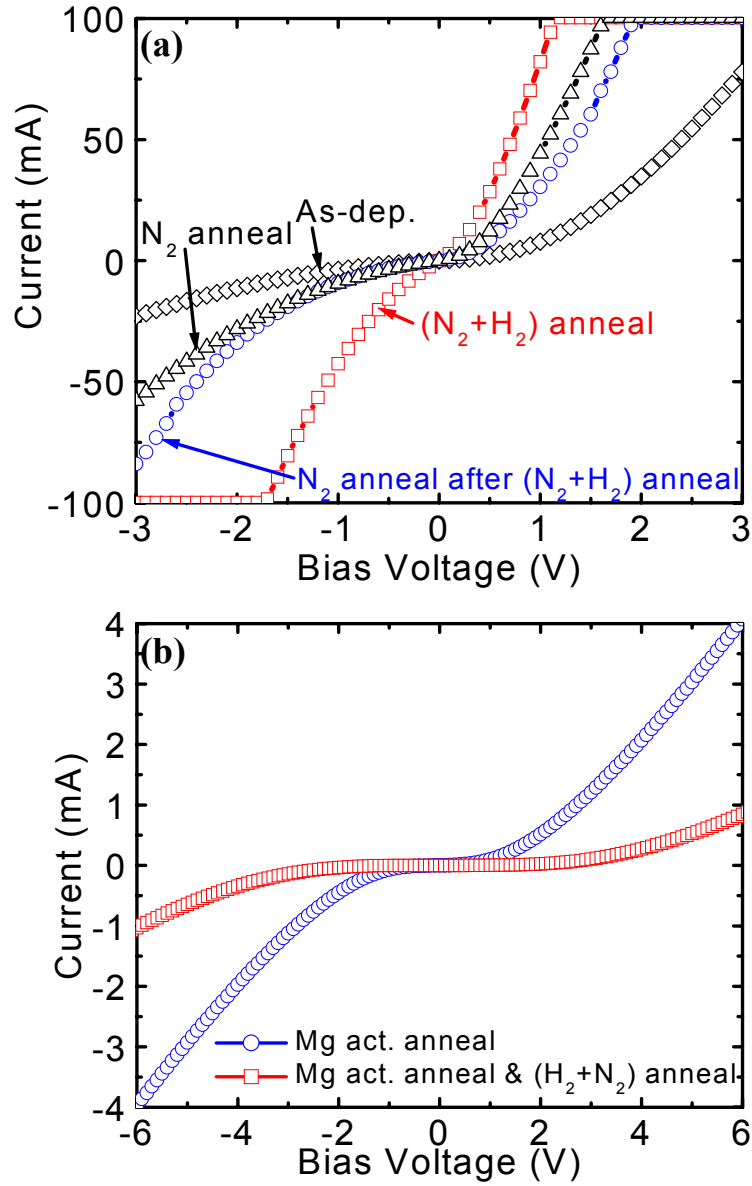


Figure 4.9 Current-voltage (I-V) characteristics of Ni/Au contacts deposited on (a) n-type SiC(0001) wafers and annealed at 800°C under different conditions and (b) Mg-doped GaN films annealed either in nitrogen alone for Mg activation or in forming gas following the Mg activation anneal. The contact spacing of CTLM patterns was 15 μm .

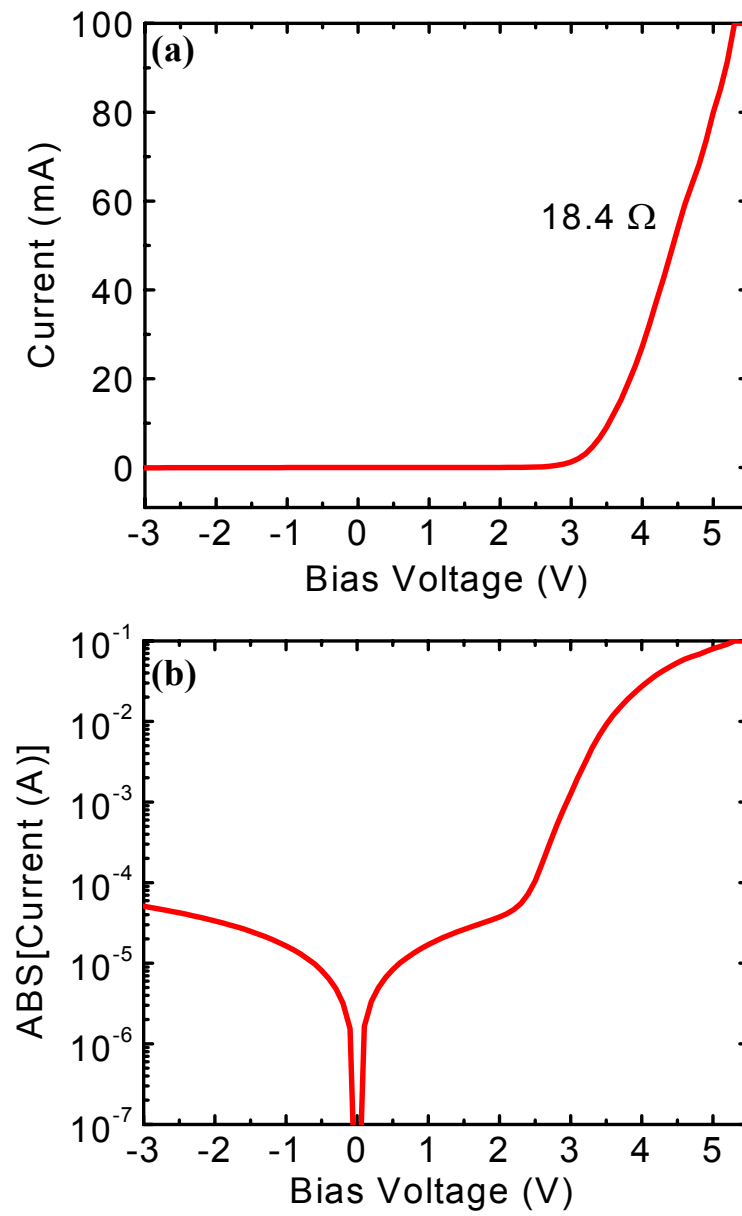


Figure 4.10 Current-voltage (I-V) characteristics of the LEDs on (a) linear and (b) semi-log scales.

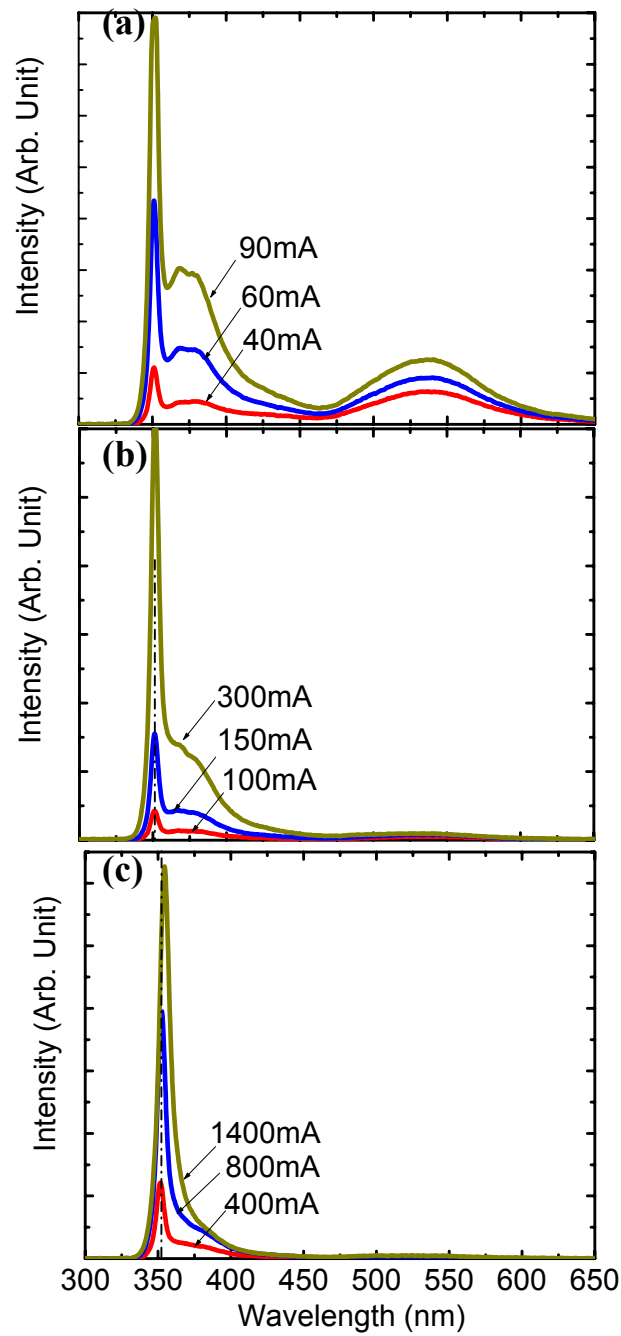


Figure 4.11 EL spectra of LED acquired using a (a) low injection current (40~90mA), (b) high injection current (100~300mA) and (c) very high injection current (400~1400mA). A different integration time was used in each case to avoid peak saturation.

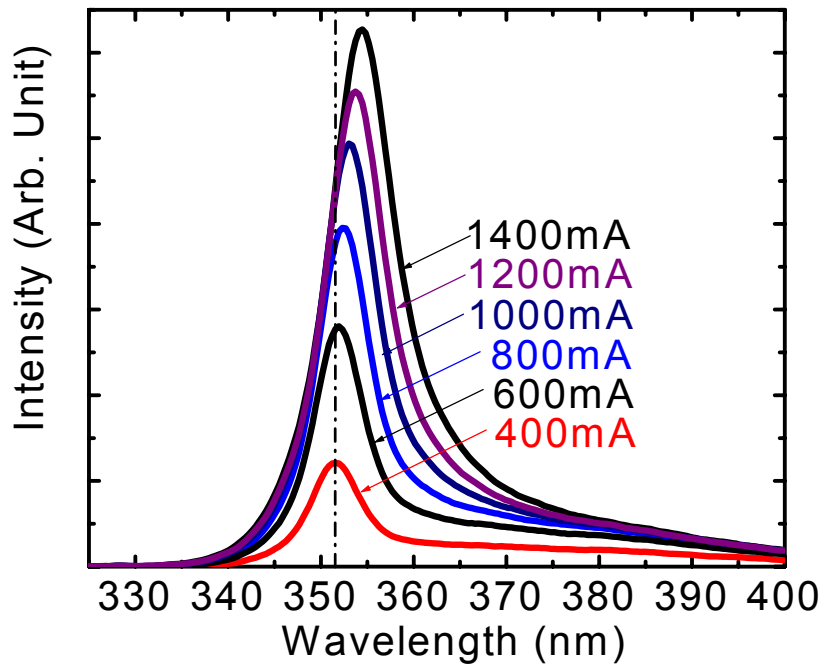


Figure 4.12 EL spectra of LED at very high injection current (400~1400mA).

5. Effect of Carrier-Blocking Layers on the Emission Characteristics of AlGaIn-based Ultraviolet Light Emitting Diodes

Ji-Soo Park, Daryl Fothergill¹, Xiyao Zhang¹, Zachary J. Reitmeier, John. F. Muth¹, and Robert F. Davis

Department of Materials Science and Engineering, North Carolina State University, Raleigh, NC 27695-7907

¹Department of Electrical and Computer Engineering, North Carolina State University, Raleigh, NC 27695-7911

Abstract

AlGaIn-based thin film heterostructures suitable for ultraviolet light emitting diodes have been grown and fabricated into working devices with and without p-type and n-type AlGaIn carrier-blocking layers at the top and the bottom of the quantum wells, respectively. The principal emission from each device occurred at 353nm. The highest intensities of this peak were measured at all values of the injection current in the device with a p-type carrier-blocking layer at the top of the quantum well; this device also exhibited the highest values of light output power. Growth of an n-type carrier-blocking layer at the bottom of the quantum wells had an adverse effect on the characteristics of light emitting diodes. A broad peak centered at ~540nm exhibited yellow luminescence and was present in the spectra acquired from all the devices. This peak is attributed to absorption of the ultraviolet emission by and re-emission from the p-GaN and/or to the luminescence from the AlGaIn within quantum wells by current injection. The intensity of this peak increased and saturated by the same order of magnitude as the intensity of the emission at 353nm.

5.1 Introduction

Considerable research has been conducted on the growth of III-nitride-based material heterostructures and the fabrication of high-power ultraviolet (UV) light emitting diodes (LEDs), with wavelengths below 360nm for application in long life-time white lighting, high-density optical storage and biochemical and medical applications.²⁻¹⁰⁾ Domen *et al.*¹⁾ have reported that electron overflow from the active region into a p-type cladding layer can be a significant problem in III-nitride-based UV LEDs, because of poor hole injection and low hole mobility. Electrons that overflow from the active regions into the p-type cladding layers are typically lost to either radiative recombination with the majority holes or non-radiative recombination at point or extend defects. These processes reduce both the power and the efficiency of UV LEDs.

Subsequent studies have shown that the introduction of a carrier blocking layer (CBL) markedly improves output power²⁾ and significantly reduces parasitic emissions³⁾ in AlGaInN-based UV LEDs. The majority of the AlGaInN- or AlGaInN-based UV LEDs have had either a p-type AlGaIn CBL atop the quantum well (QW)⁴⁻⁶⁾ or both a p-type and an n-type AlGaIn CBL at the top and the bottom, respectively, of the QW^{2,7-10)}.

In this paper, we conducted a systematic study that compared the efficacy of growing (1) separate p-type and n-type CBLs at the top and bottom, respectively, of III-nitride-based QWs and (2) both of these CBLs in the same material structure. AlGaIn-based material heterostructures, suitable for UV LEDs, with and without p-type and n-type AlGaIn CBLs at the top and the bottom, respectively, of the QWs and with emissions at 353nm were grown on SiC(0001) substrates containing a previously

deposited conducting $\text{Al}_{0.15}\text{Ga}_{0.85}\text{N}$ buffer layer. The effects of each CBL on the intensities of the UV and the visible emissions and on the light output power of the subsequently fabricated UV LEDs were investigated.

5.2 Experimental Procedures

The LED material structures were grown by metalorganic vapor phase epitaxy (MOVPE) using a cold-walled vertical pancake-style system that was evacuated to 10^{-6} Torr prior to growth. The on-axis, n-type 6H-SiC(0001)_{Si} substrates were etched in an HF:H₂O (1:10) solution for 10 min at room temperature, rinsed in de-ionized water and blown dry with nitrogen prior to loading into the growth reactor. The resistivity of these substrates was $\sim 0.05 \Omega\cdot\text{cm}$. Trimethylaluminum (TMA), triethylgallium (TEG), and ammonia were used as the precursors; hydrogen served as both the carrier and the diluent gas. The reactor pressure was fixed at 20 Torr for the growth of all layers in the LED structures. The temperature of the SiC-coated graphite susceptor was measured using a single wavelength optical pyrometer.

Figure 5.1 is a cross-sectional schematic of the primary LED structure without a CBL. A 100nm-thick Si-doped, electrically conducting $\text{Al}_{0.15}\text{Ga}_{0.85}\text{N}$ buffer layer¹¹⁾ was deposited on the surface of each SiC(0001) substrate as the initial growth step in the fabrication of each multi-layer heterostructure. This was followed by the growth of a 1000nm-thick Si-doped $\text{Al}_{0.10}\text{Ga}_{0.90}\text{N}$ cladding layer. The value of $N_D - N_A$ measured by capacitance-voltage measurement in the buffer layers and in the n-type cladding layers was $5 \times 10^{18} \text{cm}^{-3}$.

In structures without an n-type CBL, five QWs consisting of 3nm-thick undoped $\text{Al}_{0.06}\text{Ga}_{0.94}\text{N}$ wells separated by 6nm-thick, Si-doped ($[\text{Si}] \sim 5 \times 10^{18} \text{ cm}^{-3}$) $\text{Al}_{0.10}\text{Ga}_{0.90}\text{N}$ barrier layers were subsequently grown on the n-type cladding layer. Subsequent layers consisted of a 200nm-thick, p-type, Mg-doped $\text{Al}_{0.10}\text{Ga}_{0.90}\text{N}$ cladding layer followed by 50nm-thick, Mg-doped, p-type GaN ($[\text{Mg}] \sim 5 \times 10^{19} \text{ cm}^{-3}$) layer. The only difference in the conditions used to grow these layers was the V/III ratio. The values of which were 4600 for the buffer layers, and 4275 for the cladding layers, and the quantum wells. The schematic in Figure 5.2 (a) shows the mole fraction of Al in each layer and the relative position of each of the different types of layers for the structure described above. A 20nm-thick, Mg-doped ($[\text{Mg}] \sim 5 \times 10^{19} \text{ cm}^{-3}$) p-type $\text{Al}_{0.25}\text{Ga}_{0.75}\text{N}$ CBL (P-CBL) was initially inserted between the QWs and the Mg-doped $\text{Al}_{0.10}\text{Ga}_{0.90}\text{N}$ cladding layer, as shown in Figure 5.2 (b). A separate 20nm-thick, Si-doped, ($[\text{Si}] \sim 5 \times 10^{18} \text{ cm}^{-3}$) n-type $\text{Al}_{0.25}\text{Ga}_{0.75}\text{N}$ CBL (N-CBL) was subsequently inserted between the Si-doped $\text{Al}_{0.10}\text{Ga}_{0.90}\text{N}$ cladding layer and the QWs, as shown in Figure 5.2 (c). Finally, both n-type and p-type $\text{Al}_{0.10}\text{Ga}_{0.90}\text{N}$ CBLs (NP-CBLs) were inserted at the bottom and the top of the QWs, as shown in Figure 5.2 (d).

The initial step in the fabrication of the vertical structure LEDs consisted of the sequential deposition of a 30nm-thick Ni layer and a 100nm-thick Au layer on each SiC substrate. These metal layers were annealed at 800°C for 20 min under flowing nitrogen at atmospheric pressure to obtain a backside ohmic contact and to activate the Mg to achieve p-type character within the various layers. A 4nm-thick Ni layer and a 4nm-thick Au layer were subsequently deposited on the top p-type GaN layer and annealed at 500°C for 10min in air to form a semitransparent electrode. Thick electrodes consisting

of a 100nm-thick Ti layer covered by a 1000nm-thick Au layer were deposited. The area of the semitransparent electrode that emitted light was $10.5 \times 10^{-4} \text{ cm}^2$. All metal layers were deposited via electron beam evaporation. Patterns were formed using standard photolithography and lift-off processes.

The various LED material structures were diced into chips having the dimensions of 0.2 cm by 0.4 cm and mounted on copper headers. The electrical and optical characteristics were measured under direct current operation at room temperature using a bare-chip geometry, a USB2000 spectrometer (Ocean Optics, Inc) and an integrating sphere.

5.3 Results and Discussion

Figure 5.3 shows the current-voltage characteristics of the LED without a CBL. The devices turned on at 3.2V and they had a series resistance of 18.4Ω . The LEDs fabricated with N-CBL and/or P-CBL showed the same turn-on voltage and series resistance; thus, the effect of these additional layers on these electronic characteristics was negligible.

Figure 5.4 (a)-(d) shows the electroluminescence (EL) spectra of the LEDs without a CBL, and with a P-CBL, an N-CBL and an NP-CBL, respectively, as a function of injection current. A small peak at 353nm and a broad peak centered at $\sim 540\text{nm}$ were observed at an injection current of 20mA in the LED without a CBL, as shown in Fig. 5.4 (a). The intensity of the 353nm peak increased much faster with injection current than that observed for the peak centered at $\sim 540\text{nm}$. The width of the former peak also

increased markedly with injection current. These phenomena indicate that the band-edge emission from the MQWs becomes dominant at higher forward currents. Previous investigators have reported that either the intensity of the shorter wavelength peak is saturated or this peak shifts to a longer wavelength as a function of increasing injection current due to heating of the device.^{2, 12-14)} However, neither a saturation in the intensity nor a shift in the position of the 353nm peak was observed, even when the dc injection current was increased to 200mA ($\sim 200\text{A/cm}^2$), as shown in Fig. 5.5(a). These positive results are very likely due to the high thermal conductivity of the SiC substrates.

A peak at $\sim 370\text{nm}$ was also observed on the shoulder of the 353nm peak in the LEDs without a CBL (Fig. 5.4(a)) and with an N-CBL (Fig. 5.4(c)); this peak was not observed in LEDs with either a P-CBL (Fig. 5.4(b)) or an NP-CBL (Fig. 5.4(d)). The acceptor activation energy of the $\text{p-Al}_{0.10}\text{Ga}_{0.90}\text{N}$ cladding layer has been reported to be 0.3eV .^{15,16)} As such, the transition energy from the conduction band to the acceptor level in the $\text{p-Al}_{0.10}\text{Ga}_{0.90}\text{N}$ cladding layer has been calculated by the present authors to be about 3.35 eV (370nm). This is consistent with other report of electron-hole recombination in the p-AlGaN side of the junction through the acceptor levels.¹⁷⁾ Thus, in LEDs without a CBL and with an N-CBL there may be significant electron overflow into the $\text{p-Al}_{0.10}\text{Ga}_{0.90}\text{N}$ cladding layer that results in the formation of the peak at $\sim 370\text{nm}$ through electron-hole recombination in the acceptor levels in the $\text{p-Al}_{0.10}\text{Ga}_{0.90}\text{N}$ cladding layer. LEDs with either a P-CBL or the combination of an N- and a P-CBL, electron overflow into the $\text{p-Al}_{0.10}\text{Ga}_{0.90}\text{N}$ cladding layer will be blocked by the P-CBL, and the intensity of shoulder peak at around 370nm will be substantially reduced.

The EL intensities of the 353nm peak, acquired from the LED without a CBL and

from those with the different types and placements of the CBLs, increased linearly as a function of injection current, as shown in Fig. 5.5 (a). The highest and second highest sets of intensities of this peak were emitted by the LEDs containing the P-CBL and the NP-CBLs, respectively. All intensities of this peak emitted by the LED containing the N-CBL were lower than those acquired from the LED without a CBL. More quantitatively, the intensity of the 353nm peak emitted by the P-CBL LED using an injection current of 100mA was almost eight times higher than that emitted by the LED without a CBL and two times higher than emitted by the LED with the NP-CBLs. The intensities of the LED containing the P-CBL also increased more rapidly than those from all other LED assemblies. These results show that the P-CBL is the most effective blocking layer for confining electrons within the quantum wells grown in this research. In other research, Kim *et al.*,¹⁸⁾ reported that the use of an n-type AlGaIn electron blocking layer positioned below the quantum wells improved the output power of InGaIn/GaN-based LEDs by reducing the number of hot electrons overflowing from these wells to the p-side via low energy electron tunneling injection. By contrast, the use of an N-CBL in the present study had an adverse effect on the peak intensity and the output power of the associated LED relative to those of all other LEDs, including the ones without a CBL. Electron flow to the MQWs appeared to be impeded by the N-CBL, and offset the positive benefits of carrier confinement. The use of NP-CBLs in AlGaIn-based UV LEDs has been reported^{2, 7-9)} to improve their power output by effectively confining electrons to the quantum wells. However, our results show that a single P-CBL is better than an NP-CBL for confining carriers and for making LEDs with higher output power.

Figure 5.5 (b) shows the EL intensities of the broad peak centered at ~540nm and acquired from the LEDs with different CBLs as a function of injection current. The origin of this emission can be surmised from considerations of the results and discussion associated with emission from other GaN-based materials and from a comparison of the intensities of the peaks at 353nm and 540nm observed in the present research. This peak is similar in energy and width to the yellow luminescence peak in the photoluminescence at room temperature from GaN or AlGaN alloy thin films.¹⁹⁻²¹⁾ The origin of this yellow luminescence has been reported²²⁻²³⁾ to be transitions from shallow (or deep) donors to deep (or shallow) acceptors or their complexes. It has also been proposed²⁴⁻²⁵⁾ that structural defects such as Ga vacancies and dislocations play roles in the radiative recombination responsible for the yellow luminescence. The results presented in Fig. 5.5(b) also show that the intensities of the 540nm peaks decrease in the same order according to the presence (or absence) of the same CBLs as those of 353nm peaks. This indicates that the UV emission at 353nm from the MQWs is the optical pumping source for the excitation that results in the emission of the 540nm peaks. As such, the intensities of the latter peaks are a direct function of the intensities of the emission of the 353nm spectra that are, in turn, a direct function of the degree of electron confinement inside the MQWs. A likely source of the 540nm emission is the top p-GaN layer via the partial absorption of the 353nm emission and the re-emission of the much broader and longer wavelength luminescence. Moreover, the higher the intensity of the emission from the MWQs the higher the intensity would be the yellow luminescence from the top p-GaN layer, as observed in Fig 5.5 (b) and implied above. Band-edge emission from the p-GaN by the absorption of the MQW emission should be ~363nm;

however, it's not observable, as it is covered by the relatively broad emission within the range of 350nm - 400nm.

The yellow luminescence observed in this research may also have been emitted from the AlGaIn layers within the MQWs. An increase in the injection current will allow more electrons to be supplied within the MQWs, which will result in an increase in the band-edge emission at 353nm as well as an increase in the yellow luminescence from the AlGaIn in the MQWs. As electrons are more effectively confined to the MQWs by the P-CBL, relatively more electrons will be available from this structure to stimulate the yellow luminescence as well as the band-edge emission at 353nm. Finally, it is possible that both sources contribute to the 540nm emission.

Another interesting point to be noted is that the intensities of the 540nm emission are saturated beyond an injection current of 80mA in all four sets of LEDs, while the 353nm emissions are not saturated, but linearly increase with the injection current. It has been reported^{20, 26)} that band-edge luminescence from GaN has a linear dependence, while the yellow luminescence has a nonlinear dependence on the intensity of the excitation light. Moreover, the latter luminescence becomes saturated at high light intensity, since the defect concentration and lifetime are finite.^{20, 26)} However, the reason the levels of the saturated emission intensities at 540nm are different in the LEDs with different CBLs is not clear.

Fig. 5.5(c) shows the peak intensity ratio of the 353nm emission to the 540nm emission ($I(353\text{nm})/I(540\text{nm})$) of the LEDs with different CBLs as a function of injection current. The ratio linearly increases with injection current. The values of this ratio calculated for the P-CBL LED were the highest at all injection currents, indicating that

the UV emission is dominant over any secondary visible emission. At an injection current of 100mA, the $I(353\text{nm})/I(540\text{nm})$ of the P-CBL LED is ~ 100 ; this value is more than two times higher than those of the LEDs with an NP-CBL or without a CBL. It has been reported²⁷⁾ that 352nm AlGaIn-based UV LEDs with an NP-CBL showed a much higher intensity ratio of UV emission-to-visible emission than LEDs without a CBL. However, our results show that the presence of a P-CBL is more effective than an NP-CBL to obtain a higher peak intensity ratio of UV emission-to-visible emission, since a P-CBL more effectively confines electrons to the QWs

Fig. 5.6 shows the light output power of our LEDs with different CBLs as a function of injection current. The LED having only the P-CBL also exhibited the highest output power, and the values of this parameter increased faster as a direct function of the injection current than in the other LEDs. Using an injection current of 100mA caused, the generation of output power was more than two times higher than that generated in the LED without a CBL. Again, this may be attributed to the most effective electron confinement within the MQWs.

5.4 Summary

The optical characteristics of AlGaIn based UV LEDs with and without p-type and n-type AlGaIn carrier blocking layers at the top and the bottom of the quantum wells, respectively, were investigated. The emission from the LED with a p-type carrier blocking layer at the top of the quantum wells exhibited the highest peak intensity at 353nm and the greatest light output power as a function of injection current. The

presence of an n-type carrier blocking layer at the bottom of the quantum wells had an adverse effect on the LED characteristics, and its effect on carrier confinement was negligible. The intensity of a broad peak centered at ~540nm and emitted by all the devices increased with the same order of the UV emissions at 353nm. The origin of the former emission is believed to be caused by yellow luminescence from the p-GaN excited by the UV emission and/or from the AlGaN layers within the quantum wells by current injection.

Acknowledgements

This research was supported by the Office of Naval Research under contract N00014-03-1-0790, Mihal Gross, monitor. The SiC substrates were provided by Cree, Inc. J.-S Park wishes to thank Joe Matthew for his help in sample preparation and wire bonding, and R.F. Davis was partially supported by Kobe Steel Ltd. University Professorship.

5.5 References

- 1) K. Domen, R. Soejima, A. Juramata, T. Tanahashi: MRS Internet J. Nitride Semicond. Res. **3** (1998) 2.
- 2) T. Nishida, H. Saito, and N. Kobayashi: App. Phys. Lett. **78** (2001) 3927.
- 3) J. Zhang, W. Shuai, S. Rai, V. Mandaville, V. Adivarahan, A. Chitnis, M. Shatalov, and M.A. Khan: Appl. Phys. Lett. **83** (2003) 3456.
- 4) W.H. Sun, J.P. Zhang, V. Adivarahan, M. Shatalov, S. Wu, V. Mandavilli, J.W. Yang,

- and M.A. Khan: Appl. Phys. Lett. **85** (2004) 531.
- 5) K. Akita, T. Nakamura, and H. Hirayama: Phys. Status Solidi (a) **201** (2004) 2624.
 - 6) A. Chitnis, J.P. Zhang, V. Adivarahan, M. Shtalov, S. Wu, R. Pachipusulu, V. Mandavilli, and M.A. Khan: Appl. Phys. Lett. **82** (2003) 2565.
 - 7) T. Nishida, T. Makimoto, H. Saito, and N. Kobayashi: App. Phys. Lett. **84** (2004) 1002.
 - 8) C. Chen, V. Adivarahan, J. Yang, M. Shatalov, E. Kuostis, and M. A. Khan: Jpn. J. Appl. Phys. **42** (2003) L1039.
 - 9) T. Nishida, T. Ban, and N. Kobayashi: Jpn. J. Appl. Phys. **42** (2003) 2273.
 - 10) T. Nishida, N. Kobayashi, and T. Ban: Appl. Phys. Lett. **82** (2003) 1.
 - 11) S. Einfeldt, Z.J. Reitmeier, and R.F. Davis: J. Cryst. Growth **253** (2003) 129.
 - 12) V. Adivarahan, A. Chitnis, J.P. Jhang, L.W. Yang, G. Simin, A.A. Khan, R. Gaska, and M.S. Shur: Appl. Phys. Lett. **79** (2001) 4240.
 - 13) A. Kinoshita, H. Hirayama, M. Ainoya, Y. Aoyagi, and A. Hirata: Appl. Phys. Lett. **77** (2000) 175.
 - 14) M.A Sanchez-Garcia, F.B. Naranjo, J.L. Pau, A. Jimenez, E. Calleja and E. Munoz, J. Appl. Phys. **87** (2000) 1569.
 - 15) M. Katsuragawa, S. Sota, M. Komiro, C. Anbe, T. Takeuchi, H. Sakai, H. Amano, and I. Akasaki: J. Cryst. Growth **189/190** (1998) 528.
 - 16) M. Suzuki, J. Nishio, M. Onomura, and C. Hongo: J. Cryst. Growth **189/190** (1998) 511.
 - 17) T.M. Katona, M.D. Craven, J.S. Speck, and S.P. DenBaars: Appl. Phys. Lett. **85**

(2004) 1350.

18) K.C. Kim, Y.C. Choi, D.H. Kim, T.G. Kim, S.H. Yoon, C.S. Sone, and Y.J. Park: Phys. Status Solidi (a) **201** (2004) 2663.

19) S. Nakamura and T. Mukai: Jpn. J. Appl. Phys. **31** (1992) L1457.

20) R. Singh, R.J. Molnar, M.S. Unlu, and T.D. Moustakas: Appl. Phys. Lett. **64** (1994) 336.

21) W. Grieshaber, E.F. Shubert, I.D. Goepfert, R.F. Karlicek, Jr., M.J. Schurman, and C. Tran: J. Appl. Phys. **80** (1996) 4615.

22) S.O. Kucheyev, M. Toth, M.R. Phillips, J.S. Williams, C. Jagadish, and G. Li: J. Appl. Phys. **91** (2002) 5867.

23) J.S. Colton, P.Y. Yu, L. Teo, E.R. Weber, P. Perlin, I. Grzegory, and K. Uchida: Appl. Phys. Lett. **75** (1999) 3273.

24) J. Neugebauer and C. Van de Walle: Appl. Phys. Lett. **69** (1995) 503.

25) G. Li, S.J. Chua, S.J. Xu, W. Wang, P. Li, B. Beaumont, and P. Gibart: Appl. Phys. Lett. **74** (1999) 2821.

26) M.A. Reshchikov, and R.Y. Korotkov: Phys. Rev. B **64** (2001) 115205.

27) T. Nishida and N. Kobayashi: Proceedings of SPIE **4641** (2002) 68.

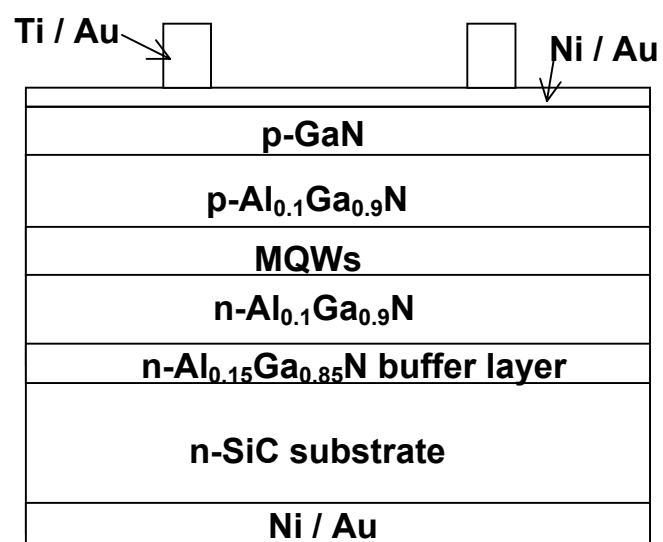


Figure 5.1 Cross-sectional schematic of the LED structure without CBL.

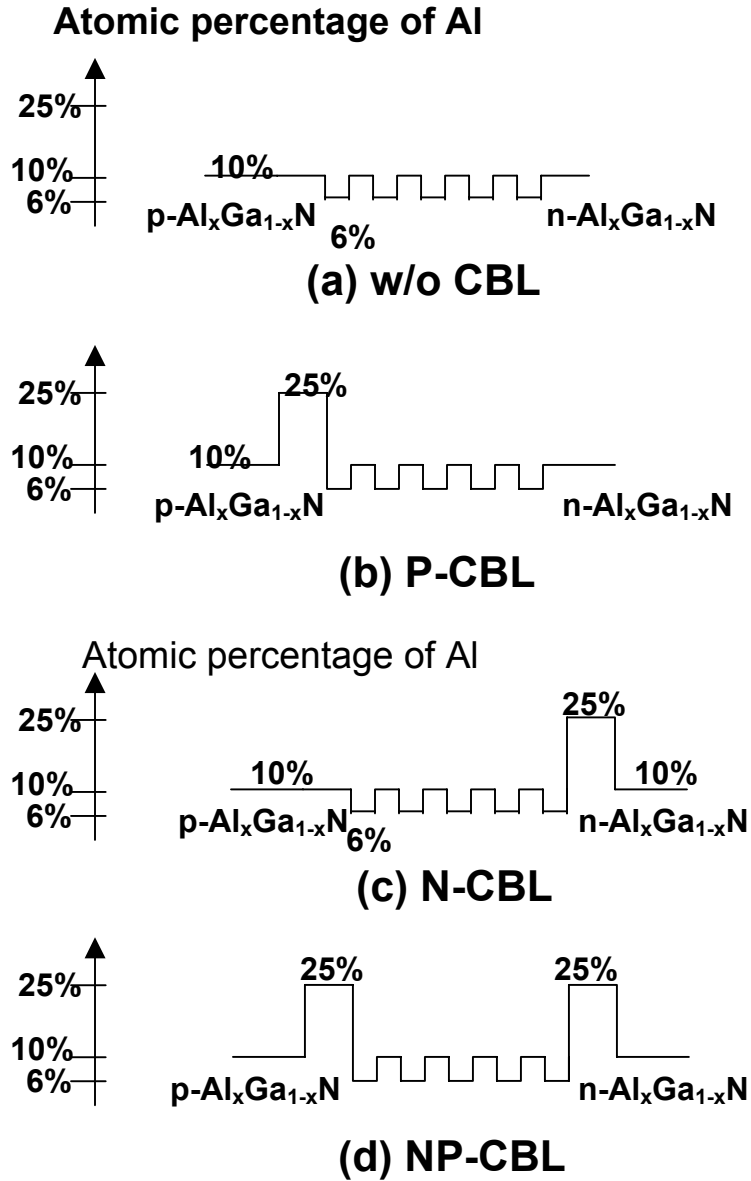


Fig. 5.2 Schematic diagrams showing the positions of the MQWs in the LEDs (a) without a CBL, (b) with a P-CBL, (c) with an N-CBL, and (d) with N- and P-CBLs and the percentages of Al in each layer.

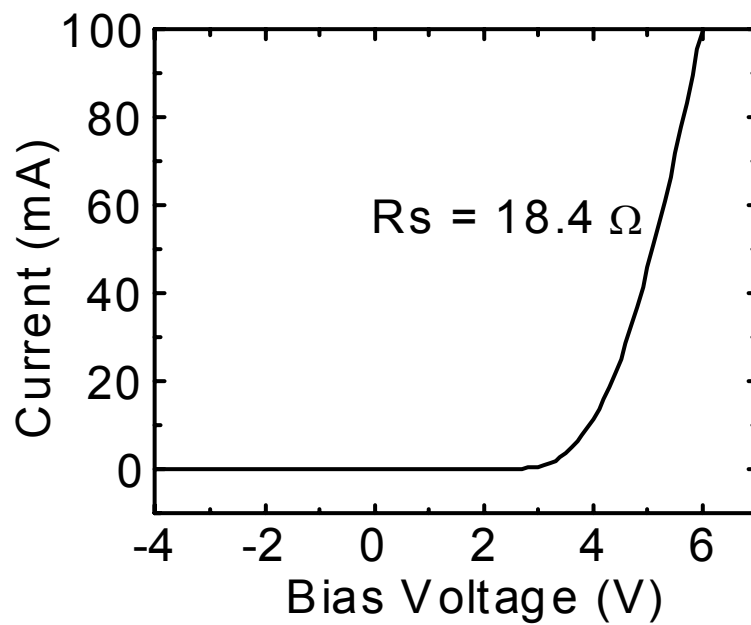


Fig. 5.3 Current-voltage characteristic of LEDs without a CBL.

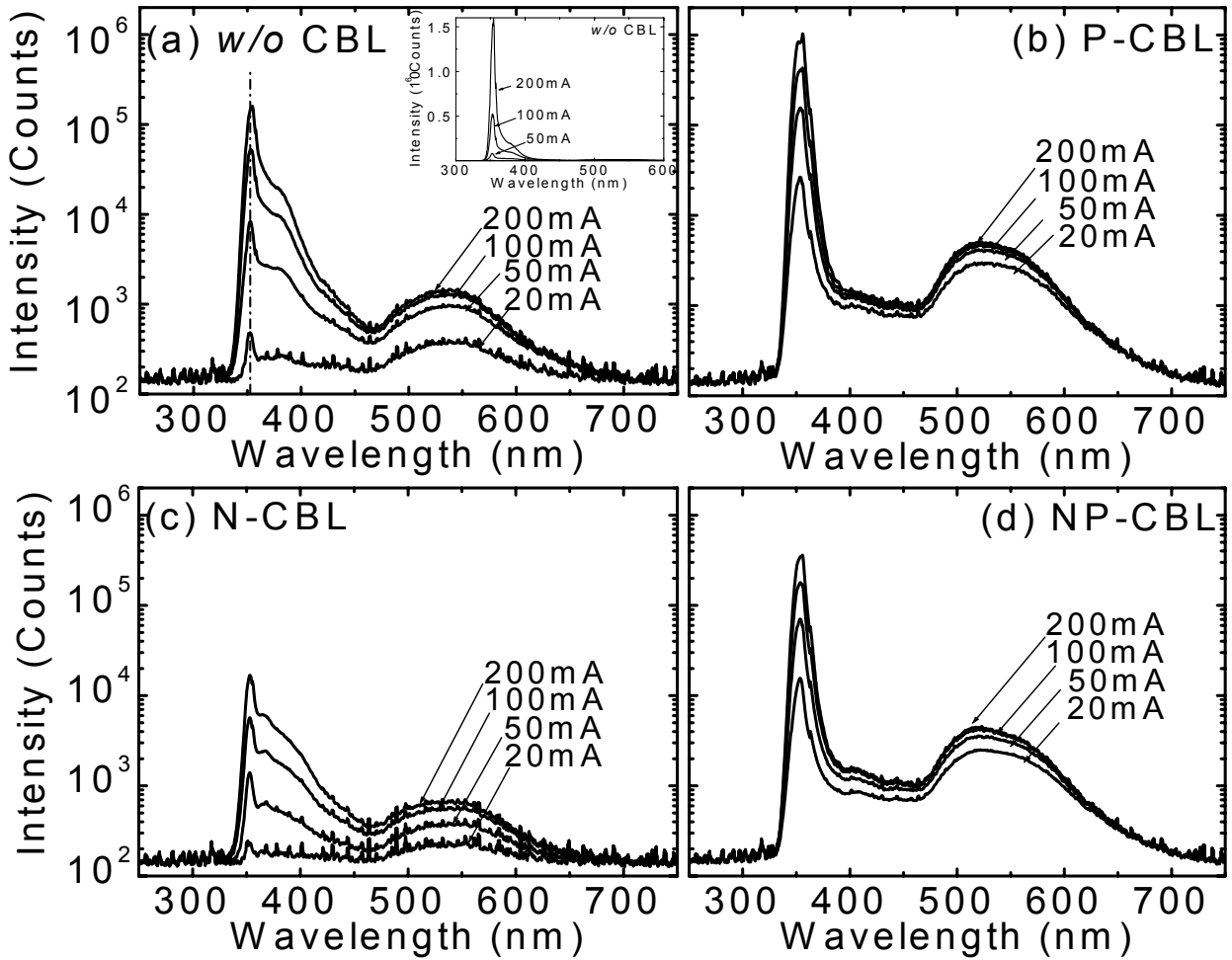


Fig. 5.4 Semilogarithmic plots of EL spectra acquired from LEDs (a) without a CBL, (b) with a P-CBL, (c) with an N-CBL, and (d) with NP-CBLs as a function of injection current. The inset in (a) shows linear plots of the EL spectra of an LED without a CBL.

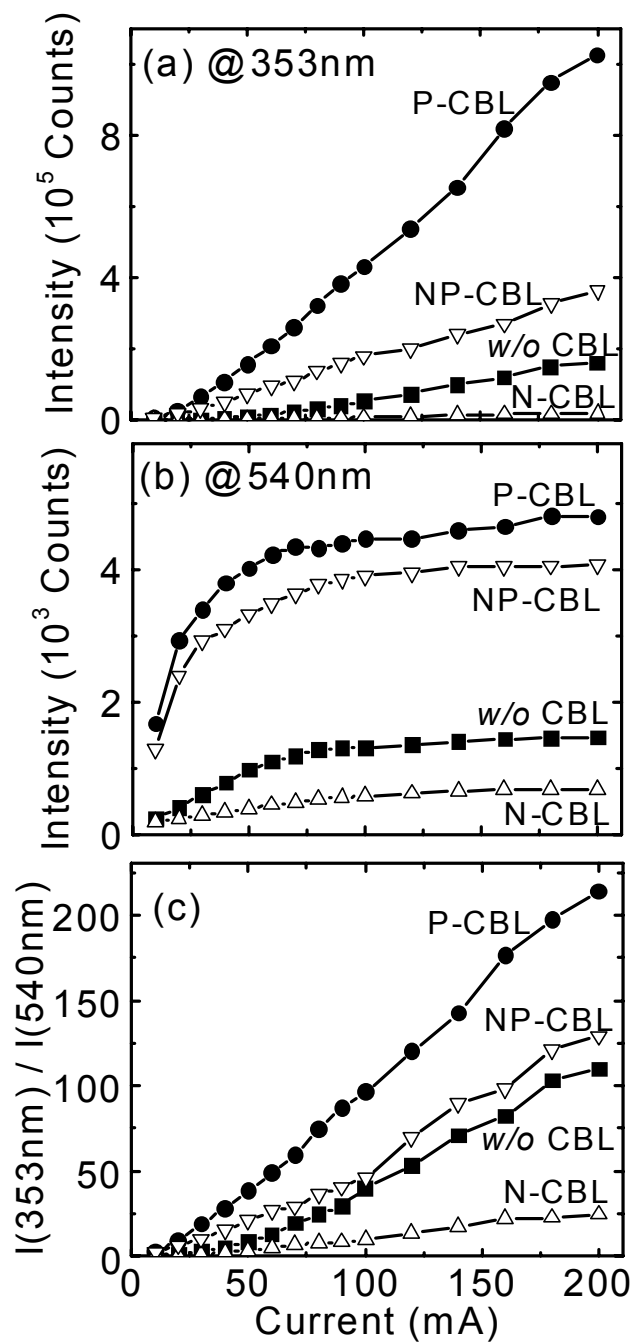


Fig. 5.5 EL intensities as a function of injection current of (a) the 353nm peaks and (b) the 540nm peaks and (c) the intensity ratios of the 353nm peaks to 540nm peaks of LEDs with different CBLs.

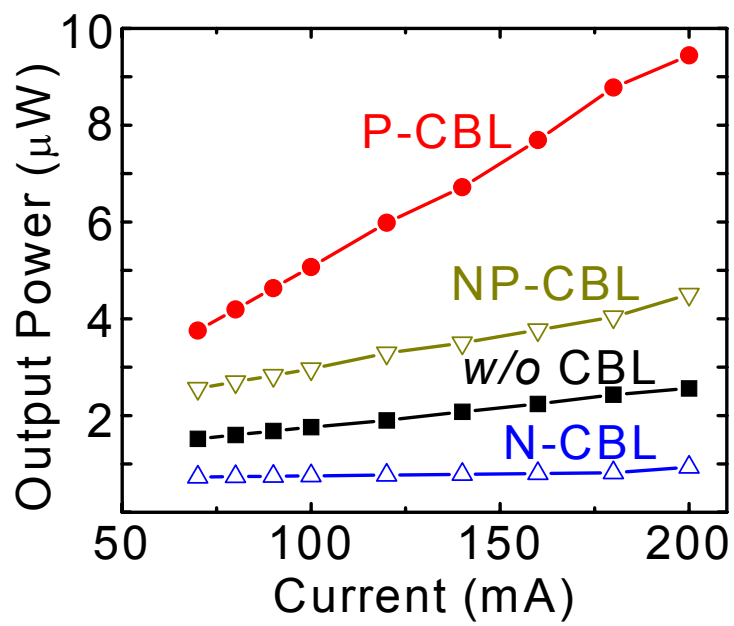


Fig. 5.6 Light output power of the LEDs with different CBLs as a function of injection current.

6. Recommendations for Future Research

$\text{Al}_x\text{Ga}_{1-x}\text{N}$ films ($x < 0 \leq 1$) have been grown on Si- and C-terminated 6H-SiC{0001} substrates and characterized for electron emission applications, as described in Chapter 3. Using the SiH_4 flow rate, which yields a Si concentration of $\sim 1 \times 10^{19} \text{ cm}^{-3}$ in GaN, the upper limit of the mole fraction of Al wherein a value of $N_D - N_A$ could be measured ~ 0.61 . It has been suggested by other investigators that the decrease in the values of $N_D - N_A$ is due to (1) the decrease in the energy of the Si donor state (the value of energy at the top of the valence band is taken to be zero) as a function of the increase in the band gap with an increase in the Al concentration^{1,2} and possibly to (2) auto-compensation by Si,² and/or acceptor impurities.³⁻⁵ As such, it is important to determine if one of more acceptor impurities are present in the Si-doped AlGaN films and, if so, also determine if the concentration of any of these p-type dopants increases with an increase in the concentration of either the Al or the Si. If it is determined that the values of the $N_D - N_A$ decrease primarily because the energy of the Si donor state decreases with an increase in the Al concentration, it is recommended that other donor dopants such as Ge be investigated. Germanium is an interesting choice because (1) the covalent radii of this element and Ga are 0.122 and 0.126, respectively, and (2) the covalent radii of Si and Al are 0.111 and 0.118, respectively. Thus, Ge and Si are somewhat more likely to substitute on the Ga and Al sites, respectively. Moreover, the Ge-N bond strength is very weak (a germanium nitride may not even exist); by contrast the Si-N bond strength is very strong. As such, Si in substitutional sites in AlGaN alloys may have a strong tendency to phase separate into clusters of a Si-rich nitride or nucleate precipitates of a

Si_xN_y phase, especially at higher concentrations; whereas Ge may not possess either tendency. As such, research should be conducted to determine if the donor energy level produced by the addition of Ge to AlGa_xN solid solutions also decreases as a direct function of the increase in the Al concentration.

It may also be possible to increase in the upper limit of the Al mole fraction wherein n-type doping is achieved by increasing either the Si or the Ge concentration above $1 \times 10^{19} \text{ cm}^{-3}$ such that a donor band is formed, the top of which spreads toward the bottom of the conduction band, i.e., the highest energy states in the band are close to the conduction band minimum. As such, the donor states that can be ionized are positioned higher in energy than the states in the single energy level in the $\text{Al}_x\text{Ga}_{1-x}\text{N}$ solid solutions having Si or Ge concentrations $< 1 \times 10^{19} \text{ cm}^{-3}$. However, it is important to remember that a thermodynamic competition always exists between the formation and/or the spread of an energy band and the formation of either phase separated clusters or classically nucleated or spinodally formed second phases that effectively reduce the concentration of the dopant species in the host semiconductor and thereby establish both the upper limit of the equilibrium solubility range of the dopant and the maximum value of the Al concentration wherein a value of $N_D - N_A$ can be measured.

N-polar AlN films exhibited a lower work function at surface than that of Al-polar films; thus, the surface work function of undoped and donor doped N-polar $\text{Al}_x\text{Ga}_{1-x}\text{N}$ films should be evaluated and compared with that of Al(Ga)-terminated films.

Ionicity in wurtzite and other non-cubic crystal structures creates internal dipoles that produce positive and negative surface charges on the crystallographic planes that are orthogonal to the orientation of the dipoles. These surface charges, in turn, produce

internal spontaneous polarization parallel to the orientation of the dipoles. The magnitude of the spontaneous polarization in AlGa_xN solid solutions increases with an increase in the Al concentration. The growth of AlGa_xN/GaN heterostructures results in a substantial change in polarization that is positive across the interface from Ga-polar GaN to N-polar AlGa_xN. This ΔP produces substantial downward band bending and therefore change in the Fermi level (the electronic chemical potential) in the GaN very near the interface which causes the diffusion of a very large concentration of electrons from the bulk of the GaN into this near surface region that, in turn, results in a marked increase in the sheet charge density and the creation of a two-dimensional electron gas. This phenomenon is effectively polarization-induced donor doping of the GaN. If the AlGa_xN film is grown sufficiently thin, it may allow the tunneling of the electrons from the two-dimensional electron gas into vacuum and thus the continued emission of a very large flux of electrons from the AlGa_xN surface under the influence of an applied field. In this regard, the degree of ionicity in ZnO and MgZnO are markedly greater than in GaN and AlGa_xN. As such, the value of ΔP across the interface and the associated sheet charge density and the concentration of electrons in the two-dimensional gas may be significantly greater than in the GaN/AlGa_xN heterostructures.

Growth of donor doped III-nitride hexagonal pyramid structures may also enhance the electron emission from these materials. For example, if Al_xGa_{1-x}N films are grown on GaN hexagonal pyramids, electron emission may be more improved, since the electron affinity of Al_xGa_{1-x}N solutions is lower than that of GaN. In addition, it is proposed that since N-terminated films have a lower work function at the surface, the growth of similarly terminated GaN hexagonal pyramids on C-terminated SiC substrates,

followed immediately by the growth of $\text{Al}_x\text{Ga}_{1-x}\text{N}$ films may show enhanced electron emission characteristics.

Chapter 4 details the growth of AlGa N films, quantum wells, and p-GaN and n-SiC contacts for the fabrication of ultraviolet light emitting diodes (UV LEDs). As noted in Chapter 1, the high density of dislocations in all heteroepitaxially grown III-nitride films is the most critical problem that must be solved for the realization of high-power UV LEDs. In other words, the output power of all UV LEDs would be improved if they were fabricated in material structures that were grown on free-standing GaN or AlGa N substrates that also possessed a low density of dislocations. In this regard, the In-segregation effect reported by Hirayama *et al.*⁶ should be further investigated and applied to increase the output power of UV LEDs. For this, growth and optical characterization of AlInGa N quaternary films will be necessary. Finally, acceptor-type doping in these LED structures may also be improved with the use of a Mg-doped AlGa N /GaN superlattice structure.

In Chapter 5, the results of my investigations of the effect of various n- and p-doped carrier blocking layers on the emission characteristics of AlGa N -based UV LEDs were reported. The emission of both strong UV and moderate visible (yellow) radiation was observed. For the application of long life-time UV LEDs for the excitation of selected phosphors in white lighting or color displays, the visible emission must be suppressed. The possible origins of the visible emission, namely, the excitation of the p-type capping layer from light emitted by the quantum wells and/or excitation within the quantum wells, were also considered in Chapter 5. If the former is the source of the visible emission the growth of different thicknesses of the p-GaN capping layer should

result in an increase in the intensity of this longer wavelength radiation. Conversely, the growth of a very thin semi-transparent metal electrode on the p-AlGa_{0.1}N cladding layer without a p-GaN capping layer would also be a possible solution to reduce the visible emission. As such, the growth and doping of the p-Al_{0.1}Ga_{0.9}N ohmic contact must be investigated.

References

1. A.Y. Polyakov, N.B. Smirnov, A.V. Govorkov, M.G. Milividski, J.M. Redwing, M. Shin, M. Skowronski, D.W. Greve, and R.G. Wilson, *Solid State Electron.* **42**, 627 (1998).
2. Y. Taniyasu, M. Kasu, and N. Kobayashi, *Appl. Phys. Lett.* **81**, 1255 (2002).
3. M.D. McCluskey, N.M. Johnson, C.G. Van de Walle, D.P. Bour, M. Kneissl, and W. Walukiewicz, *Phys. Rev. Lett.* **80**, 4008 (1998).
4. S. Fischer, C. Wetzel, E.E. Haller, and B.K. Meyer, *Appl. Phys. Lett.* **67**, 1298 (1995).
5. C.G. Van de Walle, C. Stampfl, J. Neugebauer, M.D. McCluskey, and N.M. Johnson, *MRS Internet. J. Nitride Semidcond. Res.* **4S1**, G10.4 (1999).
6. H. Hirayama, A. Kinoshita, T. Yamabi, Y. Enomoto, A. Hirata, T. Araki, Y. Nanishi, and Y. Aoyagi, *Appl. Phys. Lett.* **80**, 207 (2002).

7. Appendices

7.1 Detailed Process Sequences and Conditions for the Fabrication of Ultraviolet Light Emitting Diodes on 6H-SiC(0001) Substrates.

1. Growth of LED structures

- (1) Clean SiC wafer (resistivity $\leq 0.05 \Omega \cdot \text{cm}$) in 10% HF for 10 min
- (2) Grow LED structures including n-AlGaIn buffer layer, AlGaIn cladding layer, quantum wells, p-AlGaIn and GaN capping layers.
- (3) After growth, the chamber should be baked for 30min at 1100°C and then platter and alumina tube should be cleaned in warm NaOH and RT 50% HCl, respectively, followed by rinsing in DI water and N₂ blowing for dry to grow another sample without memory effect of Mg. Inner quartz wall needs to be wiped out using methanol without taking apart the system.

2. N-SiC backside contact process

- (1) Clean the LED samples in TCE, Acetone and Methanol for 5min each using ultrasonic
- (2) PR (Shipley 1813) coating on the front side of the sample to protect against HF cleaning of the backside of the sample
- (3) Hard bake at 115°C for 5min
- (4) Clean backside of the sample in 10% HF for 10min

- (5) Load the sample in the e-beam evaporator without delay and pump down to 5×10^{-6} Torr.
- (6) Deposit 30nm-thick Ni and 100 nm-thick Au on the backside of the sample
- (7) Remove PR using Shipley 1165 remover
- (8) Anneal at 800 °C for 20 min in flowing N₂ using furnace for Mg activation and for n-SiC contact
- (9) Slice wafer into 4 pieces of a quarter of 2 inch wafer by hand using diamond scratch. Dicing machine can hurt samples or backside metal if there is metal on the sample backside.

3. Transparent metal electrode process (p-GaN contact)

- (1) Clean the samples in TCE, Acetone and Methanol for 5min each using ultrasonic
- (2) Hard bake at 115C for 5min
- (3) PR coating (Shipley 1813 + imidizol) at 3500 rpm for 40 sec
- (4) Soft bake at 115°C for 1min
- (5) Exposure (aligner: MBJ3) for 1.75min using transparent metal electrode mask
- (6) Reversal bake at 115°C for 2min
- (7) Develop for about 1min
- (8) Clean p-GaN surface in HCl:DI (1:1) solution at 85°C for 10min.
- (9) Load the sample in the e-beam evaporator with out delay and pump down to 5×10^{-6} Torr.
- (10) Deposit 4nm-thick Ni and 4nm-thick Au consequentially at growth rate of 0.1 or 0.2 nm/sec after 10nm dummy deposition.

(11) Metal lift-off in 1165 remover

(12) Anneal the sample at 500°C for 10 min in air for p-GaN contact

4. Thick metal electrode process

(1) Clean the samples in TCE, Acetone and Methanol for 5min each. Do not use ultrasonic to protect semi-transparent p-GaN contact.

(2) Hard bake at 115°C for 5min

(3) PR coating (Shipley 1813 + imidizol) at 3500 rpm for 40 sec

(4) Soft bake at 115°C for 1min

(5) Exposure (aligner: MBJ3) for 1.75min using thick metal electrode mask. Thick metal electrode should be aligned into semi-transparent metal electrode.

(6) Reversal bake at 115°C for 2min

(7) Develop for about 1min.

(8) Deposit 10nm-thick Ti and 100nm-thick Au using e-beam evaporator.

(9) Metal lift-off in 1165 remover.

7.2 Calibration Procedures for Light Output Power Measurements of Ultraviolet Light Emitting Diodes Fabricated in This Program.

1. Using the tungsten lamp LS-1-CAL (Ocean Optics Inc.) to calibration the spectral response of the system above 400 nm (visible range). The procedure is listed in the OOIIRAD manual, page 14, from step 14 to step 18.
2. Refer to *The Book of Photon Tools* (Oriel Instruments), page 1-46, Fig. 1, reproduce the data of “irradiance vs. wavelength” curve of D₂ Lamp. Please note that the absolute value of irradiance at each wavelength ($\mu\text{W}/\text{m}^2/\text{nm}$ at 0.5 m) is not calibrated. The only useful information that these data give us is the relationship between the irradiance at visible range and that at UV range. That is to say, if we know the LED’s irradiance over visible range (>400nm), we ought to be able to find out its irradiance over the UV range using these data.
3. Measure the spectrum data (scope) of the D₂ Lamp using USB2000 spectrometer. Divide the irradiance taken in step 2 by this scope data, and the results is the calibration factors acquired from D₂ Lamp. Unlike the tungsten lamp calibration, this calibration has taken the spectral response of the system over the UV and blue/green range into consideration (250 nm - 500 nm). However, we still only know the relative irradiance over this wavelength range.
4. Take both the spectrum and irradiance of the LED using USB2000 and OOIIRAD software. Please note here the irradiance is calculated from the spectrum and the tungsten calibration data. Therefore, it is believable above 400 nm but not in the UV range.
5. Multiply the spectrum of the LED and the D₂ Lamp calibration factors computed in step 3. The irradiance acquired this way is believable from 250 nm to 500 nm, except its absolute value. We know the absolute irradiance at 500 nm from step 4, and therefore only need to shift this relative irradiance curve to match that value.
6. Verification: From 4 and 5, we know the two irradiance curves after the tungsten and the D₂ Lamp calibrations are believable from 400 nm to 500 nm. Therefore, these two curves should be the same.